学位論文

Hydrodynamic response to jet propagation in quark-gluon plasma

(ジェットに対するクォーク・グルーオン・プラズマの流体力学的応答)

平成２６年１２月博士（理学）申請

東京大学大学院理学系研究科

物理学専攻

橘　保貴

Hydrodynamic response to jet propagation in quark-gluon plasma

Yasuki Tachibana

Department of Physics, The University of Tokyo

December 2014

PhD Thesis

Abstract

In this thesis, we study the hydrodynamic response to jet propagation in the quark-gluon plasma (QGP). The QGP, the deconfined state of quarks and gluons, is realized under extreme conditions such as the heavy ion collisions (HIC) where extremely high-temperature is achieved by a head-on collision of two heavy nuclei accelerated at nearly the speed of light. The QGP created in the HIC behaves as an almost-perfect fluid and expands with relativistic velocity. The space-time evolution of the QGP is known to be well described by the relativistic hydrodynamics. In the HIC, high-energy quarks and gluons, so-called jets, are produced by hard processes. They do not participate in the hydrodynamical evolution of the QGP fluid, but traverse the QGP while losing their energies and momenta due to strong interactions. The QGP medium are excited by the incoming energy and momentum from jets and Mach cones emerge as the hydrodynamic response. Such a hydrodynamic response carries the information of various properties of QGP. In Pb-Pb collisions at LHC, low momentum particles at large angles from the jets are enhanced in dijet asymmetric events. Since these low momentum particles are considered as constituents of the hydrodynamic fluid, their enhancement at large angles can be interpreted as the hydrodynamic response to the jets.

Motivated by the experimental data in the HIC, we study the space-time evolution of the QGP in dijet asymmetric events to make a theoretical connection between the medium response to the jet propagation and the enhancement of the low-momentum particles in the HIC. We formulate a hydrodynamic model with source terms to describe the space-time evolution of the QGP fluid with jet propagations. Then, we perform simulations in the case of the dijet traversing the center of the expanding medium. We find the Mach cones which are distorted strongly by the radial expansion of the medium. We show the enhancement of low momentum particles at large angles in dijet asymmetric events take place as a result of the distorted Mach cone. Furthermore, we perform simulations by changing both the jet production points and the initial energies of dijet. We evaluate the effect of the number of dijet events and carry out the event averaged calculations. As a result, we show that the enhancement of low momentum particles at large angles is the universal phenomenon originating from the hydrodynamic response to the jet propagation.

Table of Contents

List of Abbreviations

QCD	: Quantum Chromodynamics
QGP	: Quark-gluon Plasma
HIC	: Heavy Ion Collisions
RHIC	: Relativistic Heavy Ion Collider
LHC	: Large Hadron Collider
JAM	: Jet AA Microscopic transport model
UrQMD	: Ultra-relativistic Quantum Molecular Dynamics model
EoS	: Equation of State
PDF	: Parton Distribution Function
FF	: Fragmentation Function
BDMPS-Z formalism	: Baier-Dokshitzer-Mueller-Peigne-Schiff and Zakharov formalism
ASW formalism	: Amesto-Salgado-Wiedemann formalism
AMY formalism	: Arnold-Moore-Yaffe formalism
GLV formalism	: Gyulassy-Levai-Vitev formalism
HT equation	: Higer Twist formalism
AdS/CFT correspondence	: Anti-de Sitter/Conformal Field Theory correspondence

τ	: Proper time
η_{s}	: Space-time rapidity
ϕ	: Azimuthal angle
p_T	: Transverse momentum
m_T	: Transverse mass
η_p	: Pseudorapidity
y	: Rapidity
ϕ_p	: Azimuthal angle in momentum space
$g_{\mu\nu}$	: Metric
$\eta_{\mu\nu} = \mathrm{diag}(1,\ -1,\ -1,\ -1)$	: Minkowski metric

$\sqrt{s_{NN}}$:Center of mass energy per nucleon-nucleon collision
Y_{beam} : Beam rapidity of incoming nucleus
N_{ch} : Number of charged particles
N_{coll} : Number of collisions
N_{part} : Number of participants
n_{coll} : Number density of collisions in transverse plane
n_{part} : Number density of participants in transverse plane
b : Impact parameter
A_J : Asymmetry ratio of dijet
$\not{p}_T^{||}$: Missing transverse momentum
$\Delta R = \sqrt{\Delta\phi^2 + \Delta\eta^2}$: Size of jetcone

p : Proton
Pb : Lead
Au : Gold

α_s : Strong coupling constant
N_f : Number of flavors
C_R : Casimir operator
m_D : Debye mass

θ_M : Mach angle

$T^{\mu\nu}$: Energy momentum tensor
N_i : Conserved charge current
u^μ : Flow
v : Flow velocity
$\Delta^{\mu\nu}$: Projection operator
e : Energy density
P : Pressure
c_s : Sound velocity
n_i : Conserved charge density
T : Temperature
T_f : Freezeout temperature
T_c : Crossover temperature
τ_0 : Initial proper time
s : Entropy density
μ_i : Chemical potential
J^ν : Source term
Σ : Freezeout hypersurface
$d\sigma$: Hypersurface element

Chapter 1

Introduction

Quarks and gluons are the elementary particles with color charges: Their interactions are described by quantum chromodynamics (QCD), which is one of the four fundamental forces in nature. According to QCD, quarks and gluons are confined in hadrons and cannot be observed as isolated particles in ordinary conditions (color confinement). However, QCD also predicts the existence of the quark-gluon plasma (QGP), the deconfined state of quarks and gluons, under extremely high temperature and density [1]. QGP is the primordial form of the matter which filled the universe a few microseconds after the Big Bang. Investigation of the properties of QGP provides not only insight into the underlying QCD theory in various physical phenomena, but also understanding of the dynamics of the universe just after the Big Bang. The experimental explorations in the research of QGP are carried out in the heavy-ion collisions (HIC) at Relativistic Heavy Ion Collider (RHIC) in Brookhaven National Laboratory (BNL) and Large Hadron Collider (LHC) in CERN. In the HIC, extremely high-temperature is achieved by a head-on collision of two heavy nuclei accelerated at nearly the speed of light.

The QGP created in the HIC is not static, so that its bulk properties are encoded in spectra of low transverse momentum hadrons detected in the final state. The blue-shifted thermal equilibrium spectra of the transverse momentum and the anisotropic azimuthal distribution of particle emission are the consequences of the radial expansion of the hot matter with relativistic velocity: The QGP keeps *local* thermal equilibrium and collective flow in response to the anisotropic pressure gradient structure associated with the initial geometry. Such clues support that the QGP behaves as a relativistic fluid whose space-time evolution is described by the relativistic hydrodynamic equations [2, 3, 4, 5, 6]. Hydrodynamic modeling of HIC provides a unique phenomenological approach to extract the properties of the QGP from the space-time evolution of non-static and strongly coupled matter.

The high transverse momentum region of hadron spectra in HIC is dominated by collimated clusters of particles, so-called jets, originating from hard scatterings between the partons of the two colliding nuclei in the initial stage. They do not take part in the hydrodynamical expansion because of their large transverse momenta. They are subject to traverse the QGP fluid and lose their energy through the strong interaction with the QGP medium [7, 8, 9, 10, 11, 12, 13]. As

a consequence of this jet quenching phenomenon, yields of high-transverse momentum hadrons in HIC are suppressed relative to in proton-proton collisions where the QGP medium is not formed. Recent dijet event measurement at LHC provides more detail information about the jet quenching. At the leading order, jets are created as a back-to-back pair with equal transverse momenta. However observed dijets in HIC are highly imbalanced relative to the those in hadron-hadron collisions [14]. This can be interpreted as a consequence of jet quenching and path length difference of the dijet. The QGP created in HIC has finite size with a temperature profile. One of the dijet going toward the inside high-temperature region of the QGP is more quenched than the other one going the outside of the medium.

Jets in HIC lose their energy and momentum, so the lost energy and momentum must be transfered somewhere due to the conservation law. In Pb-Pb collision at LHC, enhancement of low transverse momentum particles at large angles from an axes of jets is observed in asymmetric dijet events by CMS Collaboration [15, 16] [Fig.1.1]. These low transverse momentum particles compensate the imbalance between the dijet and their transverse momenta are sufficiently low so that one can consider them as constituents of hydrodynamical evolution. Therefore, it is natural to consider that the energy-momentum deposition of jets wakes collective flow inducing low momentum particles emitted at large angles from the jet axis.

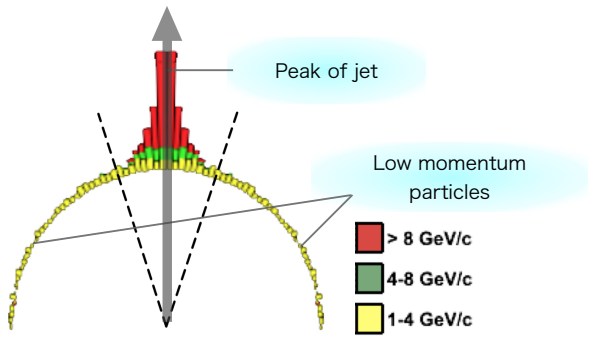

Figure 1.1: Azimuthal angle distribution of transverse momentum in dijet event observed by CMS at LHC. Each color in histgrams represents the contribution in a transverse-momentum ranges: 1-4 GeV/c (yellow), 4-8 GeV/c (green) and $p_T > 8$ GeV/c (red). (Figure adapted from the slides of Ref. [17].)

From the point of view of hydrodynamics, jets can be considered as supersonic moving sources of energy and momentum. Such supersonic moving source in a fluid induces a conical shock front, so-called the Mach cone, as interference of sound waves. The conical shock front propagates toward a specific angle from the direction of the supersonic moving source. The specific angle is determined by the sound velocity of the fluid [18]. If Mach cones are induced by

jets in QGP fluid, constituent particles of hydrodynamical evolution are preferentially emitted at large angles from the jet axis [19, 20]. The Mach cone in QGP fluid has been studied by models of hydrodynamic calculations with [20, 21, 22, 23, 24, 25] and without [26, 27, 28, 29, 30, 31, 32] linearlization, models of AdS/CFT correspondence [33, 34, 35], and a parton-transport model [36, 37]. It should be emphasized that the background QGP fluid in HIC expands with relativistic flow velocity and the Mach cone propagates with 3-dimensional structure. The expansion of the QGP distorts the Mach cone, so that the Mach cone breaks the boost invariance which the QGP profile is supposed to have as an approximate symmetry.

In this thesis, hydrodynamic response to the jet propagation in the expanding QGP fluid is studied. We formulate a hydrodynamical model to describe the space-time evolution of the QGP with the energy-momentum deposition from the jet. Assuming that the deposited energy and momentum are thermalized locally in the fluid, the source terms representing the incoming energy and momentum are introduced to the hydrodynamic equations. We perform the simulations of dijet events in HIC to see its space-time evolution as well as the resultant spectra from the QGP medium modified by the jet propagation. We solve the relativistic hydrodynamic equations with source terms numerically in the $(3+1)$-dimensional Milne coordinate. In the simulations, Mach cones induced via the source term carry the deposited energy and momentum away from the jet. In the expanding QGP, the structures of Mach cones are largely distorted by the radial flow. The spectra from the QGP medium is modified by the flow structure at the freezeout. As a result of the flows on the Mach cones spread away from the jets, the low-p_T particles are enhanced at large angeles from the jets as seen in the data by the CMS collaborations [15]. We first perform the simulations of the events with dijet traveling through the center of the medium to study the low-p_T enhancement at large angeles from the jets. Then, we perform the simulations of a number of dijets events and study the low-p_T enhancement after averaging over the triggered dijet events.

The thesis is organized as follows. In Chap. 2, the overview of the HIC is given. Some topics in HIC related to this thesis are also picked up and reviewed with the theoretical models and the experimental results. The formulation of the hydrodynamic model with source terms is presented in Chap. 3. Our hydrodynamic model consists of the relativistic hydrodynamic equation with source term, initial condition, equation of state and freezeout. In Chap. 4 we first perform a simulation in the case of the dijet traveling through the center of the expanding medium to study the typical flow structures induced by the dijet. In Chap. 5 we performe more realistic simulations by considering the the spacial distribution of the jet production points, the initial momentum distribution of the jets and trigger threshold. Chap. 6 is devoted to summary and concluding remarks. The thesis has appendices for supplemental information. A brief explanation of the coordinate system used in HIC is given in Appendix A. In Appendix B, we show the details of the numerical method which we employed for the hydrodynamics calculations in full $(3+1)$-dimensional Milne Coordinates.

The formulation presented in Chap. 3, the whole works in Chap. 4 and in Chap. 5 are

based on our original works in collaboration with Tetsufumi Hirano (Sophia Univ.) [29]. In the works, based on discussions with the collaborator, the author carried out the formulation, the implementation of the programs and the analysis. The codes for solving the the ideal hydrodynamic equations in fully $(3+1)$-dimensional Milne coordinates are developed by the author himself.

Chapter 2

Background

2.1 Heavy Ion Collisions

The strong interaction is one of the four fundamental interactions of nature, the others being the electromagnetic interaction, the weak interaction and the gravitational interaction. As its name suggests, the strong interaction is the strongest among the four fundamental interactions and described by the quantum chromodynamics (QCD) for quarks and gluons with color charges. According to QCD, colored charged particles cannot be observed as isolated particles under ordinary conditions (color confinement) [38], which is one of the most fundamental features of QCD. On the other hand, the quarks and gluons are deconfined at extremely high temperature [39, 40]. The quark-gluon plasma (QGP) is the deconfined state of quarks and gluons and supposed to have filled the universe a few microseconds after the Big Bang. As experimental exploration, heavy ion collisions (HIC) are conducted to create the QGP in the laboratories.

In the HIC, extremely high-temperature is achieved by a head-on collision of two heavy nuclei accelerated nearly at the speed of light. As a result, QGP is produced at sufficiently high center of mass energy per nucleon-nucleon collision $\sqrt{s_{NN}}$ [41, 42, 43, 44]. HIC are presently carried out at Relativistic Heavy Ion Collider (RHIC) in Brookhaven National Laboratory (BNL) for Au-Au collisions at $\sqrt{s_{NN}} = 200$ GeV and Large Hadron Collider (LHC) in CERN for Pb-Pb collisions at $\sqrt{s_{NN}} = 2.76$ TeV. Fig. 2.1 shows the schematic picture of the space-time evolution of hot matter created in HIC:

1. Before the collision, the two heavy nuclei move nearly at the speed of light. In the the laboratory frame, the nuclei are Lorentz-contracted in the direction of the collision axis due to the large Lorentz dilation factor: $\gamma \sim 100$ at RHIC energy $\sqrt{s_{NN}} = 200$ GeV and $\gamma \sim 1500$ at LHC energy $\sqrt{s_{NN}} = 2.76$ TeV.

2. The two incoming nuclei collide at $\tau = 0$. Then, the hot medium is created between the two outgoing nuclei. The medium is composed of deconfined particles with color charges (mainly gluons) and it is in non-equilibrium state for short proper time after the collision.

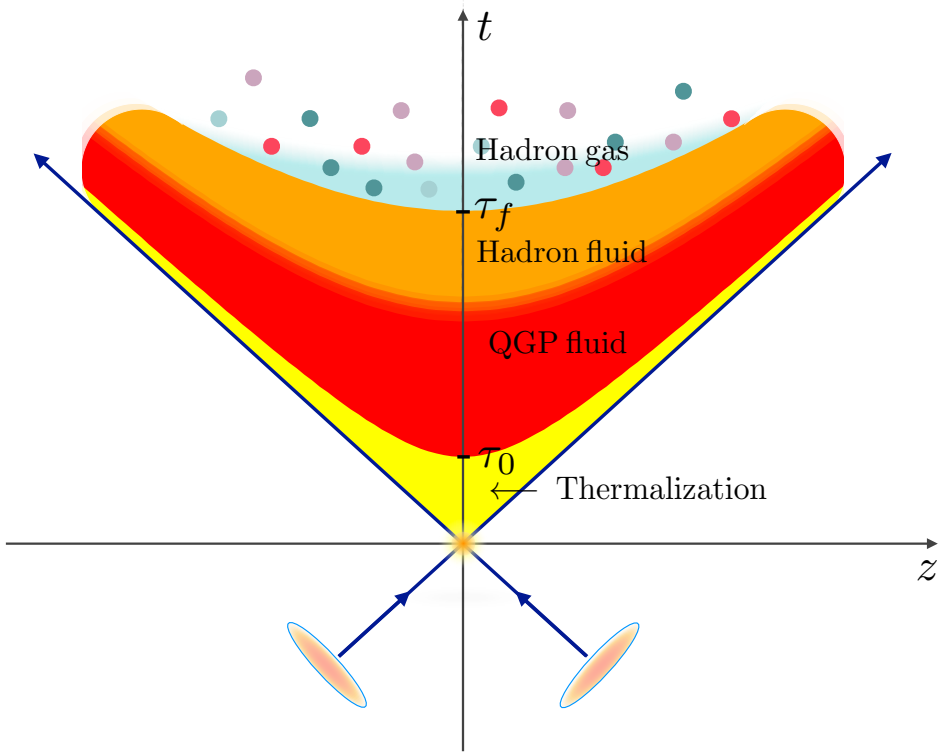

Figure 2.1: Schematic representation of space-time evolution of the hot matter in HIC. The vertical axis is time t and the horizontal axis is the longitudinal coordinate z (the collision axis).

3. The experimental data in HIC supports the local thermalization of the hot medium at an early proper time $\tau = \tau_0 < 1$ fm/c. The mechanism of the early thermalization is not fully understood and still a big mystery. The hot thermalized matter is called QGP which expands with relativistic velocity. From the analysis of experimental data of anisotropic azimuthal distribution in the momentum space, it has turned out that the QGP behaves as a nearly perfect fluid [2, 3, 4, 5, 6]. Therefore, the relativistic hydrodynamics is a powerful tool to describe the space-time evolution of the QGP fluid. So-called "hydrodynamic models" for HIC start by setting up the initial condition for the hydrodynamic equations at $\tau = \tau_0$. After that, the thermodynamic variables of the QGP fluid at every moment are calculated by solving the relativistic hydrodynamic equation together with the equation of the state.

4. The QGP fluid cools down while expanding and turns into a hadronic fluid. In hydrodynamic models for HIC, this hadronization occurs according to the equation of state employed in the hydrodynamical calculations.

5. After the hadronization, the medium keeps expanding and is diluted. As a result, the hydrodynamics becomes no longer applicable. of space-time evolution of the medium This

is called kinetic freezeout. In hydrodynamic models, the hydrodynamic description is switched to a particle picture for the weekly-interacting hadron gas at the kinetic freeze-out. The most popular method is to assume that the kinetic freezeout occurs when the temperature becomes below the freezeout temperature T_f. The phase space distribution function of the weekly-interacting hadron gas obtained from the thermodynamic variables of the fluid at T_f by employing the Cooper-Frye formula [45].

6. The weakly-interacting particles in the hadron gas after the kinetic freezeout scatter with each other or decay during their evolution before detections. The space-time evolution of the hadron gas (hadronic cascade) is described by the hadronic transport models. So-called "hybrid models" for HIC describe not only the hydrodynamical evolution of the medium but also the hadronic cascade by employing transport models such as the Jet AA Microscopic transport model (JAM) [46, 47] or the Ultra-relativistic Quantum Molecular Dynamics model (UrQMD) [48, 49]. Since the hadronic cascade plays important roles especially in spectra for identified particle species, hadronic transport models are essential to compare the theoretical predictions with experimental data.

A heavy-ion collision event consists of the various stages as shown above and the information of all the stage of the medium evolution is encoded in the hadron spectra in the final state. The transition between different stages are complex problem. Furthermore, not only the evolution of the medium but also other phenomena, e.g. jet quenching, J/ψ suppression, thermal photon emission, *etc.*, are involved in a heavy-ion collision event.

2.2 Collective Dynamics

The medium created in the HIC is not static and the information of its space-time evolution is encoded in the hadron spectra in the final state. Especially, the azimuthal distribution of particle emission in non-central collisions is strongly related to the bulk behavior of the medium.

In the non-central nucleus-nucleus collisions, the overlapped region of the two colliding nuclei does not have the rotational symmetry along the beam axis. The shape of the matter created in the collisions in the transverse plane to the beam axis is rather elliptic. The azimuthal distribution $\frac{dN}{d\phi_p}$ for a non-central collision is shown in Fig. 2.2. The figure illustrates the two situations in which the mean free path of the constituents in the medium is (a) much longer and (b) much shorter than the typical scale of the medium. In the situation (a), the constituents can move freely without interaction and are spread out isotropically regardless of the medium profile. In the situation (b), on the other hand, the medium behaves as a fluid and its space-time evolution is described by hydrodynamics. The anisotropic pressure gradient associated with the initial elliptic profile of the matter induces the anisotropic collective flow: The pressure gradient in direction of a minor axis of the initial elliptic profile is steeper than that in a major axis direction, then the medium strongly expands in a minor axis direction. As a result, the

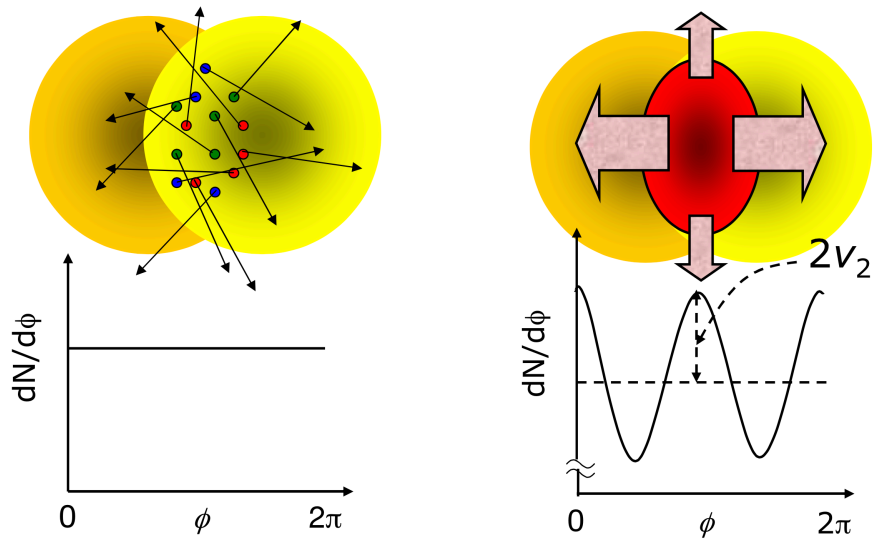

(a) Long mean free path (b) Short mean free path

Figure 2.2: Schematic illustration of the azimuthal distribution $\frac{dN}{d\phi_p}$ for a non-central collision. Two situations in which the mean free path of the constituents in the medium is much longer (a) and much shorter (b) than the typical scale of the medium are shown. (Figure from Ref.[50].)

azimuthal distribution $\frac{dN}{d\phi_p}$ for a non-central collision becomes a periodic function with a period π. The amplitude of the periodic $\frac{dN}{d\phi_p}$ normalized by $\int d\phi_p \frac{dN}{d\phi_p}$ is given by

$$v_2 = \int d\phi_p \cos(2\phi_p) \frac{dN}{d\phi_p} \Big/ \int d\phi_p \frac{dN}{d\phi_p}, \tag{2.1}$$

where ϕ_p is the azimuthal angle of the particle. The quantity v_2 is called the *elliptic flow* and characterizes the anisotropy originating from the fluidity of the medium [51, 52]. The finite v_2 is actually measured in HIC. Figure 2.3 shows the transverse momentum dependence of the elliptic flow of π, K, p and Λ in 200 GeV Au+Au collisions at RHIC. Data measured by the STAR collaboration [54] and results of the (2+1)-dimensional ideal hydrodynamic calculation [53] is plotted. The ideal hydrodynamic model calculation explains well the elliptic flow in HIC qualitatively. The success of the hydrodynamics in HIC indicates the appearance of the bulk of strongly-coupled particles in HIC.

The azimuthal distribution of particle emission in HIC has not only the elliptic component but also the other components due to the stochastically determined arrangement of the nucleons in colliding nuclei [Fig. 2.4]. The Fourier harmonics v_n of the azimuthal distribution are defined as

$$v_n(p_T, y) = \int d\phi_p \cos(n\phi_p - n\psi_n) \frac{dN}{p_T dp_T d\phi_p dy} \Big/ \frac{dN}{p_T dp_T dy}, \tag{2.2}$$

where ψ_n is the azimuthal angle of the reaction plane for each v_n in the laboratory frame.

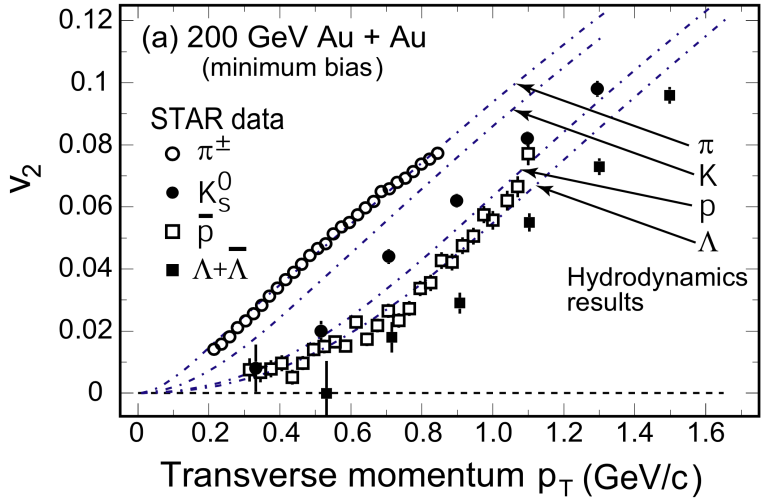

Figure 2.3: Transverse momentum dependence of the elliptic flow of π, K, p and Λ in $\sqrt{s_{NN}} =$ 200 GeV Au-Au collisions at RHIC. The dashed lines are the results of the ideal hydrodynamic calculations in Ref. [53]. The experimental data are measured by the STAR collaboration [54]. (Figure from Ref. [42].)

$v_n\left(p_T, y\right)$ is the coefficient of the Fourier expansion of the $\frac{dN}{p_T dp_T d\phi_p dy}$:

$$\frac{dN}{p_T dp_T d\phi_p dy} = \frac{1}{2\pi}\frac{dN}{p_T dp_T dy}\left[1 + 2\sum_n v_n\left(p_T, y\right)\cos\left(n\phi_p - n\psi_n\right)\right]. \tag{2.3}$$

The azimuthal angle of the reaction plane ψ_n is defined for each event and for each v_n as

$$\langle e^{in\phi_p}\rangle = v_n e^{in\psi_n}, \tag{2.4}$$

where the angle bracket denotes averaging over all particles in a single event [Fig. 2.4]. In various hydrodynamic models, the higher harmonics in HIC is studied by the event-by-event analysis with the initial condition generated by the models with the Monte Carlo method, *e.g.*, MC Glauber model [57, 58, 55], MC KLN model [59, 60], IP-Glasma model [61], *etc.* Fig. 2.5 shows the numerical results of the $(3+1)$-dimensional viscous hydrodynamic model with the IP-Glasma initial condition [62]. The hydrodynamic calculation with the shear viscosity to entropy ratio $\eta/s \simeq 0.2$ well reproduces all of v_2, v_3, v_4 and v_5 measured in HIC experiments qualitatively.

Thus, hydrodynamics describes successfully the space-time evolution of the strongly-coupled matter produced in HIC. The profile during the space-time evolution obtained from the hydrodynamic models is used as references in various calculations, *e.g.*, thermal photon emission, dilepton emission, jet quenching, *etc.*

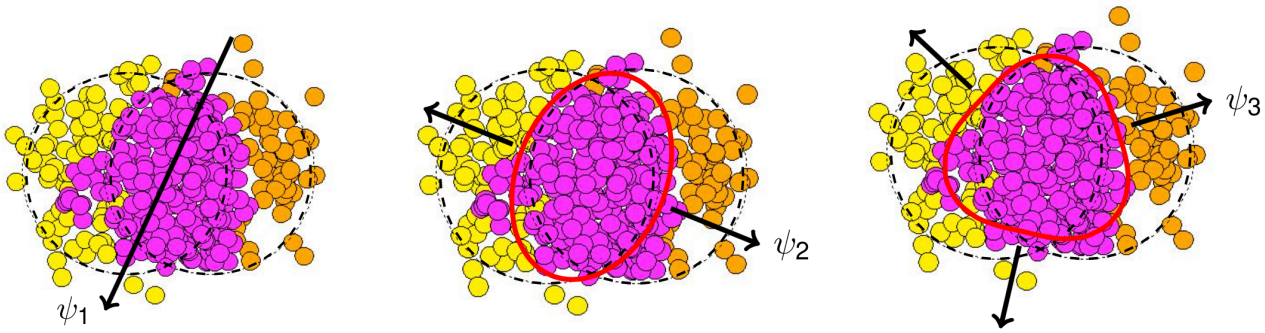

Directed Flow v_1 Elliptic Flow v_2 Triangular Flow v_3

Figure 2.4: Schematic representation of the arrangement of the nucleons in nuclei at the time of the collision generated by the calculation of the Monte Carlo (MC) Glauber model [55]. The azimuthal direction of the reaction plane for v_1, v_2 and v_3 are also shown. (Figure from Ref. [56].)

2.3 Glauber Model

The reaction of composite particles such as finite nuclei is usually a problem with high complexity. However, in sufficiently high energies, semi-classical picture of nucleus-nucleus scatterings, so-called the Glauber model [64, 65, 66, 57] can be applied. In the Glauber model, the nucleus-nucleus scattering are treated as multiple independent nucleon-nucleon scatterings. The nucleons in the nuclei are assumed to have sufficiently high momentum so that they travel in straight lines and are undeflected during the nucleus-nucleus collisions. The size of the nuclei is large compared to the scale of the interaction between nucleons so that the distribution of each nucleons in the nuclei is independently determined by a given density distribution. The nucleon density distribution of typical heavy nucleus used in HIC such as Au or Pb are well approximated by the Woods-Saxon distribution:

$$\rho(r) = \frac{\rho_0}{1 + \exp\left(\frac{r-R}{a}\right)}, \tag{2.5}$$

where ρ_0 is the nucleon density at the center of the nucleus, R is the nuclear radius and a is the skin depth of the nucleus. These parameters are $R = 6.38\,\text{fm}$, $a = 0.535\,\text{fm}$ for ^{197}Au and $R = 6.62\,\text{fm}$, $a = 0.546\,\text{fm}$ for ^{207}Pb. The Woods-Saxon nucleon distribution for ^{207}Pb is shown in Fig. 2.6.

Let us consider the geometry just before the collision in HIC [Fig. 2.7]. Nucleus A and B collide at relativistic speed along the z-axis with impact parameter $\boldsymbol{b}$. The thickness function, namely transverse distribution of the nucleon density, is obtained by integrating the density along beam axis, z. The thickness functions for nucleus A and B are

$$T_A(\boldsymbol{s}_A) = \int dz_A \rho_A(\boldsymbol{s}_A,\, z_A)\,, T_B(\boldsymbol{s}_B) = \int dz_B \rho_B(\boldsymbol{s}_B,\, z_B)\,. \tag{2.6}$$

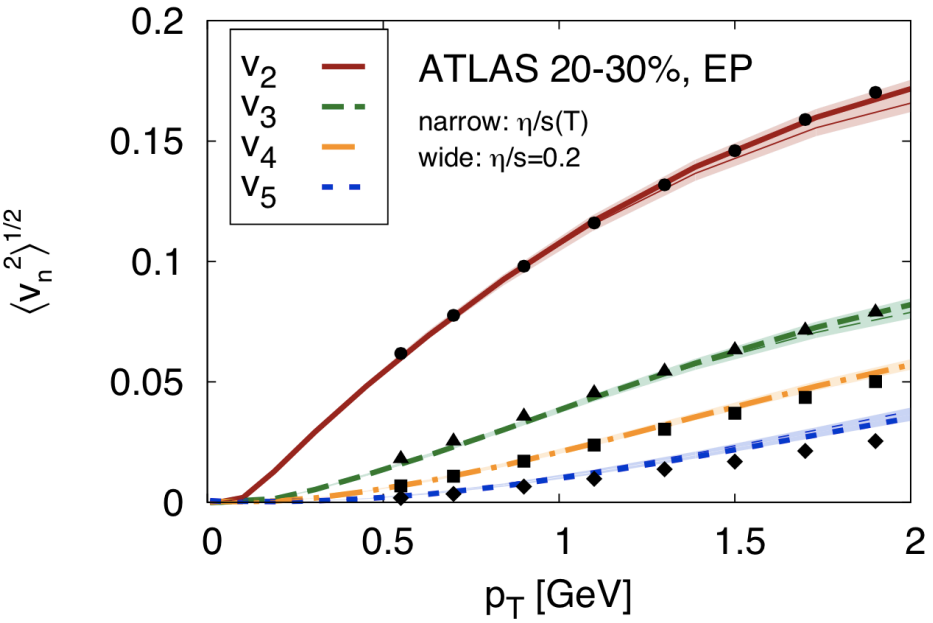

Figure 2.5: Transverse momentum dependence of v_2, v_3, v_4 and v_5 in $\sqrt{s_{NN}} = 2.76$ TeV Pb-Pb collisions at LHC for 20-30% centrality [62]. The lines are the results of the hydrodynamic calculations with the shear viscosity to entropy ratio $\eta/s = 0.2$ and the IP-Glasma initial conditions. The experimental data are measured by the ATLAS collaboration [63].

The nucleon densities ρ_A and ρ_B are normalized to their mass number A and B:

$$\int d^2 s_A T_A(\boldsymbol{s}_A) = \int d^3 r_A \rho_A(r_A) = A, \tag{2.7}$$

$$\int d^2 s_B T_B(\boldsymbol{s}_B) = \int d^3 r_B \rho_B(r_B) = B. \tag{2.8}$$

Let $\boldsymbol{r}_\perp$ denote any position in the overlap region of A and B in the transverse plane. The origin is set at the midpoint of A and B in the transverse plane. The joint probability density of nucleons in the overlap region is given by:

$$T_A\left(\boldsymbol{r}_\perp + \frac{\boldsymbol{b}}{2}\right) T_B\left(\boldsymbol{r}_\perp - \frac{\boldsymbol{b}}{2}\right). \tag{2.9}$$

Hence, the number density of binary collisions between the nucleons in the transverse plane is

$$n_{\text{coll}}^{\boldsymbol{b}}(\boldsymbol{r}_\perp) = T_A\left(\boldsymbol{r}_\perp + \frac{\boldsymbol{b}}{2}\right) T_B\left(\boldsymbol{r}_\perp - \frac{\boldsymbol{b}}{2}\right) \sigma_{\text{inel}}^{NN}, \tag{2.10}$$

where $\sigma_{\text{inel}}^{NN}$ is the cross section of the nucleon-nucleon inelastic collision. The examples of n_{coll} for Pb-Pb collision with impact parameters $b = 0$ and 6 fm are shown in Fig. 2.8. In HIC, the high momentum particles are produced from hard scatterings between the partons in the

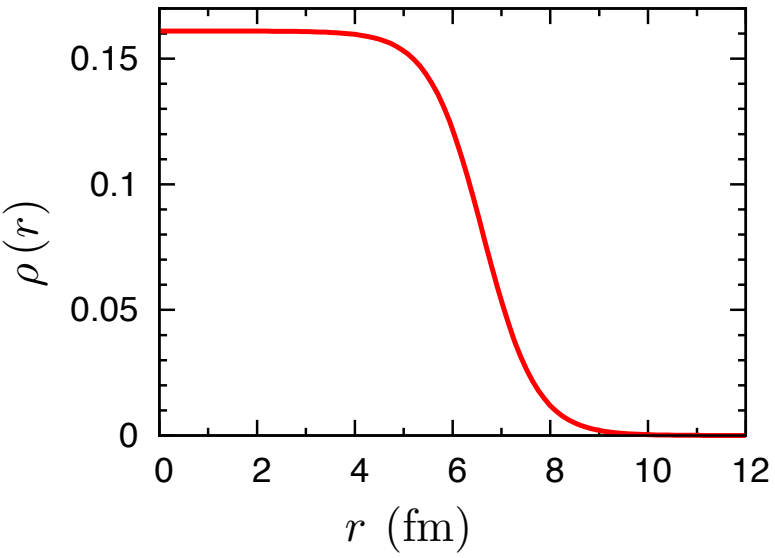

Figure 2.6: The Woods-Saxon nucleon distribution for ^{207}Pb. The parameters in the Woods-Saxon function are $R = 6.62$ fm and $a = 0.546$ fm.

initial stage, so their production mechanism is the same as the one in nucleon-nucleon collision. Therefore, the production rate for sufficiently high momentum particles can be scaled by the number of binary collisions between the nucleons, $N_{\rm coll} = \int d^2r_\perp n_{\rm coll}$.

The number density of participants, namely the nucleons in the colliding nuclei that interact, with impact parameter $\boldsymbol{b}$ is given by [67, 68]

$$n^{\boldsymbol{b}}_{\rm part}(\boldsymbol{r}_\perp) = T_A\left(\boldsymbol{r}_\perp + \frac{\boldsymbol{b}}{2}\right)\left\{1 - \left[1 - \frac{T_B(\boldsymbol{r}_\perp - \boldsymbol{b}/2)}{B}\sigma^{NN}_{\rm inel}\right]^B\right\} \tag{2.11}$$

$$+T_B\left(\boldsymbol{r}_\perp - \frac{\boldsymbol{b}}{2}\right)\left\{1 - \left[1 - \frac{T_A(\boldsymbol{r}_\perp + \boldsymbol{b}/2)}{A}\sigma^{NN}_{\rm inel}\right]^A\right\}. \tag{2.12}$$

In Fig. 2.9, the examples of $n_{\rm part}$ for Pb-Pb collision with impact parameters $b = 0$ and 6 fm are shown. The total charged multiplicities in HIC are almost scaled by the number of participants, $N_{\rm part} = \int d^2r_\perp n_{\rm part}$. In Fig. 2.10, The total charged multiplicities $N_{\rm ch}$ divided by $\langle N_{\rm part}/2\rangle$ are shown as functions of $N_{\rm part}$ [69]. Figure 2.10 demonstrates that $N_{\rm part}$ scaling holds well in HIC especially at lower energies. However, one can see that $\frac{N_{\rm ch}}{\langle N_{\rm part}/2\rangle}$ increases slightly with $N_{\rm part}$ at higher energies. This tendency is particularly notable in the mid rapidity region. Fig. 2.11 shows $dN_{\rm ch}/d\eta|_{\eta=0}$ normalized by $\langle N_{\rm part}/2\rangle$ observed by the PHENIX Collaboration, $\sqrt{s_{NN}} = 130$GeV [70]. It is conceivable that this deviation from $N_{\rm part}$ scaling is originating from the contribution of the hard processes on the particle production. To include the contribution of the hard processes, a simple linear combination of $N_{\rm part}/2$ and $N_{\rm coll}$ is usually used as the fitting function of the experimental results [71, 72] :

$$\left.\frac{dN_{\rm ch}}{d\eta}\right|_{\eta=0} \propto \frac{(1-\alpha)}{2}N_{\rm part} + \alpha N_{\rm coll}. \tag{2.13}$$

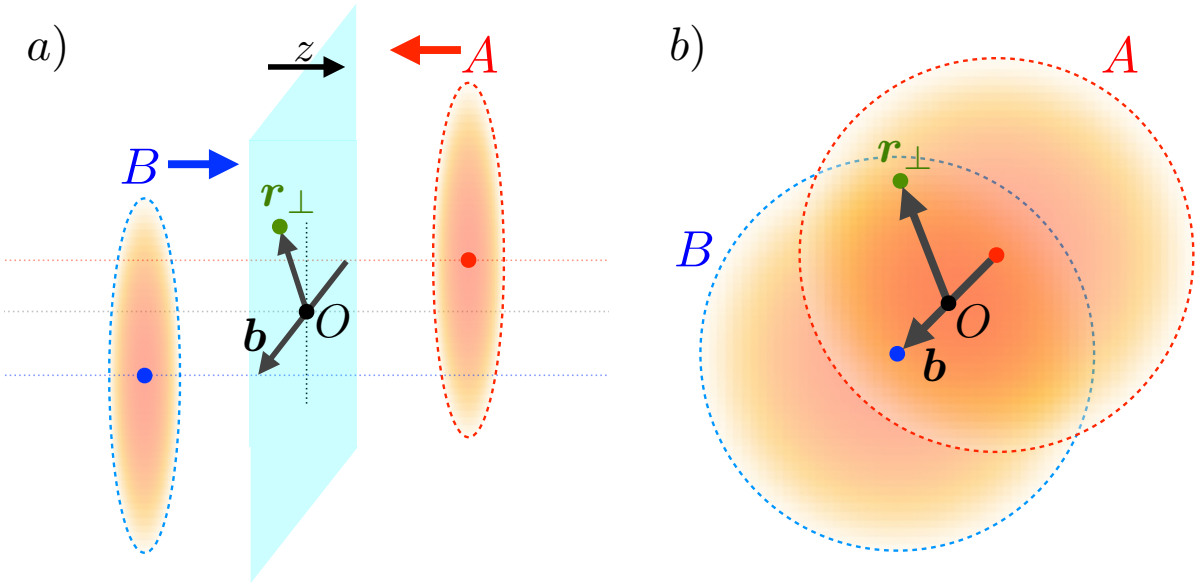

Figure 2.7: Geometry of a nucleus-nucleus collision. a) View transverse to the beam axis. b) View parallel to the beam axis.

The initial entropy density for the hydrodynamic model is taken to be proportional to the similar linear combination of $n_{\rm part}/2$ and $n_{\rm coll}$ [51, 73, 74]:

$$s\left(\tau=\tau_0,\ \eta_{\rm s}=0,\ \boldsymbol{r}_\perp\right)=\left.\frac{dS}{\tau_0 d\eta_{\rm s} d^2r_\perp}\right|_{\eta_{\rm s}=0}\propto\frac{(1-\alpha)}{2}n_{\rm part}\left(\boldsymbol{r}_\perp\right)+\alpha n_{\rm coll}\left(\boldsymbol{r}_\perp\right), \tag{2.14}$$

where τ_0 is the initial proper time for the QGP fluid and $\eta_{\rm s}$ is the space-time rapidity. The QGP fluid created in HIC evolves almost adiabatically, because of its extremely small viscosity. Furthermore, its profile is approximately boost invariant especially at mid-rapidity. As a result, the "space-time" rapidity density of entropy $dS/d\eta_{\rm s}$ is an almost conserved quantity. From the thermodynamical relation and the boost invariance, one may assume that $dN_{\rm ch}/d\eta \sim dN_{\rm ch}/d\eta_{\rm s} \propto dS/d\eta_{\rm s}(\tau_f) = dS/d\eta_{\rm s}(\tau_0)$. This supports the use of Eq. (2.14) to estimate the initial entropy density. The full profile of the initial entropy density for the hydrodynamical calculation is assumed as following:

$$s\left(\tau_0,\ \eta_{\rm s},\ \boldsymbol{r}_\perp\right)=\frac{C}{\tau_0}\theta\left(Y_{\rm beam}-|\eta_{\rm s}|\right)H\left(\eta_s\right)\left[\frac{(1-\alpha)}{2}n_{\rm part}\left(\boldsymbol{r}_\perp\right)+\alpha n_{\rm coll}\left(\boldsymbol{r}_\perp\right)\right], \tag{2.15}$$

where $Y_{\rm beam}$ is the beam rapidity and $H\left(\eta_{\rm s}\right)$ represents the profile in the $\eta_{\rm s}$-direction. $H\left(\eta_{\rm s}\right)$ The profile in the $\eta_{\rm s}$-direction is usually assumed to be flat at mid-rapidity like the Bjorken model [75]. At both ends of the flat region, half Gaussians smoothly connected to a vacuum are used [76, 77, 78, 79, 80]:

$$H\left(\eta_s\right) \ = \ \exp\left[-\frac{\left(|\eta_s|-\eta_{\rm flat}/2\right)^2}{2\sigma_\eta^2}\theta\left(|\eta_s|-\frac{\eta_{\rm flat}}{2}\right)\right], \tag{2.16}$$

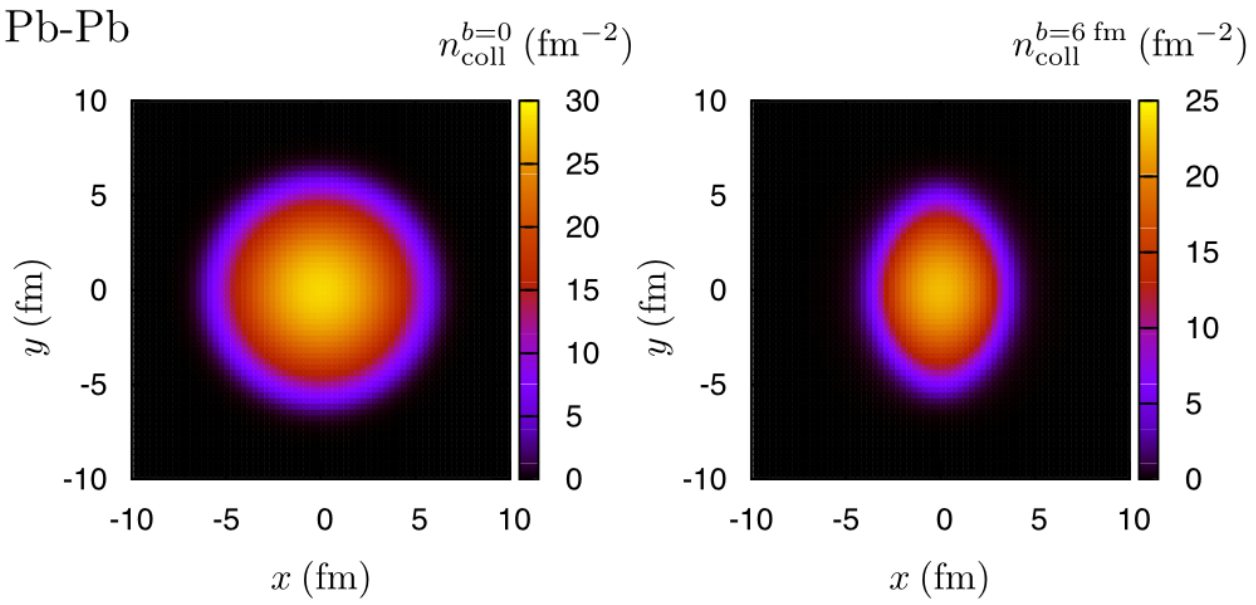

Figure 2.8: The number density of binary collisions between the nucleons calculated from equation (2.10) for Pb-Pb collision with impact parameters $b = 0$ (left) and 6 fm (right).

where $\eta_{\rm flat}$ and σ_η are the rapidity length of the flat region and the width of the Gaussians, respectively.

To introduce the effect of the difference between the $n_{\rm part}(\boldsymbol{r}_\perp)$ in the two colliding nuclei, $n_{\rm part}$ in Eq. (2.15) is replaced by [81, 82]

$$n_{\rm part} = \frac{Y_{\rm beam} - \eta_{\rm s}}{Y_{\rm beam}} n_{\rm part}^A + \frac{Y_{\rm beam} + \eta_{\rm s}}{Y_{\rm beam}} n_{\rm part}^B, \tag{2.17}$$

$$n_{\rm part}^A = T_A\left(\boldsymbol{r}_\perp + \frac{\boldsymbol{b}}{2}\right)\left\{1 - \left[1 - \frac{T_B\left(\boldsymbol{r}_\perp - \boldsymbol{b}/2\right)}{B}\sigma_{\rm inel}^{NN}\right]^B\right\}, \tag{2.18}$$

$$n_{\rm part}^B = T_B\left(\boldsymbol{r}_\perp - \frac{\boldsymbol{b}}{2}\right)\left\{1 - \left[1 - \frac{T_A\left(\boldsymbol{r}_\perp + \boldsymbol{b}/2\right)}{A}\sigma_{\rm inel}^{NN}\right]^A\right\}. \tag{2.19}$$

At $\eta_{\rm s} = 0$, Eq. (2.19) reduces to Eq. (2.12). By introducing the trapezoidal weight, which breaks the longitudinal boost invariance at mid-rapidity region, the pseudorapidity distribution $dN_{\rm ch}/d\eta$ in the collisions between two different nuclei can be reproduced. The parametrization given by Eqs. (2.15), (2.16) and (2.19) is called the modified BGK initial condition [83].

2.4 Jet Quenching

In HIC, the high-p_T particles produced in the initial scattering between the partons in the colliding nuclei traverse the QGP medium [Fig. 2.12]. The spectra of high-p_T particles is

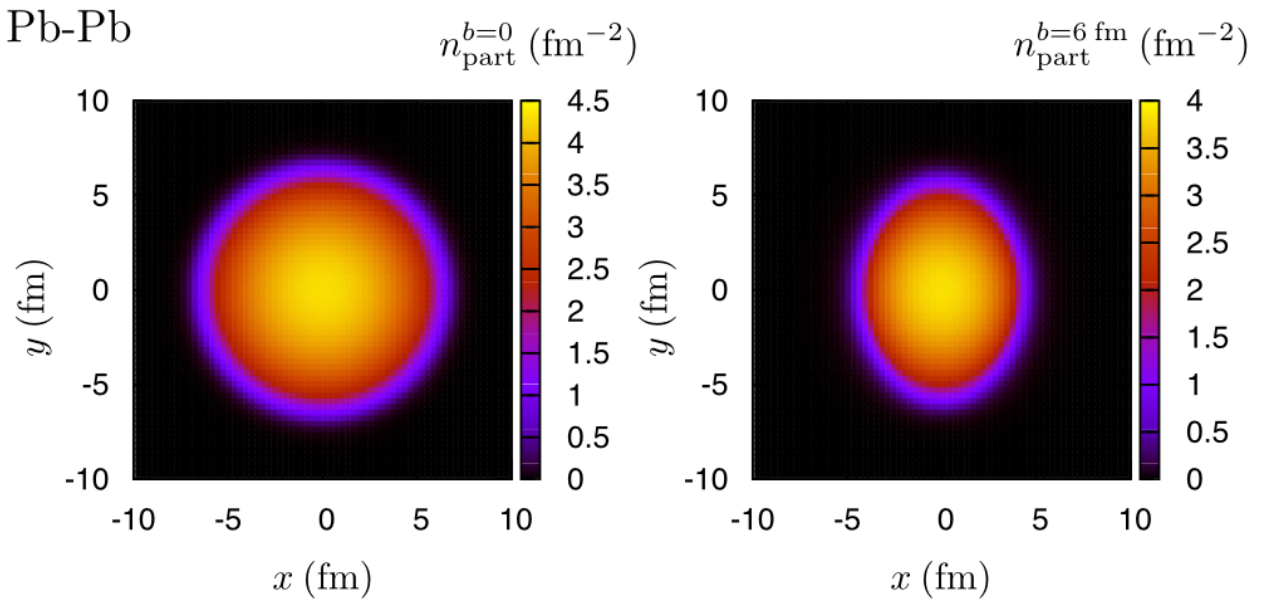

Figure 2.9: The number density of participants calculated from equation (2.12) for Pb-Pb collision with impact parameters $b = 0$ (left) and 6 fm (right).

modified from the ones without the medium by the effect of the interaction with the medium during their traveling. This phenomenon is called the *jet quenching* and provides insight into the properties of the QGP in HIC.

2.4.1 Hard Processes in HIC

Non-perturbative long-distance contributions are always involved in partonic reactions in nucleon-nucleon collisions and in HIC because all partons are confined in hadrons at both the initial and the final states. On the other hand, the cross section of short-distance hard processes between partons, in which large momenta are exchanged, can be calculated in perturbative QCD, owing to asymptotic freedom. By the factorization theorem of QCD, the cross section for the production of high-p_T hadron in nucleon-nucleon collisions can be separated into the long- and short-distance contributions [Fig. 2.13, left]:

$$\sigma_{AB\to h} = f_A\left(x_a,\, Q^2\right) \otimes f_B\left(x_b,\, Q^2\right) \otimes \sigma_{ab\to ij}\left(x_a,\, x_b,\, Q^2\right) \otimes D_{j\to h}\left(z,\, Q^2\right), \tag{2.20}$$

where $\sigma_{ab\to ij}\left(x_a,\, x_b,\, Q^2\right)$ is the short-distance cross section of the elementary process, $ab \to ij$, calculable in perturbative QCD, the other parts in the right-hand side are non-perturbative quantities: $f_A\left(x_a,\, Q^2\right)$ and $f_B\left(x_b,\, Q^2\right)$ are parton distribution functions (PDF) representing the structure of the colliding particles in terms of quarks and gluons. PDF, $f_A\left(x_a,\, Q^2\right)$, can be interpreted as the probability to find a parton a with momentum fraction x_a inside the colliding

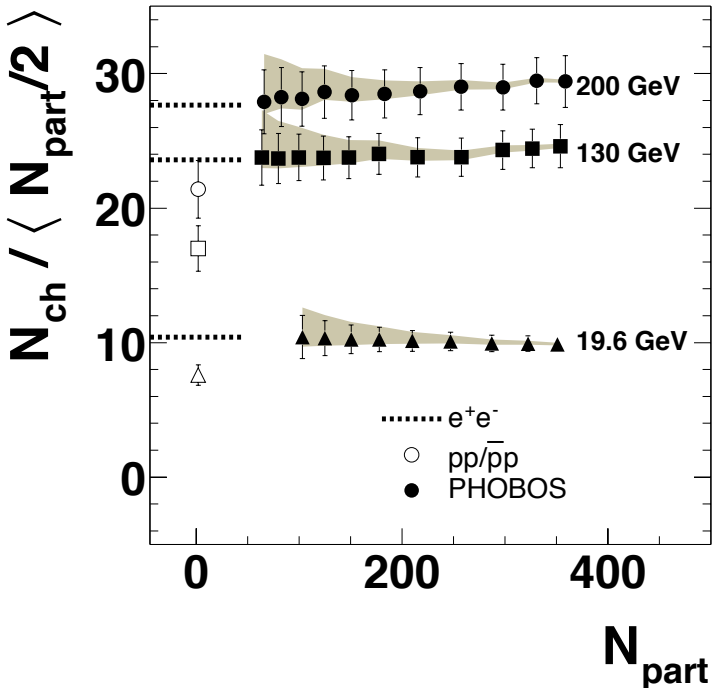

Figure 2.10: $N_{\rm ch}/\langle N_{\rm part}/2\rangle$ against $N_{\rm part}$ for $\sqrt{s_{NN}}$ = 19.6, 130, 200 GeV Au-Au collisions [69].

particle A. $D_{j\to h}\left(z,\, Q^2\right)$ is the fragmentation function (FF) describing the hadronization process of the parton j into the hadron h with momentum fraction z in the final state. PDF and FF for proton-proton collisions are obtained by the global fitting various experimental data, such as deep inelastic scattering and e^+-e^- annihilation, using the Dokshitzer-Gribov-Lipatov-Altarelli-Parisi (DGLAP) evolution equations [85, 86, 87, 88]:

$$t\frac{\partial D\left(x,\, t\right)}{\partial t} = \int_x^1 \frac{dz}{z}\frac{\alpha_s}{2\pi} P\left(z\right) D\left(\frac{x}{z},\, t\right), \tag{2.21}$$

where $t = \mu_F^2$, μ_F is the factorization scale, $\alpha_s = g/(4\pi)$ is the strong coupling constant, $D\left(x,\, t\right)$ can be either the PDF or the FF and $P\left(z\right)$ is the splitting function [89].

In HIC, the factorization formula (Eq. (2.20)) must be modified due to the presence of the QGP medium. Since the short-distance processes take place before the creation of the medium [Fig. 2.13, right], only the FF is modified by the medium effects:

$$\sigma_{AB\to h} = f_A\left(x_1,\, Q^2\right) \otimes f_B\left(x_2,\, Q^2\right) \otimes \sigma_{ab\to ij}\left(x_1,\, x_2,\, Q^2\right) \otimes D^{med}_{j\to h}\left(z,\, Q^2\right). \tag{2.22}$$

In HIC, the high-p_T partons are created as well as in nucleon-nucleon collisions, and then propagate through the QGP medium. The FF modified by the medium effect D^{med} is subject to the DGLAP equation with the medium effect during the propagation:

$$t\frac{\partial D^{med}\left(x,\, t\right)}{\partial t} = \int_x^1 \frac{dz}{z}\frac{\alpha_s}{2\pi} P^{med}\left(z\right) D^{med}\left(\frac{x}{z},\, t\right). \tag{2.23}$$

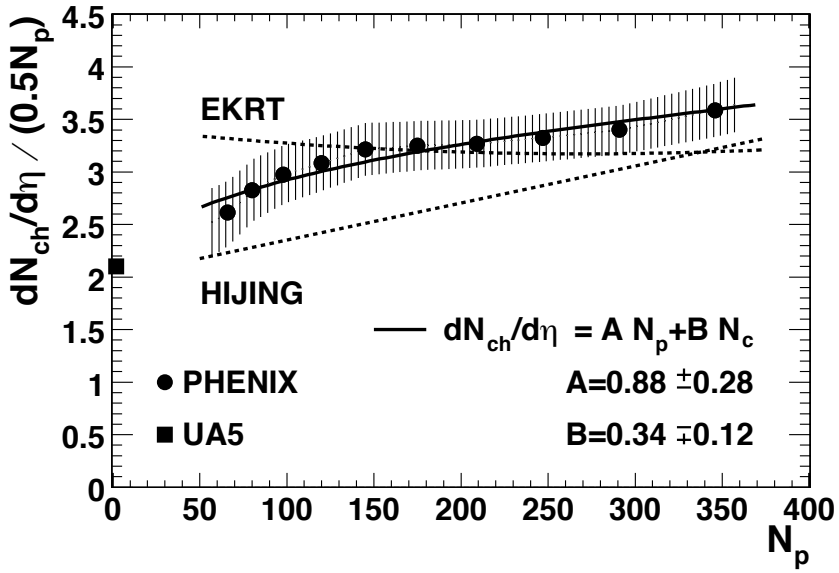

Figure 2.11: The pseudorapidity density of the charged particle at mid rapidity ($|\eta| < 0.35$) as a function of $N_{\rm part}$ measured by the PHENIX Collaboration at RHIC, $\sqrt{s_{NN}} = 130$ GeV [70]. The data are fitted by equation (2.13) with $\alpha = 0.16$ (solid line).

As the initial condition for the DGLAP equation of D^{med}, the the same value as the FF without the medium effect D^{vac} is used, *i.e.* $D^{med}(x,\, Q_0^2) = D^{vac}(x,\, Q_0^2)$ [90, 91]. In this procedure, it is assumed that at sufficiently large scale, $Q^2 = Q_0^2$, the hadronization process is completed before affected by the medium because of the very large transverse momentum. So, all the QGP medium effect in HIC is encoded in the FF through the medium-modified splitting function in the DGLAP equation (2.23):

$$P^{med}(z) = P^{vac}(z) + \Delta P(z,\, t)\,, \tag{2.24}$$

where P^{vac} is the same function as P in Eq. (2.21) and ΔP^{med} is the additional contribution to take into account the interaction with the QGP medium during the propagation [92]. As a result, the information about interaction between the propagating hard partons and the QGP medium are encoded in the spectra of high-p_T hadrons in the final state. Though the factorization formula for HIC has not been proven but is simply assumed at the moment, it is well supported by various experimental data compared with the ones in p-p collisions.

2.4.2 Parton Energy Loss in HIC

The high-p_T partons, produced from early stage hard scatterings, do not participate in the local thermalized fluid but traverse the fluid, because of their large transverse momenta. During traversing the QGP-fluid, the high-p_T partons strongly interact with constituent partons of the QGP fluid. In the QGP medium, the high-p_T partons are supposed to lose their energy via the interactions such as the elastic collisions and the medium-induced radiation [Fig. 2.14)]. This phenomenon is called the *jet quenching* [7, 8, 9, 10, 11, 12, 13].

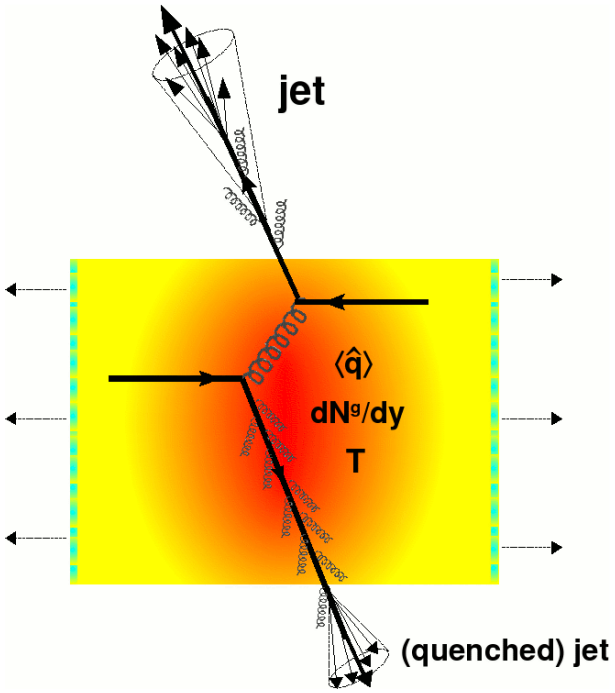

Figure 2.12: Schematic illustration of the high-p_T parton traversing the QGP medium in HIC. Figure from [84]

The idea of parton energy loss in the QGP medium was first proposed by Bjorken in 1982 [7]. He considered elastic scatterings with the thermalized partons in the QGP medium. The energy loss of the high-p_T partons via the elastic scatterings is called the collisional energy loss and is given by [7, 12, 93, 94];

$$\left.\frac{dE}{dt}\right|_{\rm col} = 2\pi C_R \alpha_s^2 T^2 \left(1 + \frac{N_f}{6}\right) \log \frac{\sqrt{4ET}}{m_D}. \tag{2.25}$$

Here, E is the energy of the high-p_T parton, C_R is the Casimir operator taking its value $C_R = C_A = 3$ where the the high-p_T parton is a gluon and $C_R = C_F = 4/3$ where the the high-p_T parton is a quark, T is the temperature of the medium, N_f is the number of quark flavors in the medium, and $m_D = \sqrt{(1 + N_f/6)}\, gT$ is the Debye color-screening mass of the gluons in the QGP medium.

Especially for the light flavor partons with large momentum, the energy loss due to medium-induced radiation is supposed to be much larger than the one due to the collisional energy loss. Radiative energy loss has been studied in various formalisms with different assumptions; Baier-Dokshitzer-Mueller-Peigne-Schiff and Zakharov (BDMPS-Z) [95, 96, 97, 98, 99], Amesto-Salgado-Wiedemann (ASW) [100, 101, 102], Arnold-Moore-Yaffe (AMY) [103, 104, 105, 106], Gyulassy-Levai-Vitev (GLV) [107, 108] and higer twist (HT) [92, 109]. Radiated gluons carry

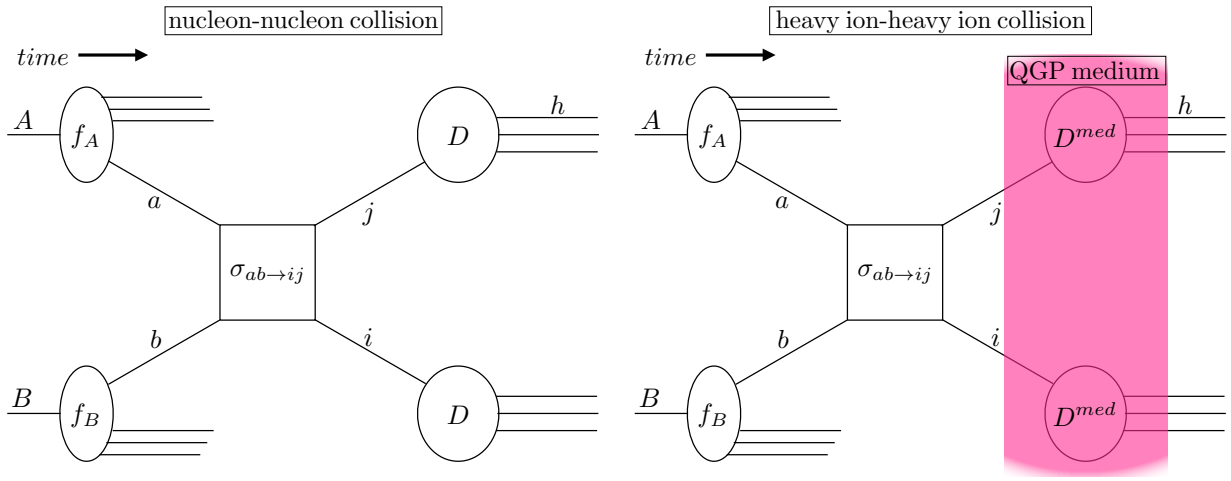

Figure 2.13: Feynman diagrams for hard processes in nucleon-nucleon collision (left) and in heavy ion-heavy ion collision (right). f_A and f_B are parton distribution functions and $\sigma_{ab\to ij}$ is the cross section of the short-distance process, $ab \to ij$. D and D^{med} are fragmentation functions in the vacuum and in the QGP medium, respectively. The colored region indicates the region where the presence of the medium affects the hard processes in HIC.

away energies and momenta from the leading parton. The radiative energy loss is given by

$$\langle \Delta E \rangle = \int d(\Delta E)\ \Delta E\, P(\Delta E)\,. \tag{2.26}$$

Here, ΔE is an averaged total energy carried away by radiated gluons and $P(\Delta E)$ is the probability distribution of parton energy loss. Assuming that successive gluon emissions are independent, the Poisson distribution is commonly employed for $P(\Delta E)$:

$$P(\Delta E) = \exp\left[-\int_0^\infty d\omega \frac{dI}{d\omega}\right] \sum_{n=0}^{\infty} \frac{1}{n!} \left[\prod_{i=1}^{n} \int d\omega_i \frac{dI(\omega_i)}{d\omega}\right] \delta\left(\Delta E - \sum_{i=1}^{n} \omega_i\right), \tag{2.27}$$

where $dI/d\omega$ is the spectrum of radiated gluons with energy ω. In BDMPS-Z formalism, the spectrum is

$$\omega \frac{dI_{\mathrm{BDMPS-Z}}}{d\omega} = \frac{2\alpha_s C_R}{\pi} \log\left|\cos\left[(1+i)\sqrt{\frac{\omega_c}{\omega}}\right]\right| \tag{2.28}$$

$$\simeq \frac{2\alpha_s C_R}{\pi} \begin{cases} \sqrt{\frac{\omega_c}{\omega}} & \text{for} \quad \omega \ll \omega_c, \\ \frac{1}{3}\left(\frac{\omega_c}{\omega}\right)^2 & \text{for} \quad \omega \gg \omega_c. \end{cases} \tag{2.29}$$

Here, ω_c is the characteristic gluon energy and its definition is given by

$$\omega_c \equiv \frac{1}{2}\hat{q}L^2, \tag{2.30}$$

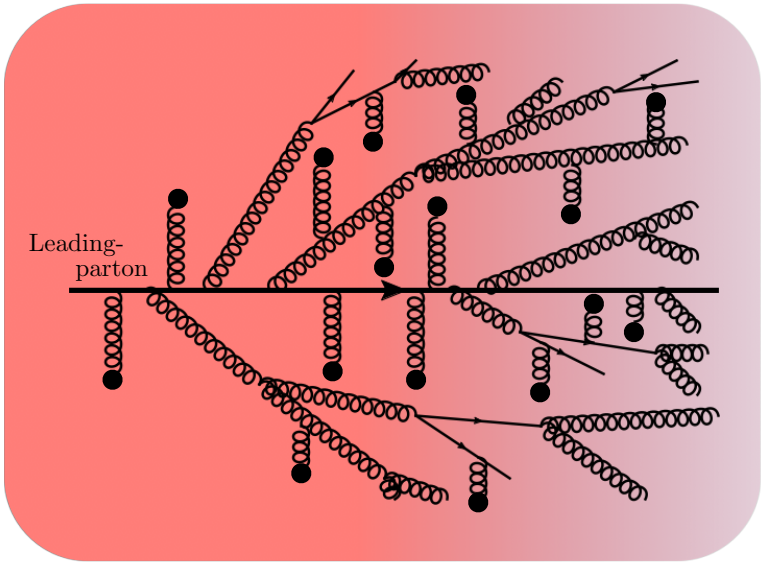

Figure 2.14: Schematic illustration of the high-p_T parton traveling through the QGP medium. The medium strongly interacts with the high-p_T parton (leading parton) and induces gluon radiation.

where $\hat{q}$ is the jet quenching parameter and L is the path length in the medium. The jet quenching parameter can be interpreted as a diffusion coefficient in $k_\perp$-space; $\hat{q} = \langle k_\perp^2 \rangle / L$. Here, $k_\perp$ is momentum transverse to the direction of the leading parton. All the information about the properties of the medium is encoded in $\hat{q}$. From Eqs. (2.26), (2.27) and (2.29), the total radiative energy loss in BDMPS-Z formalism is

$$\langle \Delta E \rangle_{\mathrm{BDMPS-Z}} = \int_0^\infty d\omega \omega \frac{dI_{\mathrm{BDMPS-Z}}}{d\omega} = \alpha_s C_R \omega_c = \frac{\alpha_s C_R}{2} \hat{q} L^2. \tag{2.31}$$

We can see so-called L^2-dependence of the radiative energy loss in Eq. (2.31).

The effect of the parton energy loss in HIC experiments can be extracted from the measurements of the nuclear modification factor;

$$R_{AA}\left(p_T,\, \eta_p\right) = \frac{1}{\langle N_{coll} \rangle} \frac{dN_{ch}^{AA}}{dp_T d\eta_p} \Big/ \frac{dN_{ch}^{pp}}{dp_T d\eta_p}\,, \tag{2.32}$$

where $\langle N_{coll} \rangle$ is the averaged number of binary collisions in A-A collisions, N_{ch}^{AA} and N_{ch}^{pp} are the number of charged particles in nucleus-nucleus collisions and in proton-proton collisions, respectively. If the spectra are not modified by the medium, R_{AA} would be consistent with unity. Figure 2.15 shows the nuclear modification factor measured by the ALICE collaboration in HIC at LHC. It is found that R_{AA} in the central (0-5%) collisions is small compared to the one in the peripheral (70-80%) collisions at high-p_T region. As collisions become more peripheral, the size of the created medium is supposed to become smaller. As a result, there is almost no modification on the high-p_T particles by the medium and R_{AA} is almost equal

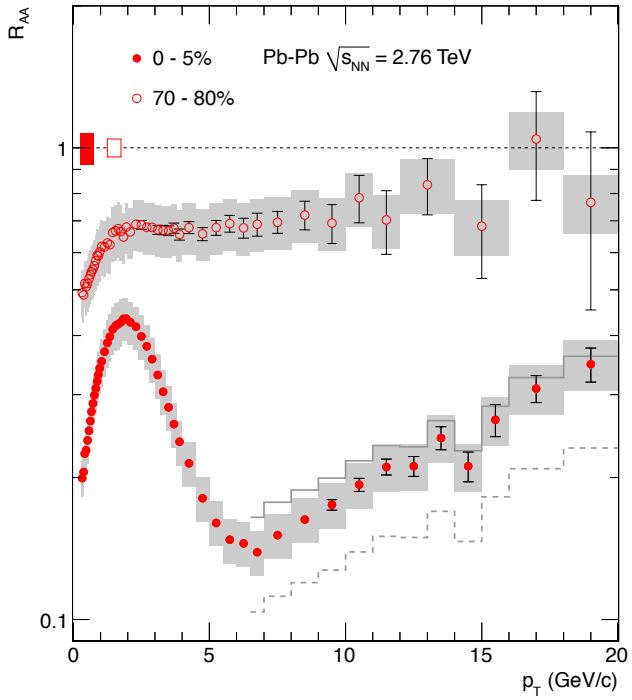

Figure 2.15: Nuclear modification factor R_{AA} measured in central (0-5%) and peripheral (70-80%) Pb-Pb collisions as a function of transverse momentum p_T at LHC energy $\sqrt{s_{NN}} = 2.76\,\text{TeV}$ [110].

to 1 at high-p_T region in the peripheral (70-80%) collisions. On the other hand, the high-p_T particles in the central (0-5%) collisions are strongly suppressed by the medium. If partons lose their energy by the medium effect, the spectra are shifted to the low-p_T direction. Then, the particles in high-p_T region are depressed because the spectra in hadron-hadron collisions are steeply decreasing functions of p_T. Therefore, the high-p_T suppression in HIC shown above is a consequence of the parton energy loss in the QGP medium.

2.4.3 Dijet Asymmetry in HIC

In the leading order, high-p_T partons are produced as a pair in opposite azimuthal directions with equal transverse momenta due to the energy momentum-conservation. Sufficiently high-p_T partons are hadronized through the fragmentation processes and detected as back-to-back pairs of jets, namely collimated clusters of high-p_T hadrons, in the final state in relativistic collision experiments.

In recent Pb-Pb experiments at LHC, thanks to its high center of mass energy $\sqrt{s_{NN}} = 2.76\,\text{TeV}$ per nucleon-nucleon collision, detailed measurements of fully reconstructed jets with transverse momenta $p_T^{\text{jet}} > 100\,\text{GeV}/c$ has become available. A large number of dijet events, namely events with two very high-p_T triggered jets in an opposite direction each other, are

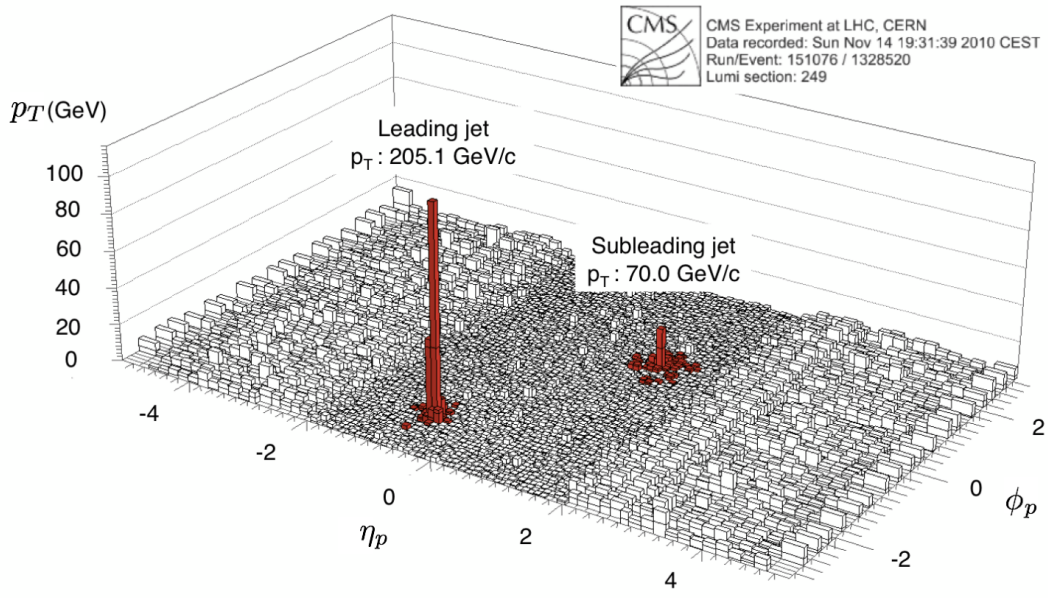

Figure 2.16: Lego plot for a dijet asymmetric event in a Pb-Pb collision at $\sqrt{s_{NN}}$ TeV by the CMS collaboration [15]. The height of towers indicates the total-p_T detected in a calorimeter cell at particular azimuthal angle ϕ_p and pseudorapidity η_p.

observed by the ATLAS Collaboration [14] and the CMS Collaboration [15, 111] [Fig. 2.16] in HIC at LHC. The observed dijets are supposed to originate from pairs of partons produced in early stage hard processes. Without the medium effect, the sum of the dijet momentum is balanced due to the energy momentum-conservation in the hard process. However, a large number of highly asymmetric dijet events are observed in HIC. To quantify the imbalance of the dijet events, the asymmetry ratio is defined by

$$A_J = \frac{p_T^{\text{jet1}} - p_T^{\text{jet2}}}{p_T^{\text{jet1}} + p_T^{\text{jet2}}} \tag{2.33}$$

where p_T^{jet1} and p_T^{jet2} are the transverse momentum of the leading jet and of the subleading jet, respectively. In central Pb-Pb collisions at LHC, a mean shift of A_J to higher values from the ones without medium effect is observed [14, 15, 111] [Fig. 2.17]. The increase of dijet events with large-A_J compared with p-p collisions indicates a substantial amount of energy loss of partons to be sources of jets in the QGP medium at LHC. In a dijet event, one parton going inside of the QGP medium is strongly quenched because of its long path length through the high-temperature region of the medium and the other one going toward the outside does not lose so much energy. As a consequence, the strongly quenched parton is detected as a subleading jet and the other

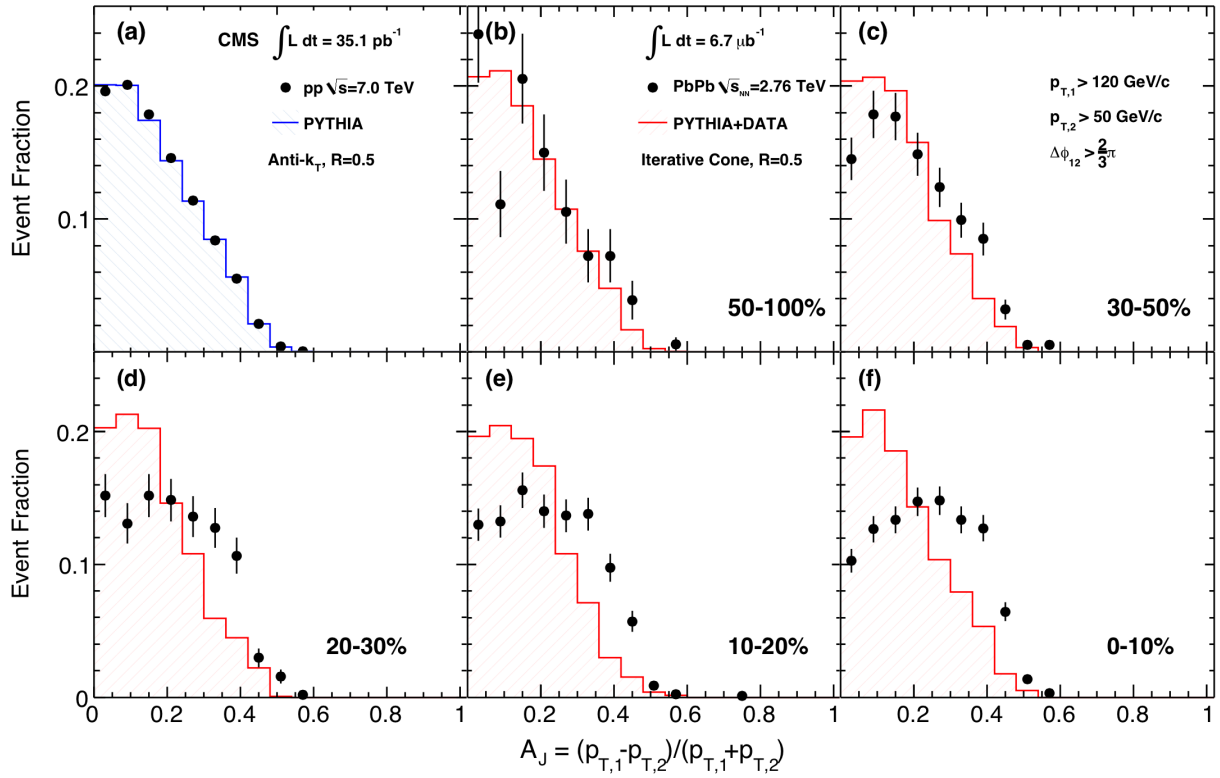

Figure 2.17: Event fraction as a function of the dijet asymmetry ratio A_J for leading jets with $p_T^{\text{jet1}} > 120$ GeV/c, subleading jets with $p_T^{\text{jet2}} > 50$ GeV/c and the azimuthal angles between dijet $|\phi_p^{\text{jet1}} - \phi_p^{\text{jet2}}| > (2/3)\pi$ for p-p collisions at $\sqrt{s_{NN}} = 7$ TeV and for Pb-Pb collisions at $\sqrt{s_{NN}} = 2.76$ TeV in 50-100% (b), 30-50% (c), 20-30% (d), 10-20% (e) and 0-10% (f) centrality bins by the CMS collaboration [15]. The histograms show the results form simulations using event generator PYTHIA without the medium effect on jets.

one is detected as a leading jet. Various theoretical calculations based on parton energy loss have been performed to explain the dijet asymmetry [112, 113, 114, 115, 116, 117, 118, 119].

In dijet asymmetric events, the sum of transverse momenta of jets is not balanced. Since the total momentum of the whole system must be balanced at all times due to the energy-momentum conservation, the lost momenta of jets is diffused somewhere in the system created in HIC. The missing transverse momentum to see the balance of the whole transverse momentum, is defined as

$$\not{p}_T^{||} = \sum_i -p_T^i \cos(\phi_p^i - \phi_p^{\text{jet1}}), \tag{2.34}$$

where $i = 1$ is an index for detected tracks in a dijet event and the sum is taken over all the tracks. The missing transverse momentum $\not{p}_T^{||}$ is the net transverse momentum along the jet axis and p_T of all the tracks is projected onto the subleading jet axis $\phi_p^{\text{jet2}} = \phi_p^{\text{jet2}} + \pi$ in

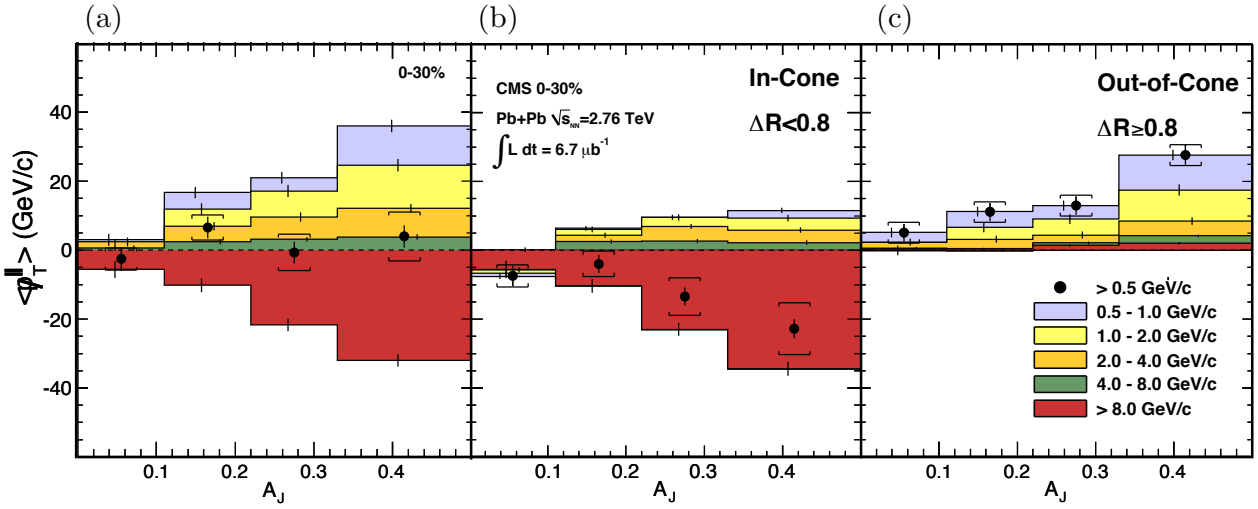

Figure 2.18: $\langle \not{p}_T^{||} \rangle$ as a function of the dijet asymmetry ratio A_J measured for dijet events in Pb-Pb collisions at by the CMS collaboration [15]. The trigger for the leading jet is $p_{T,1} > 120$ GeV/c and the one for the subleading jet is $p_{T,2} > 50$ GeV/c. The angle and pseudorapidity distance between the the leading and subleading jets are $|\phi_p^{\rm jet1} - \phi_p^{\rm jet2}| > (2/3)\pi$ and $|\eta_{\rm s}{}^{\rm jet1} - \eta_{\rm s}{}^{\rm jet2}| > 1.6$, respectively. The tracks with $|\eta_p| < 2.4$ and $p_T > 0.5$ GeVc are used in the result Figure (a) shows the result for the whole region. Figure (b) is the result for inside the leading and subleading jet cones ($\Delta R < 0.8$) and figure (c) is one for outside both of the leading and subleading jet cones ($\Delta R \geq 0.8$). The solid black circles show the total $\langle \not{p}_T^{||} \rangle$ and each band represents the contribution in six transverse-momentum ranges: 0-0.5, 0.5-1, 1-2, 2-4, 4-8 GeV/c, and $p_T > 8$ GeV/c.

the azimuthal direction in Eq. (2.34). $\not{p}_T^{||}$ is measured for dijet events in Pb-Pb collisions at the LHC by the CMS Collaboration [15] [Fig. 2.17]. The event-averaged missing transverse momentum, $\langle \not{p}_T^{||} \rangle$, turned out to vanish within uncertainties even in highly-asymmetric dijet events. Figure 2.18 (a) shows that high-p_T particles which mainly come from the leading jet negatively contributes to $\langle \not{p}_T^{||} \rangle$ and this negative contribution is balanced by lower-p_T particles with $0.5 < p_T < 8$ GeV/c in the direction of the subleading jet. Let us consider two cones in the momentum space around the leading jet axis and the subleading jet axsis with the size

$$\Delta R = \sqrt{(\Delta\phi_p)^2 + (\Delta\eta_{\rm s})^2} = 0.8, \tag{2.35}$$

where $\Delta\phi_p$ and $\Delta\eta_{\rm s}$ are the azimuthal angle and pseudorapidity distance from the leading or subleading jet axis in the momentum space, respectively [Fig. 2.19]. The contribution of the particles inside ($\Delta R < 0.8$) and outside ($\Delta R \geq 0.8$) the cones are shown in Fig. 2.18 (b) and (c), respectively. The contribution to $\not{p}_T^{||}$ from the in-cone region is negative and dominated by high-p_T particles. From this, we can see the imbalance between the jet. This imbalance is compensated by the contribution from the out-of-cone region dominated by very

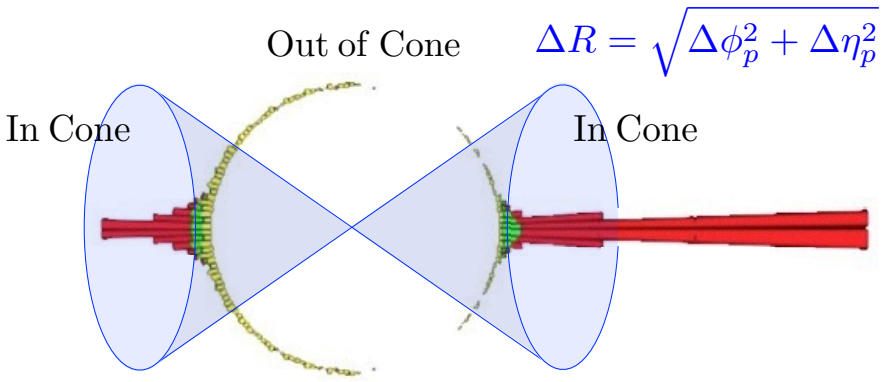

Figure 2.19: Schematic illustration of regions in momentum space divided by two cones around the leading and subleading jet axes with conesize $\Delta R = \sqrt{\Delta\phi_p^2 + \Delta\eta_p^2} = 0.8$. (Figure adapted from the slides of Ref. [17].)

low-p_T particles with $0.5 < p_T < 2$ GeV/c. Since the low-p_T particles play an important role in momentum balance of dijet asymmetric events, it has been suggested that the energy deposition from the traveling partons wakes the QGP medium and induces collective flow to enhance low momentum particles at large angles from the axis of the quenched jet.

2.5 Medium Response to Jet Quenching

The energetic partons originating from initial hard processes do not take part in the hydrodynamical evolution of the QGP medium but traverse the medium. While traversing the medium, the energetic partons deposit their energies and momenta due to the jet quenching. On the side of the QGP fluid, jets can be be considered as supersonic moving sources of energy and momentum.

A source in a fluid induces sound waves. When the source moving faster than the sound velocity of the fluid, a shock wave front appears as an interference of the sound waves [Fig. 2.20]. The shock front, so-called Mach cone, forms a conical surface propagating at a specific angle from the direction of the source. The specific angle is called Mach angle and its value is given by

$$\theta_M = \arcsin\frac{c_s}{v}, \quad v > c_s, \tag{2.36}$$

where c_s is the sound velocity of the fluid and v is the velocity of the source.

In the QGP fluid, Mach cones are supposed to be induced by the energy-momentum deposition from jets. [19, 20]. The Mach cone has been analyzed in various theoretical studies such as hydrodynamics with [20, 21, 22, 23, 24, 25] or without [26, 27, 28, 29, 30, 31, 32] linearlization, AdS/CFT correspondence [33, 34, 35], and a parton-transport model [36, 37].

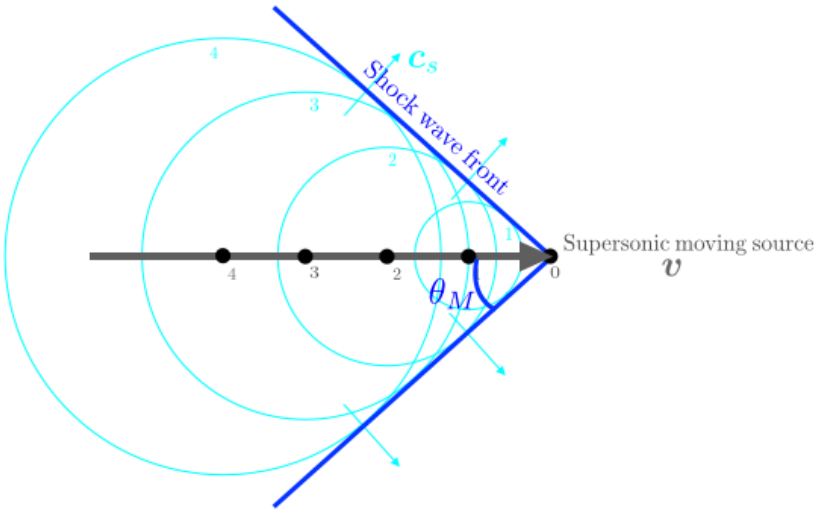

Figure 2.20: Schematic illustration of a Mach cone induced by a supersonic moving source.

Fig. 2.21 shows an example of a result from ideal hydrodynamical calculation [28]. A jet induces flows at angles with the jet due to a Mach cone, as well as a fast flow following the jet. As a result of these flows, low momentum particles from the medium are preferentially emitted at large angles from the jet axis. Furthermore, a vortex ring around the passage of the jet arises inside the Mach cone and follows the jet.

The structure of the Mach cone depends mainly on the sound velocity of the medium as seen in Eq. (2.36). The shape of the Mach cone is also modified by the shear viscosity of the fluid. The shear viscosity transports the fast flow following the jets perpendicular to jet. As a result, Mach cone structure smears out with increasing shear viscosity of the QGP [22, 25, 37]. Thus, collective flow induced by jet energy-momentum deposition carries a lot of information of QGP.

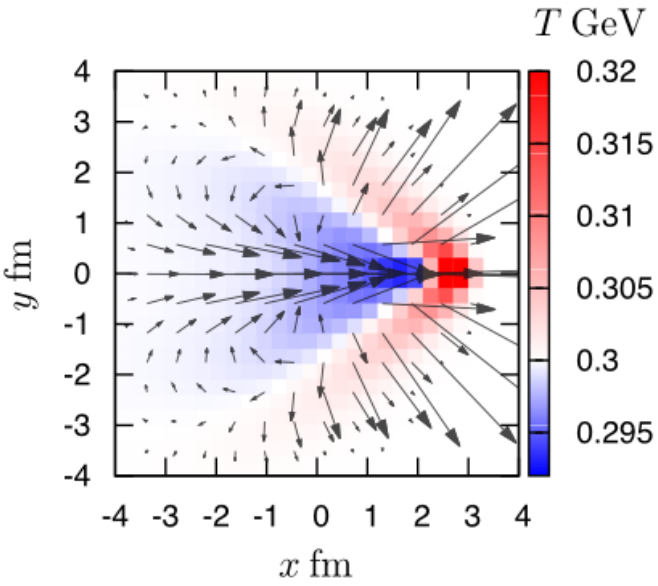

Figure 2.21: Temperature distribution and flow velocity field of the QGP fluid. An energetic parton travels in x-direction while depositing its energy and momentum into the uniform fluid with $T = 0.3$ GeV [28].

Chapter 3

Hydrodynamic Model with Source Terms

We formulate a hydrodynamic model with source terms to study the transport dynamics of momenta deposited from jets to the QGP fluid [29]. Assuming that the jets traverse the expanding QGP fluids, we simulate dijet asymmetric events in HIC. The jets are subject to deposit their energy and momentum into the QGP fluid through the strong interaction. We solve the relativistic hydrodynamic equations with source terms numerically to describe the space-time evolution of the QGP fluid affected by the jet. Then, we study the modification of spectra from the medium by the jet propagation.

3.1 Hydrodynamic Equations with Source Terms

Assuming local thermal equilibrium, we employ the relativistic ideal hydrodynamic equations to describe the spacetime evolution of the QGP medium after the local thermalization $\tau \geq \tau_0$. The conventional hydrodynamic models for HIC require the energy-momentum conservation only in the QGP medium. In the following, we introduce the source term in the hydrodynamic equations which represents the incoming energy and momentum to the fluid. The source term is modeled to conserve the energy and momentum of the whole system consisting of the jets and the QGP fluid. The energy-momentum deposition by the jet induces flows in the expanding QGP. As a result, the spectra of particles originating from the medium can be modified by jet energy loss.

3.1.1 Relativistic Ideal Hydrodynamic Equations

The hydrodynamics is an effective theory of the many-body system in the long-distance and long-time limit. If the mean free path of the constituents is significantly shorter than any typical length scale in the system, the space-time evolution of the system is insensitive to the microscopic details and described by the conservation laws of the macroscopic variables.

The energy-momentum conservation law and continuity equations for conserved charges for relativistic fluid are given by

$$\partial_\mu T^{\mu\nu}(x) = 0, \tag{3.1}$$
$$\partial_\mu N_i^\mu(x) = 0, \tag{3.2}$$

where $T^{\mu\nu}$ is the energy-momentum tensor of the fluid and N_i^μ is the density of the i-th conserved charge. The meaning of each component is,

$$\begin{array}{ll} T^{00} & : \text{energy density,} \\ T^{0i} & : i\text{-th component of energy density flux,} \\ T^{i0} & : \text{density of } i\text{-momentum,} \\ T^{ij} & : i\text{-th component of } j\text{-momentum flux,} \\ N^0 & : \text{charge density,} \\ N^i & : i\text{-th component of charge density current.} \end{array} \tag{3.3}$$

The energy-momentum tensor of the fluid is a symmetric tensor so that the fluid does not have local torques.

In the following, only ideal, namely viscous-free, hydrodynamics will be considered. We assume isotropy of the for ideal fluid in the local rest frame. Then, the energy-momentum tensor in the local rest frame can be written as the following diagonal form:

$$T^{\mu\nu}_{\mathrm{LRF}}(x) = \begin{pmatrix} e(x) & 0 & 0 & 0 \\ 0 & P(x) & 0 & 0 \\ 0 & 0 & P(x) & 0 \\ 0 & 0 & 0 & P(x) \end{pmatrix}, \tag{3.4}$$

where $e(x)$ is the local energy density and $P(x)$ is the local pressure in the local rest frame. One can obtain the energy-momentum tensor in any frame by the Lorentz Transformation of $T^{\mu\nu}_{\mathrm{LRF}}$.

We introduce the four-flow velocity u^μ defined as

$$u^\mu(x) = \gamma(x)(1, \boldsymbol{v}(x)), \tag{3.5}$$

where $\gamma = 1/\sqrt{1 - |\boldsymbol{v}|^2}$ is the Lorentz factor. The four-flow velocity u^μ is normalized as

$$u^\mu(x) u_\mu(x) = 1. \tag{3.6}$$

By using u^μ, the energy-momentum tensor and the conserved current for perfect fluid can be decomposed as

$$T^{\mu\nu} = (e(x) + P(x)) u^\mu(x) u^\nu(x) - P(x)\eta^{\mu\nu} \tag{3.7}$$
$$= e(x) u^\mu(x) u^\nu(x) - P(x)\Delta^{\mu\nu}(x), \tag{3.8}$$
$$N_i^\mu(x) = n_i(x) u^\mu(x), \tag{3.9}$$

where $\eta^{\mu\nu} = \mathrm{diag}(1, -1, -1, -1)$ is the Minkowski metric, and $\Delta^{\mu\nu} = \eta^{\mu\nu} - u^\mu u^\nu$ is the tensor perpendicular to u^μ:

$$u_\mu \Delta^{\mu\nu} = u_\mu(\eta^{\mu\nu} - u^\mu u^\nu) = (1 - u^\mu u_\mu)u^\nu = 0. \tag{3.10}$$

To see more in detail about the ideal hydrodynamic equations, we perform the projection of Eq. (3.1) along the four-flow velocity:

$$0 = u_\nu \partial_\mu T^{\mu\nu} \tag{3.11}$$

$$= u^\mu \partial_\mu e + (e + P)\partial_\mu u^\mu. \tag{3.12}$$

If we assume the local thermal equilibrium, the following thermodynamic relations can be used:

$$de = Tds + \sum_i \mu_i dn_i, \tag{3.13}$$

$$e = Ts - P + \sum_i \mu_i n_i, \tag{3.14}$$

where s, T and μ are the local entropy density, the local temperature and the local chemical potential, respectively. By using Eq. (3.13), Eq. (3.14) and charge conservation $\partial_\mu(n_i u^\mu) = 0$, Eq. (3.12) becomes

$$\partial_\mu \left(s(x)u^\mu(x)\right) = 0. \tag{3.15}$$

Thus, the entropy of the ideal fluid is conserved globally and not produced during the space-time evolution.

Similarly, Eq. (3.1) projected by $\Delta_{\mu\nu}$ is

$$\Delta_{\rho\nu}\partial_\mu T^{\mu\nu} = 0, \tag{3.16}$$

which reduces to

$$(e + P)u^\mu \partial_\mu u_\rho = \Delta_{\rho\nu}\partial^\nu P. \tag{3.17}$$

Since $u^\mu \partial_\mu u_\rho$ represents the acceleration of the flow, the flow is generated along the pressure gradient. Eq. (3.17) is the equation of motion of the relativistic ideal fluid and corresponds to the Euler equation in the non-relativistic hydrodynamics.

3.1.2 Source Terms

We introduce source term in the hydrodynamic equations which represents the incoming energy and momentum from the jet:

$$\partial_\mu T^{\mu\nu}(x) = J^\nu(x), \tag{3.18}$$

where J^ν is the source term where is the four-momentum density deposited from the traversing jet partons.

The detailed form of the source term and the mechanism of jet's energy deposition into the medium are not fully understood. The source term due to the collisional energy loss of an energetic parton in the thermalized QGP medium is studied based on the Boltzmann-Vlasov equation [120] and the hard thermal loop (HTL) perturbation theory [121]. The radiative energy loss makes huge contributions to the energy-momentum deposition through the absorption or collision energy loss of the soft radiated partons [114]. The flow structure induced by jets is enhanced by the contribution of the radiative energy loss [24, 23]. More recently, the energy-momentum deposition of jets has been studied in Refs. [122, 31] by performing Monete Carlo jet quenching simulations based on perturbative QCD. It is also suggested that the flow structure induced by jets can be largely modified by the effect of full (3+1)-dimensional space-time structure of jet shower [121].

Here, assuming that the lost energy and momentum of energetic partons are instantaneously deposited to and thermalized in a QGP-fluid cell, we employ a simple form for massless jets traversing the QGP fluid:

$$J^\mu(x) = \sum_a J_a^\mu(x), \tag{3.19}$$

$$J_a^0(x) = -\frac{dp_a^0}{dt}\delta^{(3)}(\boldsymbol{x} - \boldsymbol{x}_a(t)), \tag{3.20}$$

$$\boldsymbol{J}_a(x) = \frac{\boldsymbol{p}_a}{p_a^0} J_a^0(x), \tag{3.21}$$

where the index a denotes each jet and $p_a^\mu = (p_a^0, \boldsymbol{p_a})$ is the momentum of the jet.

For the energy loss of the jets in the local rest frame of the fluid, we take the collisional energy loss formula [94]

$$-\frac{dp_a^0}{dt} = A \times \frac{8}{3}\pi {\alpha_s}^2 T^2 \left(1 + \frac{1}{6}N_f\right) \log\frac{\sqrt{4Tp_a^0}}{m_D}. \tag{3.22}$$

Here, p_a^0 is the energy of a jet in the local rest frame, $\alpha_s = g^2/(4\pi)$ is the strong fine structure constant, N_f is the number of active flavors and $m_D = \sqrt{1 + N_f/6}\, gT$ is the Debye mass in the QGP medium. The amount of the energy loss obtained from the collisional energy loss (3.22) is too small to reproduce the highly asymmetric dijet event observed in HIC. To determine the energy deposition into the medium in a more quantitative way, the contribution of the other energy loss mechanisms must be considered. It should be noted that the purpose of the present study is to investigate the hydrodynamic response of the QGP to the jets rather than the energy loss mechanism itself. So, for simplicity, we introduce A which is a phenomenological parameter which allows us to controls the strength of the energy loss. The momentum dependence is included only logarithmically in Eq. (3.22) and the parameter A can be interpreted as a value corresponding to a typical number of radiated partons in a jet.

We solve the hydrodynamic equations numerically with the source terms (3.18) in the $(3+1)$-dimensional Milne coordinates (τ, x, y, η_s) without linearization. Here, $\tau = \sqrt{t^2 + z^2}$ is the proper time and $\eta_s = (1/2)\ln\left[(t+z)/(t-z)\right]$ is the spacetime rapidity. The source terms in the Milne coordinate are calculated by performing the Lorentz transformation on the ones (3.19) in the local rest frame obtained from Eqs. (3.20), (3.21) and (3.22). See Appendix A.1 for the Milne coordinate and Appendix B for the numerical techniques for the hydrodynamic calculations. In this framework, we can handle an expanding background QGP fluid created in HIC together with its response to the jet propagation.

In the hydrodynamic calculations, we developed a new and robust scheme for the Milne coordinates [123] are employed to keep the energy-momentum conservation (see Appendix B.5 for details). This plays a crucial role in the calculations because the deposited energy and momentum from a jet are very small relative to the total energy and momentum of the medium.

For the jet energy loss, we set $N_f = 3$ (u, d, s), $\alpha_s = 0.3$, and $A = 15$ in Eq. (3.22) to obtain the typical amount of the energy loss at LHC [114, 122]. We assume that the jets interact only with QGP with $T > 0.175$ GeV. Enhancement of the jet energy loss near the critical temperature [124, 125, 126] and jet energy loss in the hadronic medium are not included in the calculations.

3.2 Initial Condition and Equation of State for QGP Fluid

To solve the hydrodynamic equations, the initial condition and the equation of state are always necessary. In the hydrodynamic model for HIC, the initial condition is set at the time when the thermalization of the medium is achieved. There are various models for the initial condition of the QGP fluid in HIC, *e.g.* the Glauber model [73], the KLN model [127] based on the color glass condensate (CGC) picture [128, 129], the IP-Glasma model [61, 62] including the effect of the space-time evolution of initial gluonic matter, etc. Especially the anisotropy in the azimuthal spectra in the final state is expected to depend strongly on the initial profile of the QGP fluid. In this study, we employ the Glauber model. As for the equation of state which determines the relation among the thermodynamic variables, we take the ideal gas of massless quarks and gluons.

3.2.1 Initial Profile of QGP Fluid

We apply the hydrodynamic model to the space-time evolution of the medium in the Pb-Pb collisions after the themalization $\tau \geq \tau_0 = 0.6$ fm/c. Here, we employ the modified BGK initial

condition to set the initial entropy density profile of the medium [83] (see section 2.3):

$$
\begin{aligned}
s\left(\tau_0,\, \eta_{\rm s},\, \boldsymbol{r}_\perp\right) &= \frac{C}{\tau_0}\,\theta(Y_{\rm beam}-|\eta_{\rm s}|)\,H(\eta_s) \\
&\quad\times\left[\frac{(1-\alpha)}{2}\left(\frac{Y_{\rm beam}-\eta_{\rm s}}{Y_{\rm beam}}n^A_{\rm part}(\boldsymbol{r}_\perp)+\frac{Y_{\rm beam}+\eta_{\rm s}}{Y_{\rm beam}}n^B_{\rm part}(\boldsymbol{r}_\perp)\right)+\alpha n_{\rm coll}\left(\boldsymbol{r}_\perp\right)\right], \qquad (3.23)\\
H\left(\eta_s\right) &= \exp\left[-\frac{\left(|\eta_s|-\eta_{\rm flat}/2\right)^2}{2\sigma_\eta^2}\theta\left(|\eta_s|-\frac{\eta_{\rm flat}}{2}\right)\right], \qquad (3.24)
\end{aligned}
$$

where $Y_{\rm beam} = \operatorname{arccosh}\left(\sqrt{s_{NN}}/m_N\right)$ is the beam rapidity of incoming nuclei, $m_N = 0.939$ GeV is the nucleon mass, $n^A_{\rm part}$ and $n^B_{\rm part}$ are participant number densities in each nucleus, $n^A_{\rm coll}$ is collisions number density. C, α, $\eta_{\rm flat}$ and σ_η are phenomenological parameters. For Pb-Pb collision at LHC, we set $\sqrt{s_{NN}} = 2.76$ TeV, $C = 4.14$, $\alpha = 0.08$, $\eta_{\rm flat} = 1.9$ and $\sigma_\eta = 3.2$ [130]. For the initial condition of the flow velocity, we assume that there is no radial and rotational flow in the transverse direction. Also no additional flow to the Bjorken flow [75] is in the longitudinal direction. In this case, the initial condition for the flow-velocity in the Milne coordinate can be written as

$$
u^\alpha\left(\tau=\tau_0,\, x,\, y,\, \eta_{\rm s}\right) = 0. \qquad (3.25)
$$

This initial condition for the flow is commonly used in the hydrodynamic models for HIC. The flow velocity of the expanding QGP is assumed to be driven only by the initial profile of the medium at $\tau = \tau_0$.

3.2.2 Equation of State

The ideal hydrodynamic equations (3.1) and (3.2) with n conserved charges consist of $(4+n)$ equations and have $(5+n)$ independent valuables, *i.e.* e, P, u^μ ($\mu = 0,\ 1\ 2\ 3$) and n_i ($i = 1, \cdots, n$). Thus, the system of the equations is not closed and another equation, the equation of state, is required. Whereas the ideal hydrodynamic equations describe only the macroscopic conservation law, the equation of state is determined by the microscopic dynamics.

In this study, we employ the equation of state for ideal gas of massless quarks and gluons. We set the number of flavors in the QGP, $N_f = 3$ (u, d, s) to coincide with the one chosen in the energy loss. The degrees of freedom for quarks and gluons in the QGP are

$$
\begin{aligned}
d_{\rm quark} &= 3\,(\text{flavors})\,\times 3\,(\text{colors})\,\times 2\,(\text{spins})\,\times 2\,(\text{particle-antiparticle}) = 36, \qquad (3.26)\\
d_{\rm gluon} &= 8\,(\text{colors})\,\times 2\,(\text{spins}) = 16. \qquad (3.27)
\end{aligned}
$$

Here, we consider the baryon-free QGP fluid with no conserved charges. Under these assump-

tions, the relations between thermodynamic variables of the QGP medium are

$$P = d_{\mathrm{QGP}} \frac{\pi^2}{90} T^4, \tag{3.28}$$

$$s = d_{\mathrm{QGP}} \frac{2\pi^2}{45} T^3, \tag{3.29}$$

$$e = d_{\mathrm{QGP}} \frac{\pi^2}{30} T^4, \tag{3.30}$$

where $d_{\mathrm{QGP}} = d_{\mathrm{quark}} \times \frac{7}{8} + d_{\mathrm{gluon}}$ is the effective degrees of freedom for the QGP. Then, from these relations, the equation of state is obtained as follows:

$$P(e) = \frac{1}{3} e. \tag{3.31}$$

Then, the sound velocity of the medium is

$$c_{\mathrm{s}} = \left(\left. \frac{\partial P}{\partial e} \right|_{s/n} \right)^{\frac{1}{2}} = \sqrt{\frac{1}{3}}. \tag{3.32}$$

Figure 3.1 shows the initial energy density profile of the QGP medium for a central Pb-Pb collision at LHC obtained from the modified BGK model (3.23) and the relations between thermodynamic variables (3.29) and (3.30). The modified BGK initial condition for a central collision of the same nuclei is reduced to the one (2.15).

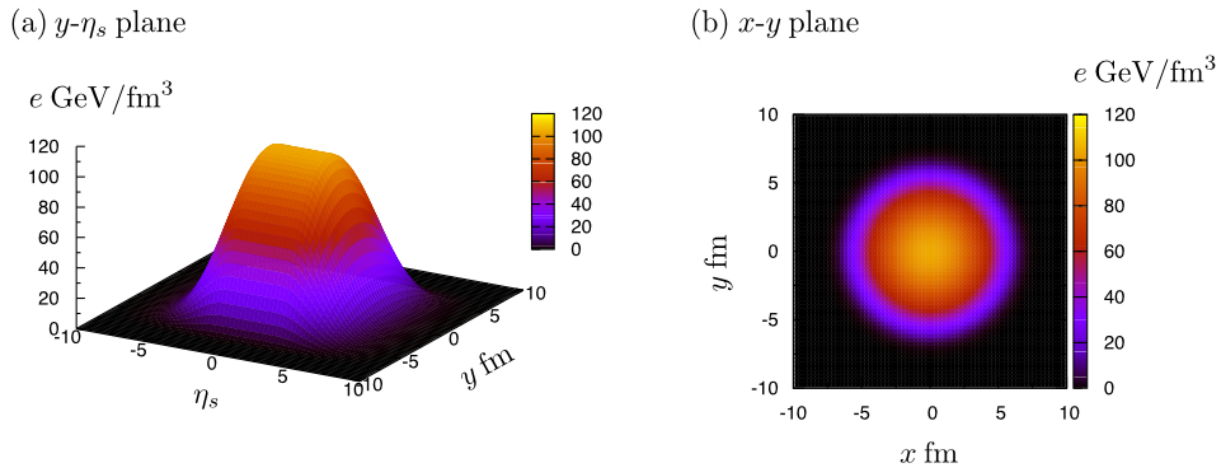

Figure 3.1: Initial energy density profile of the QGP medium for a central Pb-Pb collision at LHC in the y-η_{s} plane at $x = 0$ (a) and in the x-y plane at $\eta_{\mathrm{s}} = 0$ (b) obtained from the modified BGK model.

3.3 Kinetic Freezeout

To obtain particle spectra at the end of the hydrodynamic evolution, it is necessary to convert from the hydrodynamic variables to phase space distribution. In hydrodynamic models, it is assumed that the kinetic freezeout is accomplished instantaneously in the fluid elements while passing the freezeout hypersurface. The spectra can be given by integrating the local thermal equilibrium distribution at the freezeout hypersurface boosted by the flow velocity:

$$p^0 \frac{dN_i}{d^3p} = \frac{g_i}{(2\pi)^3} \int_\Sigma \frac{p^\mu d\sigma_\mu(x)}{\exp\left[p^\mu u_\mu(x)/T(x)\right] \pm 1}, \tag{3.33}$$

where i is an index for the species of the particle, Σ is the freezeout hypersurface, g_i is the degeneracy and $\pm$ corresponds to Fermi or Bose distribution for particle species i and $d\sigma$ is the hypersurface element. Eq. (3.33) is called the Cooper-Frye formula [45] and is used to obtain the momentum distribution of particle species i from hydrodynamic outputs. The kinetic freezeout is supposed to occur when the temperature falls below the freezeout temperature T_f, so the freezeout hypersurface Σ is determined by T_f. The contributions of the fluid elements passing the hypersurface from the region with $T > T_f$ to the region with $T \leq T_f$ are added to the spectra. On the other hand, when the fluid elements pass the freezeout hypersurface from the region with $T \leq T_f$ to the region with $T > T_f$, their contributions are subtracted from the spectra. By following this procedure at every moment, the surface integral (3.33) is carried out.

We use the Cooper-Frye formula to obtain the distribution of the transverse momentum and the missing transverse momentum $\not{p}_T^{||} = \sum -p_T \cos(\phi_p - \phi_1)$:

$$\frac{d}{d\phi_p dy}\langle p_T \rangle_{\text{fluid}} = \sum_i \int dp_T\, p_T\, \frac{dN_i}{dp_T d\phi_p dy}, \tag{3.34}$$

$$\langle \not{p}_T^{||} \rangle_{\text{fluid}} = -\sum_i \int dp_T d\phi_p\, p_T \cos(\phi_p - \phi_1)\, \frac{dN_i}{dp_T d\phi_p}, \tag{3.35}$$

$$\frac{dN_i}{p_T dp_T d\phi_p dy} = p^0 \frac{dN_i}{d^3p}. \tag{3.36}$$

Here, ϕ_p is the azimuthal angle in momentum space, y is the rapidity and $m_T = \sqrt{m_i^2 + p_T^2}$ is the transverse momentum of the particle species i. Adding the transverse momentum of jets traversing the medium in the final state to $\langle \not{p}_T^{||} \rangle_{\text{fluid}}$, we obtain $\langle \not{p}_T^{||} \rangle$ to be compared with the data.

In this thesis, we set the freezeout temperature, $T_f = 0.16$ GeV, to reproduce the magnitude of the measured v_2. The particles yielded after the kinetic freezeout are massless quarks and gluons because we employed the equation of state for ideal gas of quarks and gluons which does not contain the hadronization process. Here, the degeneracy d_i in Eq. (3.33) are set to the degrees of feedom in Eqs. (3.26) and (3.27): $d_{\text{quark}} = 36$ and $d_{\text{gluon}} = 15$. In recent hydrodynamic model calculations, the equation of state from lattice QCD calculations is used for a more quantitative analysis. However, the lattice equation of state requires enormous

calculation involving all the hadron resonances at the kinetic freezeout to see the subtle interplay of momentum balance studied in the following. In this thesis, we employ the ideal gas equation of state for simplicity and keep the strict momentum conservation at the freezeout as well as that in hydrodynamic evolution. In the the lattice equation of state, the degrees of freedom decrease while expanding and cooling down. This makes the cooling of the medium slower than in the ideal gas one. For a more quantitative analysis, the employment of the lattice equation of state and the freeze out calculation via Cooper-Frye formula with all the hadron resonances would be needed and we postpone them as future studies.

Chapter 4

Collective Flow Induced by Dijet Traveling through the Center of the Medium

In this chapter, to study the typical flow structures in dijet events and the resultant spectra from them, we perform simulations in the case of the dijet traveling through the center of the expanding medium. The jet-induced flows is expected to develop largely because they are caused in the high-temperature region of the QGP fluid. In our simulations, we use the model for HIC at LHC explained in the previous chapter. By solving the hydrodynamic equations with the source terms numerically, we study the space-time evolution of the flow induced by the jets in the expanding QGP. Then, we calculate the spectra from the medium via the Cooper-Frye formula. Then, we show that the low-p_T particles are enhanced in dijet events as a result of the energy-momentum transport by flows in the QGP. This firmly relates the experimental results by the CMS Collaboration [15] with the hydrodynamic response to the jets in the medium. The work presented in this chapter is original and done in collaboration with Tetsufumi Hirano (Sophia Univ.). The auther builds the model, perform the simulations and analyze the data from them based on discussions with the collaborator. The program codes for the simulations are also developed by the auther himself.

4.1 Dijet Traveling through the Center of the Medium

We consider the dijet events in the central Pb-Pb collisions. The origin ($x = 0$, $y = 0$, $\eta_{\rm s} = 0$) is set at the center of the QGP fluid. A pair of back-to-back massless jets is supposed to be created at ($\tau = 0$, $x = 0$, $y = y_0 \geq 0$, $\eta_{\rm s} = 0$) with the common energy, $p_a^0(\tau = 0) = 200$ GeV. Then the jets travel in the opposite direction along the y axis at the speed of light [Fig. 4.1]. Until $\tau = \tau_0 = 0.6$ fm/c, these jets travel without interactions. At $\tau = \tau_0 = 0.6$ fm/c, they start to interact with the QGP fluid and deposite their energy and momentum into the fluid. At the same time the hydrodynamic evolution of the medium starts.

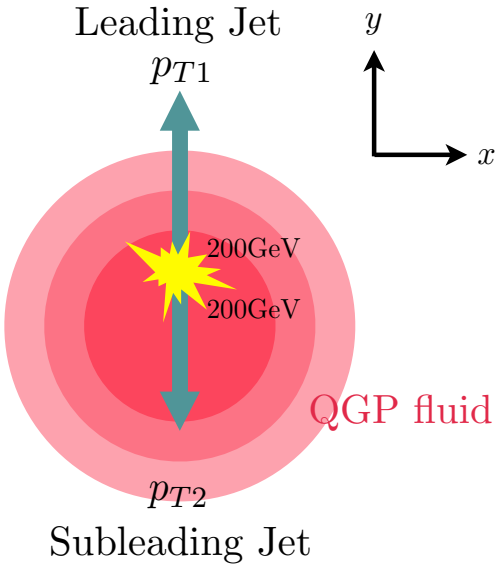

Figure 4.1: Geometry for the simulation of the dijet asymmetric event in section 4

In the events with a dijet created at an off central position, imbalance between the dijet in the final state is generated due to the path length difference in the medium: One jet going toward the outside of QGP is observed as a leading jet with transverse momentum $p_T^{\rm jet1}$ and the other one going inside is observed as a subleading jet with transverse momentum $p_T^{\rm jet2}$ $\left(< p_T^{\rm jet1}\right)$. We control the jet asymmetric parameter $A_J = \left(p_T^{\rm jet1} - p_T^{\rm jet2}\right) / \left(p_T^{\rm jet1} + p_T^{\rm jet2}\right)$ by changing the initial position of the pair creation: When the position of the pair creation is off central, namely, $y_0 > 0$, the amount of energy loss is different between the two jets.

4.2 Numerical Results

4.2.1 Space-time evolution of the medium

Figs. 4.2 and 4.3 show the temperature distribution of the QGP fluid in the transverse plane at $\eta_{\rm s} = 0$ and in the reaction plane at $x = 0$, respectively. The pair of jet is created at $y_0 = 0$, 3.0 fm and 6.0 fm. We can see relatively higher temperature regions which have oval or V-shaped structures in each case. These are the remnants of Mach cones which are generated by the energy-momentum deposition from jets and then distorted by the expansion of the QGP.

Fig. 4.2 (a) shows the space-time evolution of the medium in the transverse plane for the dijet symmetric event (y_0=0). A_J for this event is to be vanished. In this case, both Mach cones have the same structure and are pushed by the radial expansion of the medium only from the inside of the cones. As a result, Mach cones become oval shape and their Mach angle θ_M becomes effectively larger around the jet.

Figs. 4.2 (b) and (c) show the space-time evolutions of the medium in the transverse plane

for the dijet asymmetric events ($y_0 = 3.0$, 6.0 fm). The dijet asymmetry ratios for these event are to be non vanishing ($A_J > 0$). In these cases, the two Mach cones induced by the leading jet and the subleading jet have significantly different structures. The subleading jet travels through higher temperature region and loses more energy and momentum than the leading jet. As a consequence, the structure of the Mach cones induced by the subleading jets grows larger. These larger Mach cones in the asymmetric events are pushed by the radial expansion of the medium also from the outside of the cones. and their Mach angles are effectively sharper than the one in the symmetric event. Since the Mach cone in the case of $y = 6.0\,\mathrm{fm}$ is pushed for a longer time, it is slightly sharper than the one in the case of $y = 3.0\,\mathrm{fm}$. In dijet event with larger value of A_J, flows are induced in the larger angle direction from the jet axis. On the other hand, the Mach cones induced by the leading jets does not develop so much largely. Since they are pushed by the radial expansion at the edge of the medium from the inside even after the end of the energy-momentum deposition, the tip of the Mach cones become flat and have flow velocity almost in the direction of the jet axis.

Mach cones also develops in the longitudinal direction in the reaction plane as shown in Fig. 4.3. However, the longitudinal expansion of the QGP medium do not stretch the Mach cones so much apparently in η_s-direction. This is simply understood because the coordinate itself expands: the Mach cones are largely spread out in the z-direction in the Cartesian coordinate.

The space-time evolution of the medium as a fluid is finished when the maximum temperature of the medium gets lower than the freezeout temperature $T_f = 0.16$ GeV. The proper times for $y_0 = 0$, 3, 6 fm corresponds to $\tau = 7.5$, 8.1, 9.0 fm/c, respectively. From this, we can see that as the balance between the dijet becomes more asymmetric as the lifetime of the fluid gets longer. This is because the medium is reheated by the energy deposition.

Here, the equation of state of massless ideal gas is employed to respect the simple but strict energy-momentum conservation at the later kinetic freezeout. However, we find that the basic feature of the flow structure induced by jets in the expanding QGP fluid does not change when we employ the equation of state from lattice QCD calculations [131]. In the realistic lattice equation of state, the tip of the Mach cone is sharper than in the equation of state of massless ideal gas. This is because the Mach angle $\theta_M = \arcsin c_s$ depends on the sound velocity of the medium c_s and the lattice equation of state has smaller c_s than the ideal gas one.

4.2.2 Spectra from the medium

Missing transverse momentum

Figure 4.4 shows the missing transverse momentum $\not{p}_T^{||} = \sum_i -p_T^i \cos(\phi_p^i - \phi_p^{\mathrm{jet1}})$ as a function of the dijet asymmetry ratio A_J. Dijet events with large value of A_J, such as $A_J \geq 0.4$, is reproduced by set the phenomenologocal parameter $A = 15$ in eq. (3.22) to gain a large amount of jet energy loss. Let us consider two cones around the leading axis and subleading axis with the size $\Delta R = \sqrt{\Delta\phi_p^2 + \Delta{\eta_s}^2} = 0.8$ [Fig. 2.19], we separate the momentum space

into two regions, the in-cone region and the out-of-cone region. $\Delta\phi_p$ and $\Delta\eta_s$ are the azimuthal angle and pseudorapidity distance from the direction of leading or subleading jet axis. Fig. 4.4 (a), (b) and (c) show the contribution of all the particles, the particles from the in-cone region ($\Delta R < 0.8$) and from the out-of-cone region ($\Delta R > 0.8$). Here, the transverse momenta of the jets in the final state are added to the contribution of particles with $p_T > 8\,\mathrm{GeV}/c$ from the in-cone region.

We can see the followings from Fig. 4.4:

- The total transverse momentum of the whole system is balanced well for any values of A_J.

This guarantees that the energy and momentum are conserved in the calculations both of the hydrodynamic equations with source terms and of the kinetic freezeout. The asymmetry between the jets are balanced by the contribution from low-p_T particles with $p_T < 2$ GeV/c in the subleading direction. These low-p_T particles originate from the deposited energies of jets in the QGP fluid.

- The total transverse momentum inside the cones is not balanced for the dijet asymmetric events. The contribution to $\not{p}_T^{||}$ is negative, *i.e.*, it is on the leading-jet side, and dominated by high-p_T particles with $p_T > 2$ GeV/c.

The high-p_T particles with $p_T > 8$ GeV/c mainly come from the contribution of jet particles. On the other hand, particles with 2-8 GeV/c originate from the medium with very large flow velocity induced by jets in the direction of the jets.

- The low-p_T particles with $p_T < 2$ GeV/c are also emitted to the out-of-cone region. Their contribution to $\not{p}_T^{||}$ is positive and compensates the a large fraction of imbalance inside the cones.

This tendency is in good agreement with the data from the CMS Collaboration [15]. In the calculations, collective flows are induced by jets and they carry the deposited energies and momenta, with the result that the low-p_T particles are enhanced at the large angles from jets. This fact provides an intimate link between the hydrodynamic response to jet quenching and the phenomena experimentally observed in HIC.

Compared to the data from CMS, a larger fraction of the low-p_T particles are still emitted to the in-cone region in the presented result. In the lattice equation of state, the low-p_T particles is expected to decrease in the in-cone region and to increase in the out-of-cone region by the sharper Mach cone carrying the deposited energies and momenta at larger angles. This means that the effect of momentum transport away from the jet axis is underestimated here.

Transverse momentum distribution

Fig. 4.5 shows the transverse momentum distribution $\frac{dp_T}{d\phi_p d\eta_p}$ in ϕ_p-η_p plane for the dijet asymmetric events with $y_0 = 3.0\,\mathrm{fm}$. Here, only the contribution of the particles originating from the QGP medium are included in $\frac{dp_T}{d\phi_p d\eta_p}$ and the transverse momenta of jets are not included.

The followings can be seen in Fig. 4.5:

- Total $\frac{dp_T}{d\phi_p d\eta_p}$ has a narrow peak in the leading jet direction *i.e.*, $(\phi_p,\, \eta_\mathrm{s}) = (\pi/2,\, 0)$, and a broad peaks in the subleading jet direction *i.e.*, $(\phi_p,\, \eta_\mathrm{s}) = (3\pi/2,\, 0)$.

Intutively, Mach cones are expected to produce ring-shaped spectra around the jet axes by analogy to a ring image of the Cherenkov radiation. However, no such structure can be seen. Three causes can be considered for the absence of such ring-shaped spectra. First, not only Mach cones but strong collective flow following the jets are induced by the momentum deposition. These strong following flow cause prominent peaks in the spectra in the direction of jets. Second, the local thermal equilibrium distribution boosted by the flow velocity is used to calculate the spectra in the Cooper-Frye formula (3.33). The resulting spectra are smeared out around the direction of the flow velocity. Third, Mach cones are distorted by the expansion of the medium. Actually, the characteristic pattern reflecting the Mach cone structure does not exist in the observation by the CMS Collaboration [Fig. 1.1].

- In the region of $p_T > 8\,\mathrm{GeV}/c$, only a narrow peak in the leading jet direction can be seen. In the regions of $4\,\mathrm{GeV}/c < p_T < 8\,\mathrm{GeV}/c$ and $2\,\mathrm{GeV}/c < p_T < 4\,\mathrm{GeV}/c$, the peak in the leading jet direction is much larger than the one in the subleading jet direction.

Since we employ the isothermal freezeout, the structure of the transverse momentum distribution is determined only by the flow velocity at the freezeout. The narrow peaks in the leading jet direction in the high-p_T regions are consequences of very fast flows induced by the leading jet. The Mach cone induced by the leading jet does not grow large before the kinetic freezeout because it caused in the rather low-temperature region.

- In the regions of $1\,\mathrm{GeV}/c < p_T < 2\,\mathrm{GeV}/c$ and $0.5\,\mathrm{GeV}/c < p_T < 1\,\mathrm{GeV}/c$, the peak in the subleading jet direction is larger and much broader than the one in the leading jet direction.

The Mach cone induced by the subleading jet grows largely in the medium because it propagates in the high-temperature region of the QGP fluid. As a result, the deposited energy and momenta are widely diffused and low-p_T particles have the broad peak in subleasing direction.

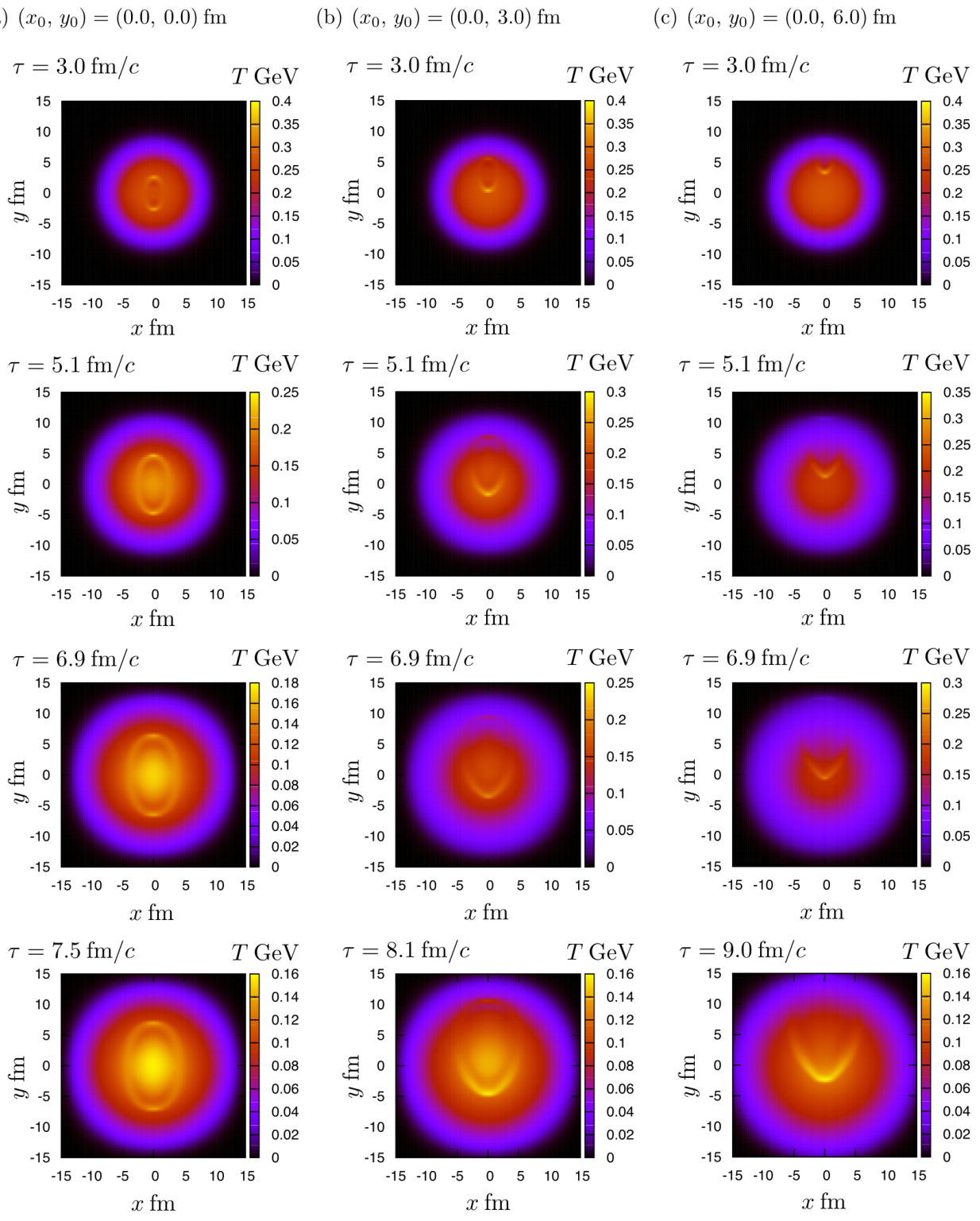

Figure 4.2: Temperature distribution of the expanding QGP fluid in transverse plane at midrapidity $\eta_s = 0$. A pair of jets is produced at $(\tau = 0, x = 0, y = y_0 = 0, \eta_s)$ (a), $(\tau = 0, x = 0, y = y_0 = 3\,\text{fm}, \eta_s)$ (b) and $(\tau = 0, x = 0, y = y_0 = 6\,\text{fm}, \eta_s)$ (c). Then, the jets travels in the opposite direction along the y-axis at the speed of light. The snapshots are taken at $\tau = 3.0\,\text{fm}/c$, $\tau = 5.1\,\text{fm}/c$, $\tau = 6.9\,\text{fm}/c$ and the proper time when the maximum temperature of the medium gets lower than the freezeout temperature $T_f = 0.16$ GeV.

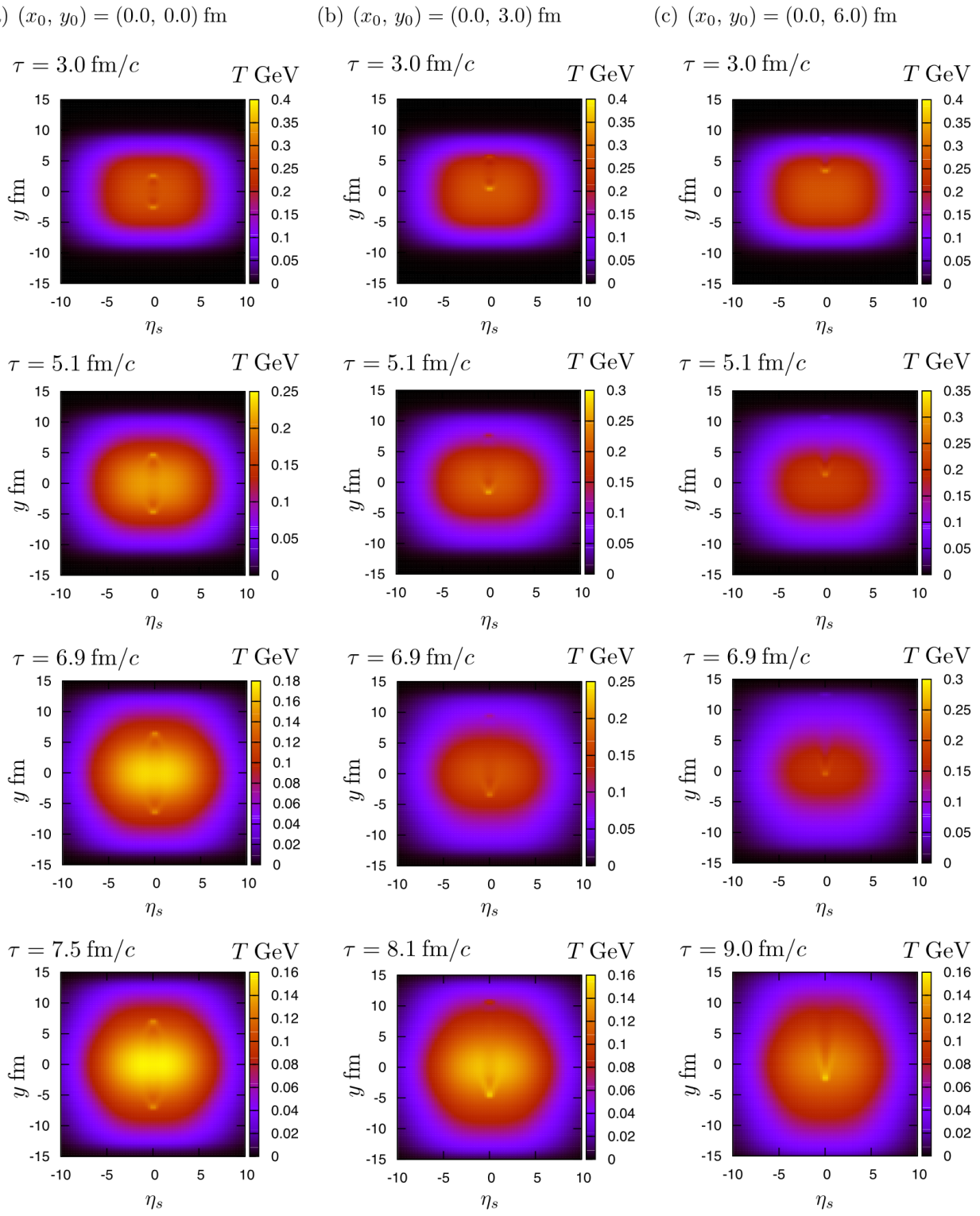

Figure 4.3: Temperature distribution of the expanding QGP fluid in reaction plane at $x = 0$. A pair of jets is produced at ($\tau = 0$, $x = 0$, $y = y_0 = 0$, η_s) (a), ($\tau = 0$, $x = 0$, $y = y_0 = 3\,\mathrm{fm}$, η_s) (b) and ($\tau = 0$, $x = 0$, $y = y_0 = 6\,\mathrm{fm}$, η_s) (c). Then, the jets travels in the opposite direction along the y-axis at the speed of light. The snapshots are taken at $\tau = 3.0\,\mathrm{fm}/c$, $\tau = 5.1\,\mathrm{fm}/c$, $\tau = 6.9\,\mathrm{fm}/c$ and the proper time when the maximum temperature of the medium gets lower than the freezeout temperature $T_f = 0.16$ GeV.

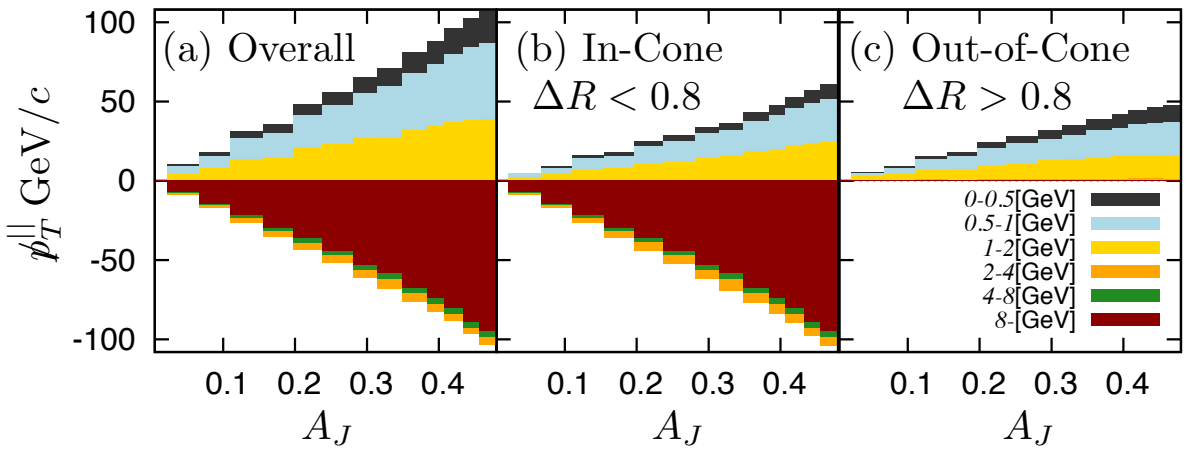

Figure 4.4: $p_T^{||}$ as a function of the dijet asymmetry ratio A_J. Figure (a), (b) and (c) show the contribution from the over all region, inside the leading jet cone or subleading jet cone ($\Delta R < 0.8$), and outside both of the leading and subleading jet cones ($\Delta R > 0.8$) in the momentum space. Each colored histogram represents the contribution to $p_T^{||}$ from six transverse-momentum ranges: 0-0.5, 0.5-1, 1-2, 2-4, 4-8 GeV/c, and $p_T > 8$ GeV/c.

(a) Total

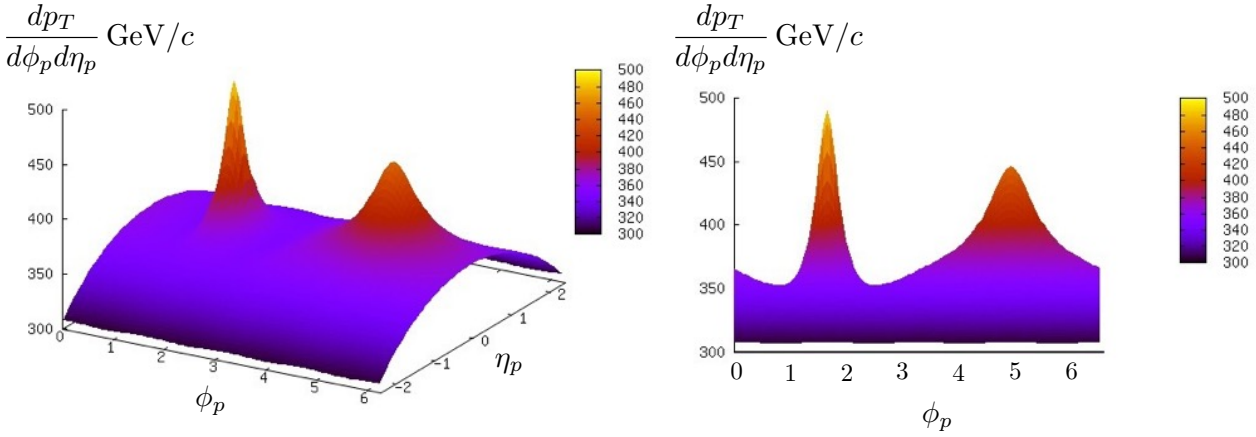

(b) $p_T > 8\,\mathrm{GeV}/c$

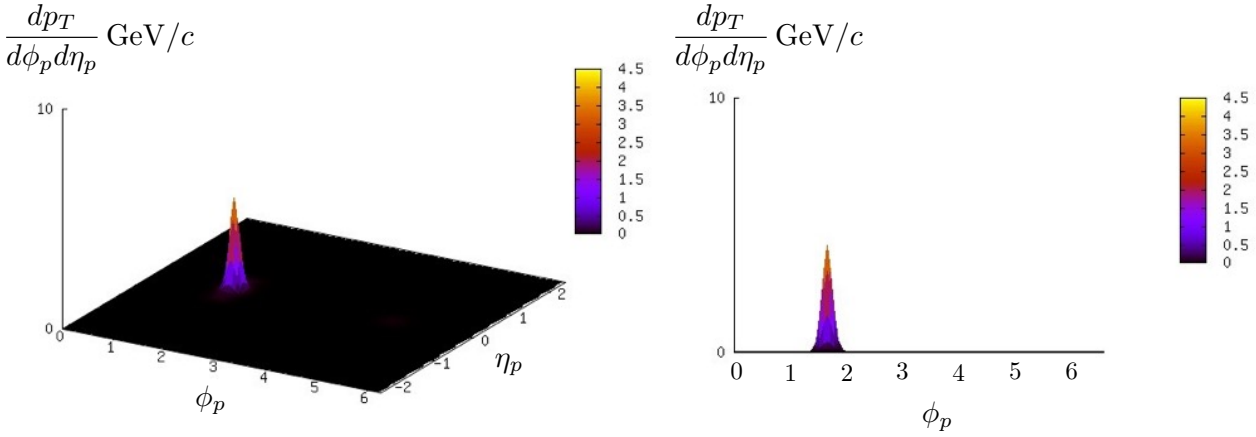

(c) $4\,\mathrm{GeV}/c < p_T < 8\,\mathrm{GeV}/c$

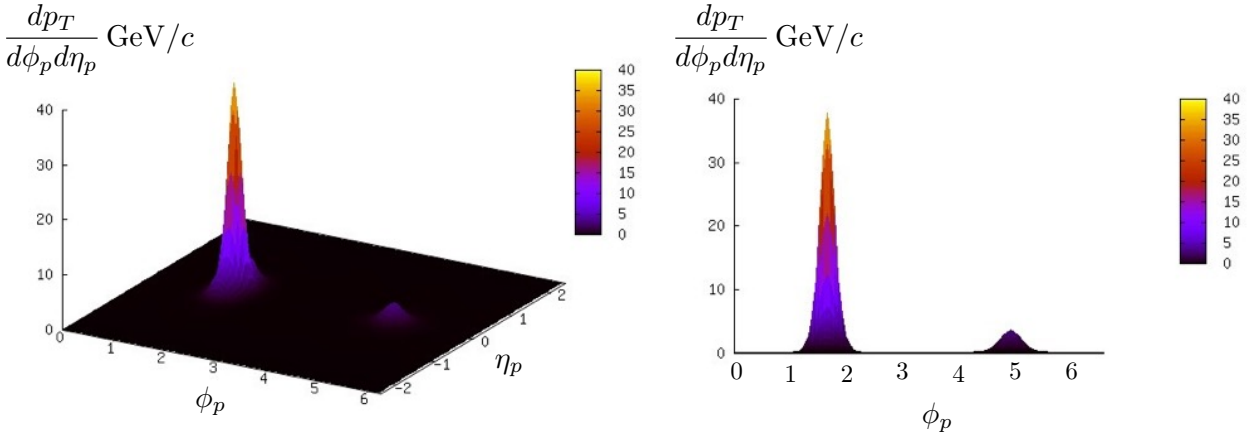

(d) $2\,\mathrm{GeV}/c < p_T < 4\,\mathrm{GeV}/c$

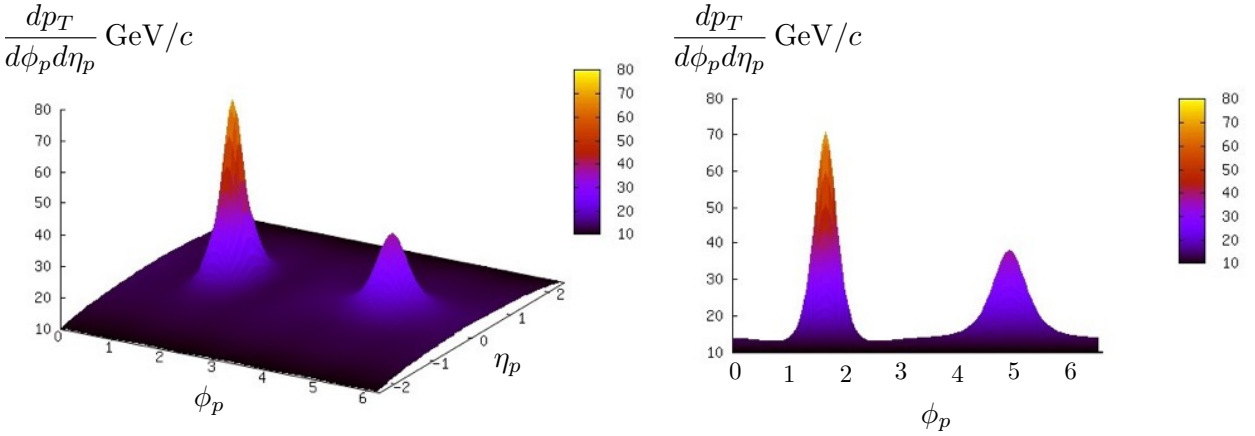

(e) $1\,\mathrm{GeV}/c < p_T < 2\,\mathrm{GeV}/c$

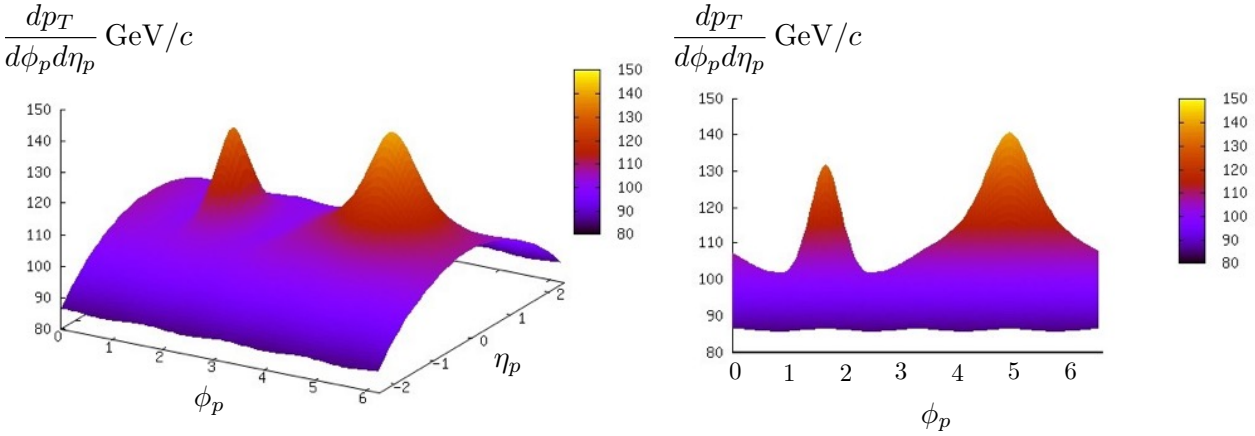

(f) $0.5\,\mathrm{GeV}/c < p_T < 1\,\mathrm{GeV}/c$

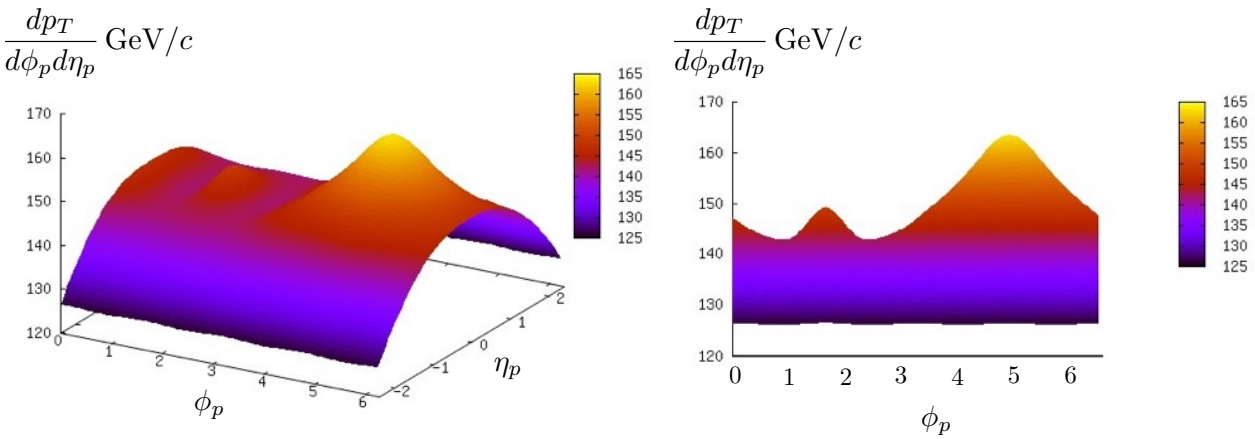

Figure 4.5: Transverse momentum density in ϕ_p-η_p plane $\frac{dp_T}{d\phi_p d\eta_p}$ for the dijet asymmetric event with $y_0 = 3.0\,\mathrm{fm}$. Only the contribution of the particles from the medium is included. The right figures show the view of the left figures along the η_p-axis. Figure (a) shows total $\frac{dp_T}{d\phi_p d\eta_p}$ of the particles from the medium. Figures (b), (c), (d), (e) and (f) shows the contribution in five p_T-ranges: 8-, 4-8, 2-4, 1-2 GeV and 0.5-1 GeV, respectively.

Chapter 5

Collective Flow in the Triggered Dijet Events

In the previous chapter, we have fixed the dijet production points and the initial energies of dijet. However, they are determined stochastically in actual events observed in experiments. Furthermore, only the events in which the dijets are observed with the energy larger than the trigger threshold are selected as dijet events in the analysis of the experimental data. In this chapter, we perform simulations by changing both the jet production points and the initial energies of dijet. Then, we take the event average weighted by the dijet production rate as a function of the dijet creation point and dijet transverse momentum. We also introduce trigger threshold for jets' momenta in final states to select the dijet events similar to that in the experiments. Jets with lower energies are produced much more frequently because the jet production rate is a steeply decreasing function of the jet energy. If such low energy jets travel through the center of the medium, they will not be triggered in the final state because they lose much energy in the medium. Thus, dijet events with rather off-central path are dominant when the event average is taken. As we have seen in the previous chapter, the shape of Mach cones are largely modified by the radial flow depending on their geometry and the Mach cones in the events with off-central path is expected to be asymmetrically distorted. Here, we investigate whether the enhancement of low-p_T particles at large angles from jets can be seen as the hydrodynamic response to the jets when the contributions of events with such asymmetrically distorted Mach cone are properly taken into account. The work presented in this chapter is our original work in collaboration with Tetsufumi Hirano (Sophia Univ.). Based on discussions with the collaborator, the auther carried out the formulation, the implementation of the programs and the analysis.

5.1 Dijet Production and Trigger

We perform simulations of dijet event in the central Pb-Pb collisions at $\sqrt{s_{NN}} = 2.76\,\mathrm{TeV}$. The origin ($x = 0$, $y = 0$, $\eta_s = 0$) is set at the center of the QGP fluid.

We discretize the region $x \geq 0$ and $y \geq 0$ in the transverse plane $\eta_s = 0$ with $0.3\,\mathrm{fm} \times 0.3\,\mathrm{fm}$ square lattice. The dijet is produced at the every lattice point in the QGP with $T > 0.175$ GeV and then travels in the opposite direction along the y axis at the speed of light [Fig. 5.1]. The procedure above covers any path of the jets in the QGP in the completely central collisions. To evaluate the effect of the number of dijet events, we use $n_{\mathrm{coll}}(x, y)$ at the jet production points calculated by the Glauber model. As in the previous chapter, these jets do not interact with

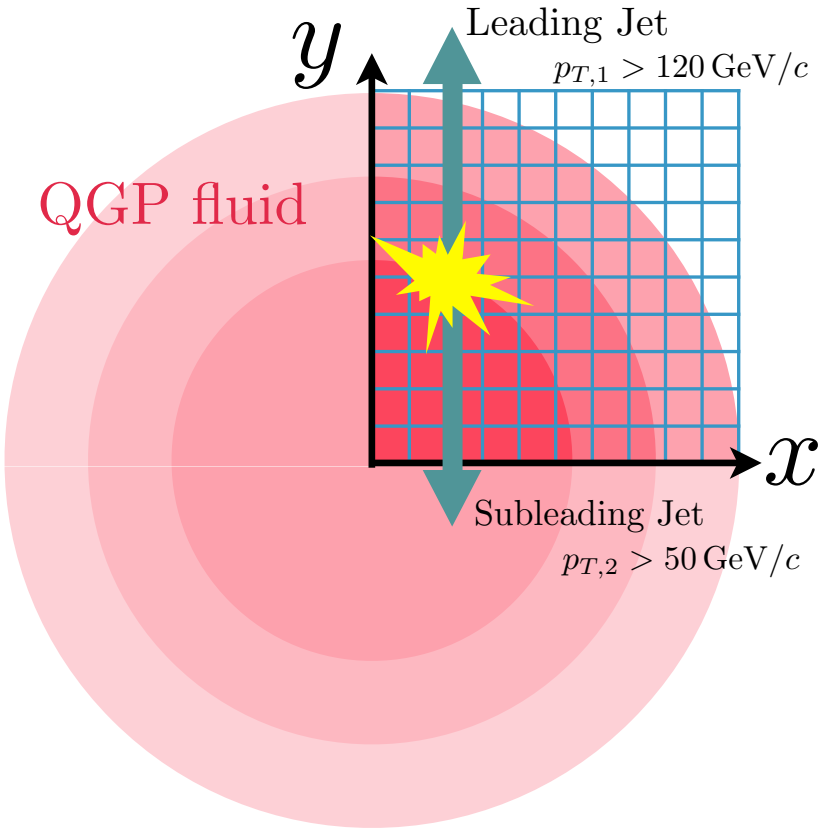

Figure 5.1: Geometry for the simulation of the dijet asymmetric event in Chap. 5

the QGP medium until $\tau = \tau_0 = 0.6\,\mathrm{fm}/c$. At $\tau = \tau_0$, they start to deposite their energy and momentum into the fluid.

We consider three different initial energies of the jets $p_a^0\,(\tau = 0) = 140$, 160, 180 GeV. For the momentum distribution of the jets at $\tau = 0$, we use the leading jet p_T distributions in p-p collisions of the form,

$$\frac{1}{N_{\mathrm{jet}}^{\mathrm{pp}}} \frac{dN_{\mathrm{jet}}^{\mathrm{pp}}}{dp_T} = \frac{1}{p_0} \left(\frac{p_0}{p_T} \right)^{\alpha}. \tag{5.1}$$

The parameters p_0 and α are chosen as $p_0 = 137\,\mathrm{GeV}/c$ and $\alpha = 6.44$ to reproduce the data by the CMS Collaboration in p-p collisions at $\sqrt{s} = 2.76\,\mathrm{TeV}$ [132].

Events with the leading jet with $p_T^{\mathrm{jet1}} > 120\,\mathrm{GeV}/c$ and the subleading jet with $p_T^{\mathrm{jet2}} > 50\,\mathrm{GeV}/c$ in the final state are triggered as the dijet events.

5.2 Numerical Results

5.2.1 Dijet asymmetry ratio

We count the number of triggered dijet events weighted by $n_{\rm coll}(x, y)$ at the jet production points and the initial momentum distribution of the jets (5.1). In Fig. 5.2 we show the event fraction of the dijet events as a function of the dijet asymmetry ratio. If there is no energy loss of the jets, the event fraction will be unity only at $A_J = 0$. The event fraction in this simulation is shifted to higher A_J: It has a peak around around 0.3-0.4 has a sharp cut off above 0.4. The similar features are seen in the data from the ATLAS collaboration [14] and the CMS collaboration [15]. Such event fraction distribution largely shifted to higher A_J is realized by introducing the phenomenologocal parameter $A = 15$ in Eq. (3.22) to gain a large amount of jet energy loss.

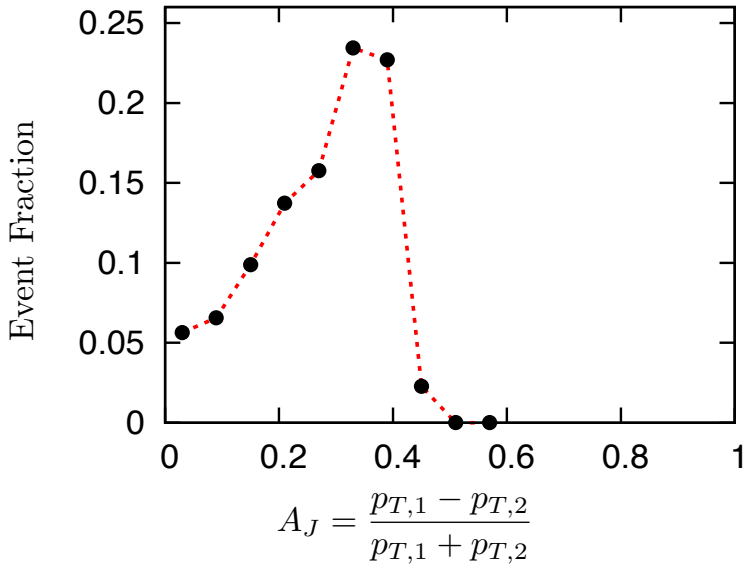

Figure 5.2: The event fraction of the dijet events as a function of the dijet asymmetry ratio.

5.2.2 Space-time evolution of the medium

To see the dominant flow structures in the triggered dijet events, we show the temperature distribution with maximum $n_{\rm coll}$ at the jet production points for each initial momentum of the jets in Figs. 5.3 and 5.4. The detail information of each event is summarized in table 5.1.

The most dominant event is the event (a) in table 5.1. The position of the jet pair creation is far from the center because only the path through the edge of the medium is allowed to be triggered as dijet events for the jets with initial energy 140 GeV. In the transverse plane, the

	$p_a^0(\tau = 0)$	$(x_0,\, y_0)$	$n_{\rm coll}(x_0,\, y_0)$	A_J
(a)	140 GeV	(2.7 fm, 4.5 fm)	10.27	0.402
(b)	160 GeV	(0.6 fm, 4.2 fm)	16.69	0.393
(c)	180 GeV	(0.6 fm, 3.3 fm)	21.12	0.316

Table 5.1: The position of the jet pair creation $(x_0,\, y_0)$ and dijet asymmetry ratio A_J of the triggered dijet event with maximum $n_{\rm coll}$ at the jet production points for each initial momentum of the jets.

Mach cone induced by the subleading jet is pushed by the radial expansion of the medium. As a result, the Mach cone is asymmetrically distorted and inclined to the inside of the medium. On the other hand, the shape of the Mach cone in the reaction plane is not modified so much because the flow in the longitudinal direction is almost same elsewhere at the midrapidity region.

The jets with the initial energy 160 GeV and 180 GeV can travel rather close to the center of the medium. In the events (b) and (c) in table 5.1, the Mach cones propagate almost the center of the medium and their shapes are not modified largely from ones we have seen in the previous simulations.

5.2.3 Event-averaged missing transverse momentum

We calculate the event-averaged missing transverse momentum $\langle \not{p}_T^{||} \rangle$ by taking the sum of $\not{p}_T^{||}$ weighted by $n_{\rm coll}(x,\, y)$ at the jet production points and the initial momentum distribution of the jets (5.1). Figure 5.5 shows the A_J dependence of $\langle \not{p}_T^{||} \rangle$ in the same way as Fig. 4.4.

We can also see the low-$p_T$enhancement even after the event average. Especially for large values of A_J, low-p_T particles are more enhanced in the out-of-cone region.

Although various structures of the collective flow are seen in the simulations, the low-p_T enhancement at large angles is maintained even after averaging over the dijets events. Thus, it is a universal phenomenon that the hydrodynamic response to the jet propagation in the QGP induces the low-p_T enhancement at large angles from the jet. This fact shows the relationship between the hydrodynamic response to the jet propagation in the QGP and the actual phenomenon observed in HIC.

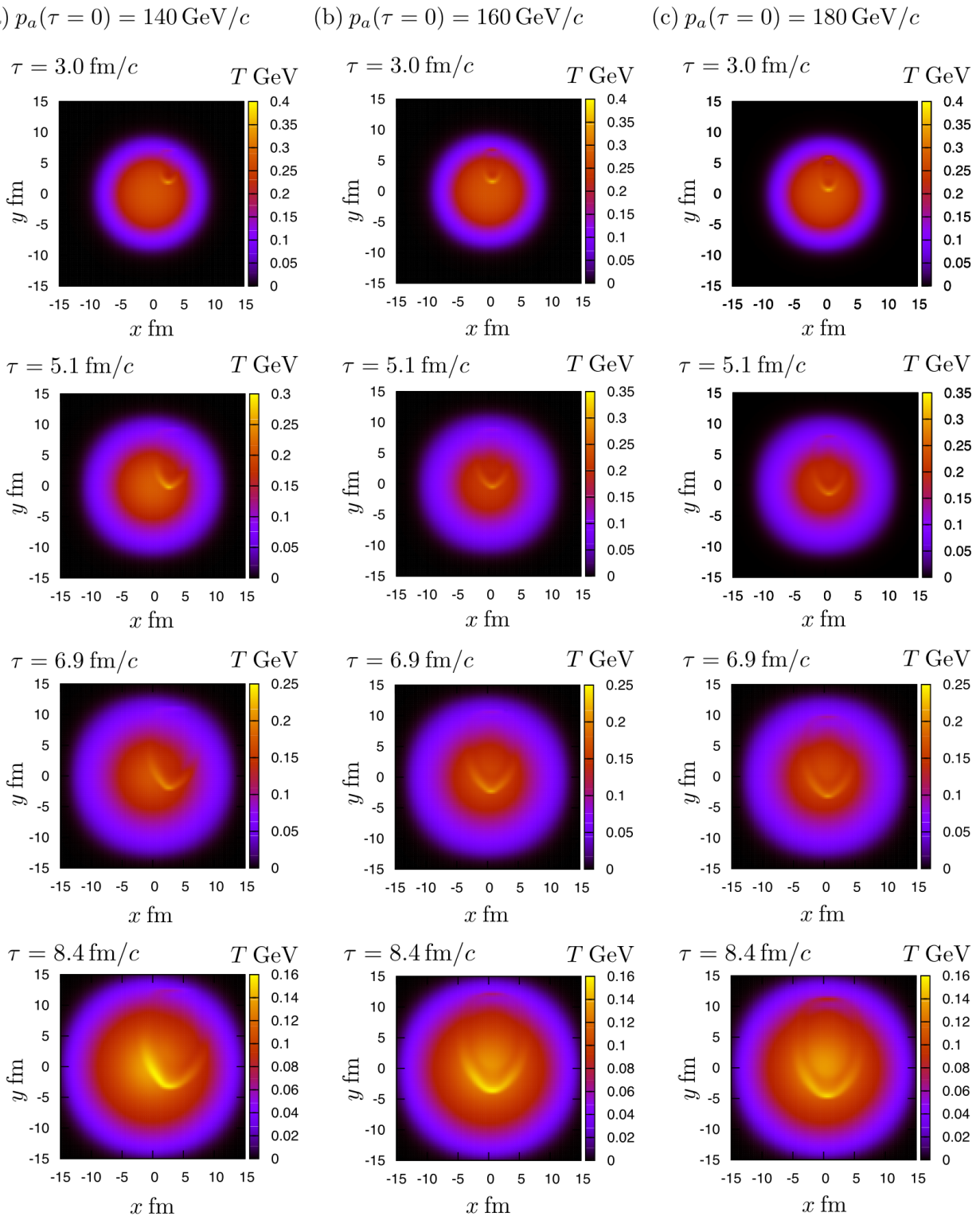

Figure 5.3: Temperature distribution of the expanding QGP fluid in transverse plane at midrapidity $\eta_s = 0$. The triggered dijet event with maximum n_{coll} at the jet production points is selected for each initial momentum of the jets. A pair of jets is produced with $p_a^0(\tau = 0) = 140$ GeV (a), 160 GeV (b), and 180 GeV (c). Then, the jets travels in the opposite direction along the y-axis at the speed of light. The snapshots are taken at $\tau = 3.0\,\mathrm{fm}/c$, $\tau = 5.1\,\mathrm{fm}/c$, $\tau = 6.9\,\mathrm{fm}/c$ and the proper time when the maximum temperature of the medium gets lower than the freezeout temperature $T_f = 0.16$ GeV.

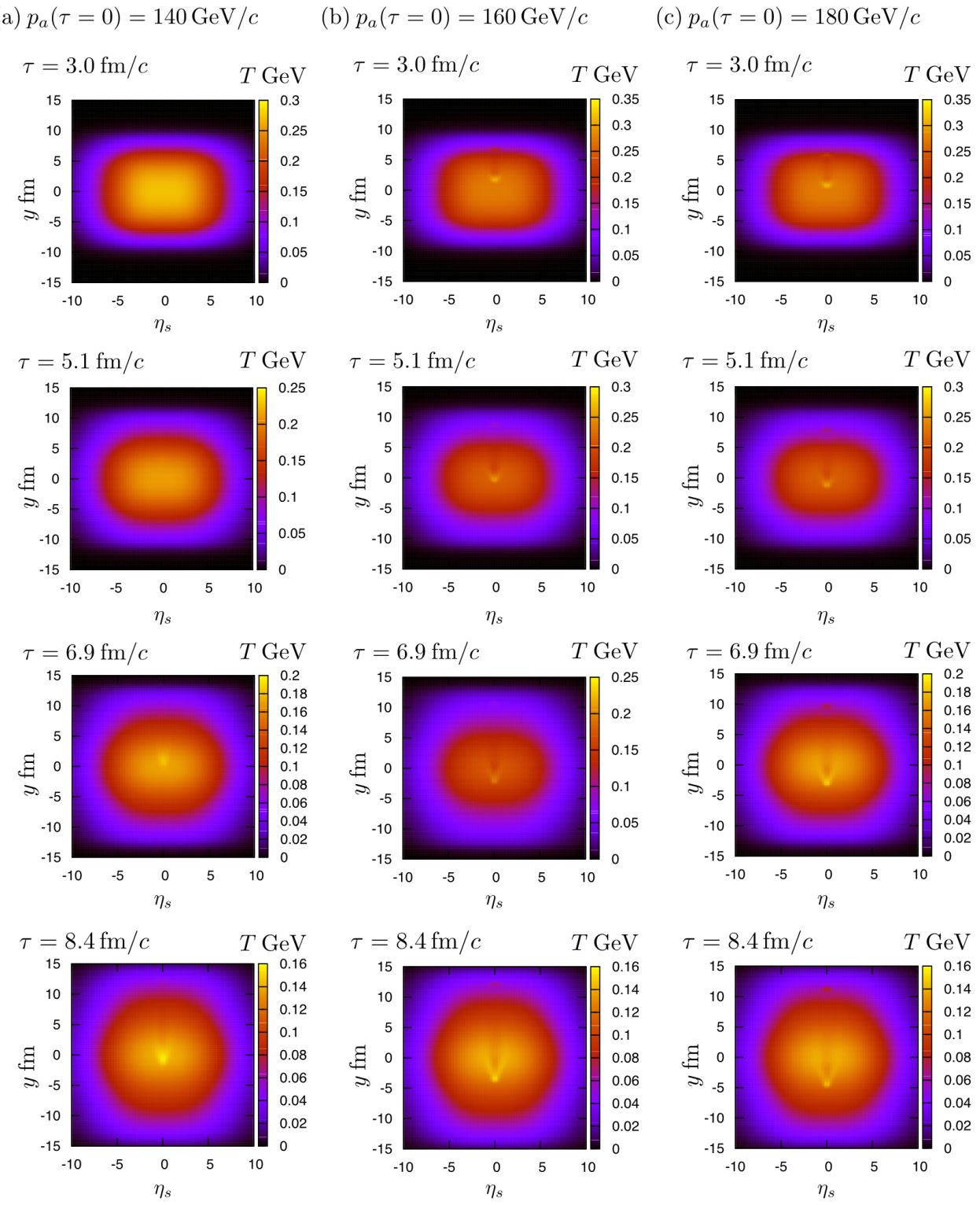

Figure 5.4: Temperature distribution of the expanding QGP fluid in reaction plane at $x = 0$. The triggered dijet event with maximum n_{coll} at the jet production points is selected for each initial momentum of the jets. A pair of jets is produced with $p_a^0(\tau = 0) = 140$ GeV (a), 160 GeV (b), and 180 GeV (c). Then, the jets travels in the opposite direction along the y-axis at the speed of light. The snapshots are taken at $\tau = 3.0\,\mathrm{fm}/c$, $\tau = 5.1\,\mathrm{fm}/c$, $\tau = 6.9\,\mathrm{fm}/c$ and the proper time when the maximum temperature of the medium gets lower than the freezeout temperature $T_f = 0.16$ GeV.

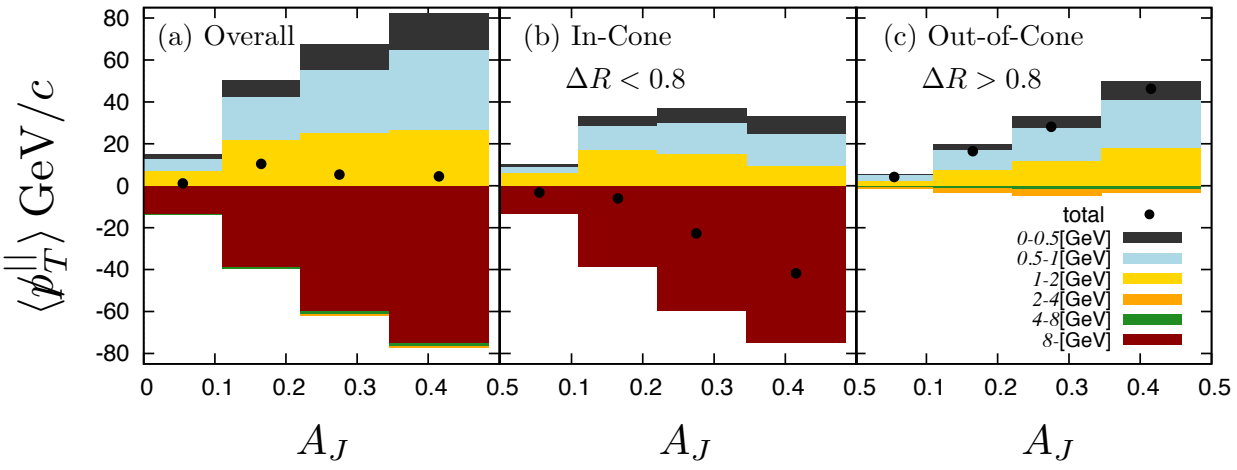

Figure 5.5: $\langle p_T^{||} \rangle$ as a function of the dijet asymmetry ratio A_J. Figure (a), (b) and (c) show the contribution from the over all region, inside the leading jet cone or subleading jet cone ($\Delta R < 0.8$), and outside both of the leading and subleading jet cones ($\Delta R > 0.8$) in the momentum space. Each colored histogram represents the contribution to $\langle p_T^{||} \rangle$ from six transverse-momentum ranges: 0-0.5, 0.5-1, 1-2, 2-4, 4-8 GeV/c, and $p_T > 8$ GeV/c.

Chapter 6

Summary

In this thesis, we studied collective response of the QGP fluid under the energy-momentum deposition from jets. Such collective response contains information of the various properties of QGP *e.g.*, the sound velocity, the viscosity, the stopping power, *etc.* In Pb-Pb collision experiments at LHC, enhancement of low-p_T particles at large angles from the jets is observed in dijet asymmetric events by the CMS collaboration. The observed transverse momenta of the low-p_T particles are sufficiently low so that they can be considered a part of the of hydrodynamic medium. Therefore, the low-p_T enhancement at large angles from the jets can be interpreted as the hydrodynamic response to the jet propagation in the QGP fluid. Motivated by these findings, we studied the space-time evolution of the QGP fluid in dijet asymmetric events to relate the low-p_T enhancement observed in heavy ion collisions (HIC) with the medium response to jet propagation.

In Chap. 2, the overview of HIC and some topics related to this thesis were presented with the experimental data and the current theoretical pictures.

In Chap. 3, we formulated the hydrodynamic model with the source terms. In the conventional hydrodynamic model, the space-time evolution of the QGP medium is described by the energy-momentum conservation. To consider the incoming energy and momentum from jets to the fluid, we introduce the source terms, assuming the instantaneously thermalization of the deposited energy and momentum in the fluid. We employed the Glauber model for initial condition and the Cooper-Frye formula at the kinetic freezeout to obtain the spectra of the particles after the hydrodynamic space-time evolution. For the energy loss of the jets, we employed the collisional energy loss formula. To reproduce the dijet events with large A_J such as observed in HIC, we amplified the energy loss by phenomenological parameter $A = 15$. The ideal gas equation of state for QGP which does not include the hadronization process is employed in the hydrodynamic calculation and massless quarks and gluons are yielded after the kinetic freezeout. This might have been too simplified but the energy and momentum are strictly conserved at the kinetic freezeout as well as in hydrodynamic evolution.

In Chap. 4, we performed simulations in the case of the dijet traveling through the center of the expanding medium. A pair of jets travels through the center of the medium and the

jets deposits their energies and momenta into the medium. Since the jets move faster than the sound velocity of the fluid, Mach cones are induced: How they evolve depends on the geometry of the QGP fluid. The structure of the Mach cones in the transverse plane is modified largely by the radial expansion of the medium. We also calculated the spectra from the medium by using the Cooper-Frye formula to study how the spectra is modified by the dijet. As a result of the hydrodynamic response to the jet propagations, the yield of low-p_T particles, which carries the energy and momentum deposited from jets, increases at large angles from the jet axis. This agrees with the tendency seen in the experimental data taken at LHC by the CMS collaboration [15]. Despite of clear flow structures in the QGP fluid, no ring-shaped spectra reflecting the Mach cone structure appeared. Possible causes are strong flow following jets, the employment of the Cooper-Frye formula at the kinetic freezeout and distortion of the Mach cone by the medium expansion. The absence of the ring-shaped spectra agrees with the observation by the CMS Collaboration [Fig. 1.1].

In Chap. 5, we performed more realistic simulations by considering the spacial distribution of the jet production points, the initial momentum distribution of the jets and trigger threshold of the jet p_T. The dijet is produced at the every lattice point in the transverse plane inside the QGP and then travels in the opposite direction. The contribution of an event with each jet production point is weighted by the distribution of binary collisions n_{coll}. We used three different initial energies of jets 140, 160, 180 GeV: The contribution of an event with each initial energy is weighted by the jet p_T distributions in p-p collisions. We counted the events with the leading jet with $p_{T,1} > 120\,\mathrm{GeV}$ and the subleading jet with $p_{T,2} > 50\,\mathrm{GeV}$ in the final state as the dijet events. In these simulations, events with the dijet traveling through the edge of the medium are included. In such events, the Mach cones are largely distorted because they propagate against the radial expansion of the medium. Although various structures of the collective flow are seen in the simulations, the low-p_T enhancement at large angles is maintained even after averaging over the dijets events. Thus, it is a universal phenomenon that the hydrodynamic response to the jet propagation in the QGP induces the low-p_T enhancement at large angles from the jet. This fact shows a solid relationships between the hydrodynamic response to the jet propagation in the QGP and the observed phenomenon in HIC.

The results in this thesis shed light on a new phenomenological approach to extract the properties of QGP by focusing on low-momentum particles at large angles from jet axis. The amount of deposited energy and momentum can be estimated from quantitative comparison of momentum distribution around the jet between the theoretical calculation and the experimental data. The shear viscosity of the QGP can also be estimated from quantitative analysis of the azimuthal angle distribution of the low-p_T particles around the jet, since Mach cone structure is smeared out with increasing shear viscosity of the QGP. The number of particles emitted at large angles from the jet axis is supposed to decrease for larger shear viscosity. To realize such quantitative comparison of the theoretical calculations and the experimental data, it is important to develop the model as introduced in employed in this thesis and make further

systematic studies of the hydrodynamic response to the jet propagation.

Acknowledgements

First of all, I am grateful to my supervisor, Prof. Tetsuo Hatsuda whose comments and support were of inestimable value for my study. I would like to thank Prof. Tetsufumi Hirano for collaboration and for giving me many valuable advice and suggestions. I would also like to thank Prof. Tetsuo Matsui, Prof. Hideki Hamagaki, Prof. Masaki Sano, Prof. Toshio Terasawa and Prof. Hidetoshi Yamaguchi for refereeing my thesis and for valuable discussions. Moreover, I would like to thank my colleagues in the working group, Y. Hirono, M. Hongo, R. Kurita and K. Murase for useful discussions. The work of the autheor is supported by a JSPS Research Fellowship for Young Scientists and by a grant from the Advanced Leading Graduate Course for Photon Science. This work was supported by JSPS KAKENHI Grants No. 13J02554.

Appendix A

Geometrical Setup for HIC

A.1 Space-time Coordinates

Milne coordinate is employed to describe the space-time of the medium in HIC. We take the collision axis as the z-axis and the transverse plane as the xy-plane in Cartesian coordinates. Then, One writes Milne coordinates $(\tau, x, y, \eta_{\rm s})$ in terms of Cartesian coordinates (t, x, y, z) as follows:

$$\tau = \sqrt{t^2 - z^2}, \tag{A.1}$$

$$\eta_{\rm s} = \frac{1}{2} \ln \frac{t+z}{t-z}. \tag{A.2}$$

τ and $\eta_{\rm s}$ are called proper time and space-time rapidity, respectively. x and y are the same in the both coordinate systems. On the contrary, t and z are written in terms of τ and $\eta_{\rm s}$ as

$$t = \tau \cosh \eta_{\rm s}, \tag{A.3}$$

$$z = \tau \sinh \eta_{\rm s}. \tag{A.4}$$

The coordinate transformation from Cartesian coordinates to Milne coordinates corresponds to the "local" Lorentz boost of the frame with the velocity $\beta_s = z/t$ in z-direction:

$$\Lambda^{\alpha}{}_{\mu}(\beta_s) = \begin{pmatrix} \gamma & 0 & 0 & -\gamma\beta_s \\ 0 & 1 & 0 & 0 \\ 0 & 0 & 1 & 0 \\ -\gamma\beta_s & 0 & 0 & \gamma \end{pmatrix}, \tag{A.5}$$

where $\gamma = 1/\sqrt{1-\beta_s^2}$ is the Lorentz factor, α is a suffix for the Milne coordinates and μ is a suffix for the Cartesian coordinates.

A.2 Momentum Coordinates

A detected particle in collider experiments are usually labeled with its transverse momentum p_T and pseudorapidity η_p. p_T is the component of the particle's momentum $\boldsymbol{p} = (p_x,\, p_y,\, p_z)$

transverse to z-axis:

$$p_T = \sqrt{p_x^2 + p_y^2} = |\boldsymbol{p}| \sin\theta, \tag{A.6}$$

where θ is the poler angle of $\boldsymbol{p}$ with respect to z-axis. The pseudorapidity corresponds one-to-one to θ:

$$\eta_p = -\log\left(\tan\frac{\theta}{2}\right). \tag{A.7}$$

p_T and η_p are independent of the particle's mass.

On the other hand, rapidity is defined as

$$y = \frac{1}{2}\log\frac{E + p_z}{E - p_z} = \frac{1}{2}\log\frac{1+\beta}{1-\beta}, \tag{A.8}$$

where $E = \sqrt{m^2 + |\boldsymbol{p}|^2}$ is the energy of the particle, m is the particle mass and $\beta = p_z/E$ is the velocity in the z-direction. We also define the transverse mass m_T as

$$m_T = \sqrt{m^2 + p_T^2} = \sqrt{E^2 - p_z^2}. \tag{A.9}$$

The particle's four-momentum $p^\mu = (E,\, \boldsymbol{p})$ in Cartesian coordinate can be written as follows:

$$p^\mu = \begin{pmatrix} m_{\mathrm{T}} \cosh y \\ p_{\mathrm{T}} \cos\phi_p \\ p_{\mathrm{T}} \sin\phi_p \\ m_{\mathrm{T}} \sinh y \end{pmatrix}. \tag{A.10}$$

Here, ϕ_p is the azimuthal angle of $\boldsymbol{p}$ in the xy-plane.

In the extremely relativistic limit, i.e. $E \simeq |\boldsymbol{p}| \gg m$, we have

$$m_T \simeq p_T, \tag{A.11}$$

$$y = \frac{1}{2}\log\frac{E + p_z}{E - p_z} \simeq \frac{1}{2}\log\frac{|\boldsymbol{p}| + p_z}{|\boldsymbol{p}| - p_z} = \frac{1}{2}\log\frac{1+\cos\theta}{1-\cos\theta} = -\log\left(\tan\frac{\theta}{2}\right) = \eta_p. \tag{A.12}$$

Thus, when the mass of the particle is negligible, the transverse mass and the rapidity coincide with the transverse momentum and pseudorapidity, respectively.

A.3 Freezeout Hypersurface

The general expression of the Cooper-Frye formula [45] is given by

$$p^0 \frac{dN}{d^3p} = \int_\Sigma (p \cdot d\sigma)\, f(p \cdot u(x)), \tag{A.13}$$

where N, p and f are the number, the momentum, and the momentum distribution function at the kinetic freezeout respectively.

In terms of the transverse momentum p_T, the momentum azimuthal angle ϕ_p and the rapidity y, 3-dimensional momentum differentiation in Eq. (A.13) is given by

$$d^3p = m_{\rm T} p_{\rm T} \cosh\eta_{\rm p} dp_{\rm T} d\phi_{\rm p} d\eta_{\rm p}. \tag{A.14}$$

Thus, the left-hand side of Eq. (A.13) can be written as

$$E\frac{dN}{d^3p} = m_{\rm T}\cosh\eta_p \frac{dN}{m_{\rm T}p_{\rm T}\cosh\eta_p dp_{\rm T} d\phi_p d\eta_{\rm s}} = \frac{dN}{p_{\rm T} dp_{\rm T} d\phi_p d\eta_p}. \tag{A.15}$$

The product of the particle's momentum and four-flow velocity in Eq. (A.13)

$$p\cdot u = p^\mu u_\mu = p^\alpha u_\alpha, \tag{A.16}$$

where α is an index for the Milne coordinates and μ is an index for the Cartesian coordinates. In the Milne coordinates, the momentum of the particle is

$$p^\alpha = \Lambda(\eta_{\rm s})^\alpha_{\ \mu}\, p^\mu = \begin{pmatrix} m_{\rm T}\cosh(y-\eta_{\rm s}) \\ p_{\rm T}\cos\phi_p \\ p_{\rm T}\sin\phi_p \\ m_{\rm T}\sinh(y-\eta_{\rm s}) \end{pmatrix}. \tag{A.17}$$

Similary, the product of the particle's momentum and the hypersurface element in Eq. (3.33) is

$$p\cdot d\sigma = p^\mu d\sigma_\mu = p^\alpha d\sigma_\alpha, \tag{A.18}$$

and the hypersurface element in the Milne coordinates is given by

$$d\sigma^\alpha = \begin{pmatrix} dxdy\tau d\eta_s \\ -d\tau dy\tau d\eta_s \\ -d\tau dx\tau d\eta_s \\ -d\tau dydy \end{pmatrix}. \tag{A.19}$$

Then, the explicit form of $p\cdot u$ and $p\cdot d\sigma$ are

$$p\cdot u = m_{\rm T}[u^\tau\cosh(\eta_p - y) - u^\eta\sinh(\eta_p - y)] + p_{\rm T}[-u^x\cos(\phi_p) - u^y\sinh(\phi_p)], \tag{A.20}$$

$$p\cdot d\sigma = m_{\rm T}[\cosh(\eta_p-\eta)\, d\sigma^\tau - \sinh(\eta_p-\eta)\, d\sigma^\eta] + p_{\rm T}[-\cos\phi_p d\sigma^x - \sin\phi_p d\sigma^y]. \tag{A.21}$$

Appendix B

Numerical Relativistic Hydrodynamics

B.1 Relativistic Hydrodynamics in Cartesian Coordinate

The relativistic hydrodynamic equations consist of the energy-momentum conservation law and continuity equations for conserved charges:

$$T^{\mu\nu}{}_{;\mu} = 0, \quad N_i^{\mu}{}_{;\mu} = 0. \tag{B.1}$$

Here, $T^{\mu\nu}$ is the energy-momentum tensor of the fluid and N_i^{μ} is the i-th conserved charge-current density. The sign ; before a lower suffix denotes a covariant derivative.

For perfect fluids, idealized model where all dissipative effects are neglected, the energy momentum tensor and charge-current densities can be decomposed as

$$T^{\mu\nu} = (e + P)u^{\mu}u^{\nu} - Pg^{\mu\nu}, \quad N_i^{\mu} = n_i u^{\mu} \tag{B.2}$$

where e, P, n_i, $u^{\mu} = \gamma\,(1, \boldsymbol{v}) = \frac{1}{\sqrt{1-v^2}}\,(1, \boldsymbol{v})$, and $g^{\mu\nu}$ are energy density, pressure, i-th conserved charge density four-flow velocity, and metric, respectively. Hereafter we omit the index i for conserved charge.

In numerical aspect, the expression in forms of continuity equation for each components of the energy-momentum tensor is more convenient. The expressions in Cartesian coordinate are the following,

$$\frac{\partial}{\partial x^0}T^{0\nu} = -\frac{\partial}{\partial x^i}T^{i\nu}, \tag{B.3}$$

where $i = 1, 2, 3$ is an index for spatial coordinate. The variables time-evolving in the numerical calculation program are chosen as

$$U^{\mu} = T^{0\mu}, U_N = N^0. \tag{B.4}$$

The other components can be written as

$$T^{i0} = v^i \left(T^{00} - P\right), \tag{B.5}$$

$$T^{ij} = v^i T^{0j} - P\delta^{ij}. \tag{B.6}$$

$$N^i = v^i N^0, \tag{B.7}$$

The equations (B.1) in Cartesian coordinate can be summarized as continuity equations in the following general form

$$\frac{\partial}{\partial x^0}U = -\frac{\partial}{\partial x^i}F^i\left(U\right). \tag{B.8}$$

All thermodynamic variables and flow velocity can be calculated from U^μ and U_N together with the equation of state $P = P(e,\, n)$,

$$v = |\boldsymbol{v}| = \frac{|\boldsymbol{U}|}{U^0 + P(e,n)}, \tag{B.9}$$

$$e = U^0 - |\boldsymbol{U}|\, v, \tag{B.10}$$

$$n = \frac{U_N}{\tau}\sqrt{1-v^2}, \tag{B.11}$$

$$\boldsymbol{U} = (U^1, U^2, U^3). \tag{B.12}$$

B.2 Discretization and the Operator Splitting Method

The equations (B.8) discretized in time direction are

$$\frac{U^{(n+1)} - U^{(n)}}{\Delta t} = -\frac{\partial}{\partial x^i}F^i\left(U^{(n)}\right), \tag{B.13}$$

where n is a time step index and Δt is an interval of the time step.

For each time step, the variables U evolve subject to the following equations,

$$U^{(n+1)} = U^{(n)} - \Delta t\left[\frac{\partial}{\partial x^1}F^1\left(U^{(n)}\right) + \frac{\partial}{\partial x^2}F^2\left(U^{(n)}\right) + \frac{\partial}{\partial x^3}F^3\left(U^{(n)}\right)\right]. \tag{B.14}$$

Calculating the right-hand side of the equations (B.14) including three-dimensional divergence as they are is quite a formidable numerical task in general. To avoid this difficulty, one usually employs the so-called operator splitting method to split the multi-dimensional equation into the sequential one-dimensional equations. In the continuum limit, instead of the three-dimenssional equations (B.14), it is equivalent to carry out the following three steps:

$$U^{(n+\frac{1}{3})} = U^{(n)} - \Delta t\frac{\partial F^1}{\partial x^1}\left(U^{(n)}\right), \tag{B.15}$$

$$U^{(n+\frac{2}{3})} = U^{(n+\frac{1}{3})} - \Delta t\frac{\partial F^2}{\partial x^2}\left(U^{(n+\frac{1}{3})}\right), \tag{B.16}$$

$$U^{(n+1)} = U^{(n+\frac{2}{3})} - \Delta t\frac{\partial F^3}{\partial x^3}\left(U^{(n+\frac{2}{3})}\right). \tag{B.17}$$

In this procedure, the flux is transferred in x^1-direction first, then in x^2 direction, and then in x^3 direction. To minimize systematic errors on spatial anisotropy associated with the order of the three steps (B.17), one permutates the order x^1, x^2, x^3, every time-step in actual numerical applications.

The hydrodynamic equations in three dimensional space reduce to the continuity equations in one dimensional space equation in the form of

$$U^{(n+1)} = U^{(n)} - \Delta t \frac{\partial F}{\partial x}\left(U^{(n)}\right). \tag{B.18}$$

Hereafter, we consider only the one-dimensional equation (B.18). From the next section, we focus on the evaluation of the differential term $\frac{\partial F}{\partial x}$ in the discretized space for numerical calcutaions.

B.3 Approximated Solver of the Riemann Problem

One discretizes Eq. (B.18) in the space with equally-spaced interval Δx and write the equation for the i-th discretized space cell in a form

$$U_i^{(n+1)} = U_i^{(n)} - \frac{\Delta t}{\Delta x}\left(F_{i+\frac{1}{2}} - F_{i-\frac{1}{2}}\right), \tag{B.19}$$

where $F_{i+\frac{1}{2}}$ is the value of $F(U)$ at the boundary between the i-th and $(i+1)$-th cell. The main part of the numerical calculation of hydrodynamics is the evaluation of boundary values. In the numerical calculation, there are discontinuities at boundaries between discretized space cells. The problem to solve such a continuity equation together with initial condition having a step-like discontinuity is called a Riemann problem. In the numerical calculation, one solves the problem approximately by using a Riemann solver and obtain the values at the boundary between the cells contained in Eq. (B.74). Here we employ a higher-order extension of Godunov's method consist of the piecewise parabolic method (PPM) [133, 130] and the relativistic Harten-Lax-van Leer-Einfeldt (HLLE) algorithm [134, 135, 136, 137] as a robust Riemann solver.

B.3.1 Piecewise Parabolic Method (PPM)

In this subsection, we review PPM employed to evaluate the values of fields U around the boundary between the cells.

Let $x_{i+\frac{1}{2}} = x_i + \frac{\Delta x}{2}$, the definition of discrete field values at the i-th cell is

$$U_i = \frac{1}{\Delta x}\int_{x_{i-\frac{1}{2}}}^{x_{i+\frac{1}{2}}} dx U(x), \tag{B.20}$$

where $U(x)$ is an interpolation function around the boundary between the i-th and $(i+1)$-th cell and We fit the integral of $U(x)$ by a quartic function with five parameters,

$$\mathcal{U}(x) = \int_{x_{i-\frac{3}{2}}}^{x} d\xi U(\xi) = ax^4 + bx^3 + cx^2 + dx + e, \quad x_{i-\frac{3}{2}} \le x \le x_{i+\frac{5}{2}}, \tag{B.21}$$

and these fitting parameters are fixed by the following equations obtained from Eqs. (B.20) and (B.21)

$$\begin{aligned}
\mathcal{U}(-2\Delta x) &= 0, && \text{(B.22)}\\
\mathcal{U}(-\Delta x) &= \Delta x U_{i-1}, && \text{(B.23)}\\
\mathcal{U}(0) &= \Delta x (U_{i-1}+U_i), && \text{(B.24)}\\
\mathcal{U}(\Delta x) &= \Delta x (U_{i-1}+U_i+U_{i+1}), && \text{(B.25)}\\
\mathcal{U}(2\Delta x) &= \Delta x (U_{i-1}+U_i+U_{i+1}+U_{i+2}), && \text{(B.26)}
\end{aligned}$$

here we can suppose $x_{i+\frac{1}{2}}$ and $\mathcal{U}(x_{i-\frac{3}{2}})=0$ without loss of generality Thus we obtain the value of U at $x_{i+\frac{1}{2}}$ as

$$\begin{aligned}
U_{i+\frac{1}{2}} &= \left.\frac{d\mathcal{U}(x)}{dx}\right|_{x=x_{i+\frac{1}{2}}} = 4a{x_{i+\frac{1}{2}}}^3 + 3b{x_{i+\frac{1}{2}}}^2 + 2cx_{i+\frac{1}{2}} + d && \text{(B.27)}\\
&= \frac{1}{2}(U_i+U_{i+1}) + \frac{1}{6}(\delta U_i - \delta U_{i+1}), && \text{(B.28)}\\
\delta U_i &= \frac{1}{2}(U_{i+1}-U_{i-1}), && \text{(B.29)}
\end{aligned}$$

with a third-order accuracy. To guarantees that $U_{i+\frac{1}{2}}$ lies between U_i and U_{i+1}, one replaces δU_i in Eq. (B.29) by $\delta' U_i$ defined by the following rule:

$$\begin{aligned}
&\delta' U_i = \mathrm{sgn}(\delta U_i)\min\left(|\delta U_i|,\, 2|U_i - U_{i-1}|,\, 2|U_{i+1}-U_i|\right) \quad \text{if } (U_{i+1}-U_i)(U_i-U_{i-1})>0,\\
&\delta' U_i = 0 \qquad\qquad \text{otherwise.}
\end{aligned} \tag{B.30}$$

The results in the above are asigned to default values at cell boundary:

$$\begin{aligned}
U_i^{\mathrm{R}} &= U_{i+\frac{1}{2}} = \frac{1}{2}(U_i+U_{i+1}) + \frac{1}{6}(\delta' U_i - \delta' U_{i+1}), && \text{(B.31)}\\
U_i^{\mathrm{L}} &= U_{i-\frac{1}{2}} = \frac{1}{2}(U_{i-1}+U_i) + \frac{1}{6}(\delta' U_{i-1} - \delta' U_i). && \text{(B.32)}
\end{aligned}$$

Next, we concentrate on one cell which has the mean value of in the cell U_i and the value at both ends U_i^{R} and U_i^{L}. One interpolates U_i^{R} and U_i^{L} with a quadratic function $U_i(x)$ satisfying the definition (B.20):

$$\begin{aligned}
U_i(x) &= U^{\mathrm{L}} + \frac{x-x_{i-\frac{1}{2}}}{\Delta x}\left[\Delta U_i + U_i^6\left(1-\frac{x-x_{i-\frac{1}{2}}}{\Delta x}\right)\right], && \text{(B.33)}\\
U_i^6 &= 6\left[U_i - \frac{1}{2}\left(U_i^{\mathrm{R}}+U_i^{\mathrm{L}}\right)\right], && \text{(B.34)}\\
\Delta U_i &= U_i^{\mathrm{R}} - U_i^{\mathrm{L}}. && \text{(B.35)}
\end{aligned}$$

To impose monotonicity constraint on the interpolation function $U(x)$ in the cell, one replaces the values at cell boundary U_i^{R} and U_i^{L}, according to the following procedure [Fig. B.1]:

$$\begin{aligned}
&U_i^{\mathrm{R}} \to U_i,\ U_i^{\mathrm{L}} \to U_i \quad \text{if } \left(U_i^{\mathrm{R}}-U_i\right)\left(U_i-U_i^{\mathrm{L}}\right)\le 0,\\
&U_i^{\mathrm{L}} \to 3U_i - 2U_i^{\mathrm{R}} \qquad \text{if } \Delta U_i U_i^6 > \Delta U^2,\\
&U_i^{\mathrm{R}} \to 3U_i - 2U_i^{\mathrm{L}} \qquad \text{if } \Delta U_i U_i^6 < -\Delta U^2.
\end{aligned} \tag{B.36}$$

Averages of the interpolation functions around the cell boundaries are

$$\bar{U}_i^{\mathrm{R}} = \frac{1}{\lambda_i^{\mathrm{R}}\Delta t}\int_{x_{i+\frac{1}{2}}-\lambda_i^{\mathrm{R}}\Delta t}^{x_{i+\frac{1}{2}}} dx U_i\left(x\right), \tag{B.37}$$

$$\bar{U}_{i+1}^{\mathrm{L}} = \frac{1}{\lambda_{i+1}^{\mathrm{L}}\Delta t}\int_{x_{i+\frac{1}{2}}}^{x_{i+\frac{1}{2}}+\lambda_{i+1}^{\mathrm{L}}\Delta t} dx U_{i+1}\left(x\right). \tag{B.38}$$

A reasonable estimation for λ^{L} and λ^{R} is the following [Fig. B.2]:

$$\begin{array}{ll} \lambda_i^{\mathrm{L}} = \left|\max\left(0, \frac{c_i^{\mathrm{L}}-v^{\mathrm{L}}}{1-c_i^{\mathrm{L}}v_i^{\mathrm{L}}}, \frac{\bar{c}_i^{\mathrm{L}}-\bar{v}_i^{\mathrm{L}}}{1-\bar{c}_i^{\mathrm{L}}\bar{v}_i^{\mathrm{L}}}\right)\right|, & \lambda_i^{\mathrm{R}} = \left|\max\left(0, \frac{c_i^{\mathrm{R}}+v_i^{\mathrm{R}}}{1+c_i^{\mathrm{R}}v_i^{\mathrm{R}}}, \frac{\bar{c}_i^{\mathrm{R}}+\bar{v}_i^{\mathrm{R}}}{1+\bar{c}_i^{\mathrm{R}}\bar{v}_i^{\mathrm{R}}}\right)\right|, \\ \bar{v}_i^{\mathrm{L}} = \frac{1}{2}\left(v_i^{\mathrm{L}} + v_{i-1}^{\mathrm{R}}\right), & \bar{v}_i^{\mathrm{R}} = \frac{1}{2}\left(v_i^{\mathrm{R}} + v_{i+1}^{\mathrm{L}}\right) \\ \bar{c}_i^{\mathrm{L}} = \frac{1}{2}\left(c_i^{\mathrm{L}} + c_{i-1}^{\mathrm{R}}\right), & \bar{c}_i^{\mathrm{R}} = \frac{1}{2}\left(c_i^{\mathrm{R}} + c_{i+1}^{\mathrm{L}}\right) \end{array} \tag{B.39}$$

where c^{L} and c^{R} are the sound velocities at the cell boundaries. One integrates Eq. (B.35) inserting into Eqs. (B.37) and (B.37):

$$\bar{U}_i^{\mathrm{L}} = U^{\mathrm{L}} + \frac{\lambda_i^{\mathrm{L}}\Delta t}{2}\left(\Delta U_i + \left(1 - \frac{2}{3}\lambda_i^{\mathrm{L}}\Delta t\right)U_i^6\right) \tag{B.40}$$

$$\bar{U}_i^{\mathrm{R}} = U^{\mathrm{R}} - \frac{\lambda_i^{\mathrm{R}}\Delta t}{2}\left(\Delta U_i - \left(1 - \frac{2}{3}\lambda_i^{\mathrm{R}}\Delta t\right)U_i^6\right) \tag{B.41}$$

B.3.2 Relativistic Harten-Lax-van Leer-Einfeldt (rHLLE) Algorithm

rHLLE approximately solves the Riemann problem whose initial conditions around the boundary $x = x_{i+\frac{1}{2}}$ are, cf. Fig. B.3:,

$$U\left(x, t=0\right) = \begin{cases} \bar{U}_i^{\mathrm{R}}, & x \le x_{i+\frac{1}{2}} \\ \bar{U}_{i+1}^{\mathrm{L}}, & x > x_{i+\frac{1}{2}} \end{cases}. \tag{B.42}$$

The solution is approximated by a region of constant value between $\bar{U}_i^{\mathrm{R}}$ and $\bar{U}_{i+1}^{\mathrm{L}}$, cf. Fig. B.3:

$$U\left(x,t\right) = \begin{cases} \bar{U}_i^{\mathrm{R}}, & x \le x_{i+\frac{1}{2}} + b_i^{\mathrm{R}}t \\ \bar{U}_{i+\frac{1}{2}}, & x_{i+\frac{1}{2}} + b_i^{\mathrm{R}}t < x < x_{i+\frac{1}{2}} + b_{i+1}^{\mathrm{L}}t \\ \bar{U}_{i+1}^{\mathrm{L}}, & x \ge x_{i+\frac{1}{2}} + b_{i+1}^{\mathrm{L}}t \end{cases}. \tag{B.43}$$

Here, $b^{\mathrm{L}} \le 0$ and $b^{\mathrm{R}} \ge 0$ are the so-called signal velocities and the reasonable estimation for them is

$$\begin{array}{ll} b_i^{\mathrm{R}} = \min\left(0, \frac{v_i^{\mathrm{R}}-c_i^{\mathrm{R}}}{1-v_i^{\mathrm{R}}c_i^{\mathrm{R}}}, \frac{\bar{v}_i-\bar{c}_i}{1-\bar{v}_i\bar{c}_i}\right), & b_{i+1}^{\mathrm{L}} = \max\left(0, \frac{c_{i+1}^{\mathrm{L}}+v^{\mathrm{L}}}{1+c_{i+1}^{\mathrm{L}}v_{i+1}^{\mathrm{L}}}, \frac{\bar{c}_i+\bar{v}_i}{1+\bar{c}_i\bar{v}_i}\right), \\ \bar{v}_i = \frac{1}{2}\left(v_i^{\mathrm{R}} + v_{i+1}^{\mathrm{L}}\right), & \bar{c}_i = \frac{1}{2}\left(c_i^{\mathrm{R}} + c_{i+1}^{\mathrm{L}}\right). \end{array} \tag{B.44}$$

The value of $\bar{U}_{i+\frac{1}{2}}$ is determined by the conservation laws around the boundary $x = x_{i+\frac{1}{2}}$.

Integrating (B.8) over $[x_{\min},\ x_{\max}]$, $[x_{\min},\ x_{i+\frac{1}{2}}]$ and $[x_{i+\frac{1}{2}},\ x_{\max}]$, $x_{\min} < x_{i+\frac{1}{2}} + b_i^{\mathrm{R}} t$, $x_{\max} > x_{i+\frac{1}{2}} + b_{i+1}^{\mathrm{L}} t$:

$$b_i^{\mathrm{R}}\bar{U}_i^{\mathrm{R}} + \left(b_{i+1}^{\mathrm{L}} - b_i^{\mathrm{R}}\right)\bar{U}_{i+\frac{1}{2}} - b_{i+1}^{\mathrm{L}}\bar{U}_{i+1}^{\mathrm{L}} = -F\left(\bar{U}_i^{\mathrm{R}}\right) + F\left(\bar{U}_{i+1}^{\mathrm{L}}\right), \tag{B.45}$$

$$b_i^{\mathrm{R}}\bar{U}_i^{\mathrm{R}} - b_i^{\mathrm{R}}\bar{U}_{i+\frac{1}{2}} = -F\left(\bar{U}_{i+\frac{1}{2}}\right) + F\left(\bar{U}_{i+1}^{\mathrm{L}}\right), \tag{B.46}$$

$$b_{i+1}^{\mathrm{L}}\bar{U}_{i+\frac{1}{2}} - b_{i+1}^{\mathrm{L}}\bar{U}_{i+1}^{\mathrm{L}} = -F\left(\bar{U}_i^{\mathrm{R}}\right) + F\left(\bar{U}_{i+\frac{1}{2}}\right). \tag{B.47}$$

Solving the simultaneous equations (B.46)-(B.47), one finally obtains:

$$F_{i+\frac{1}{2}} = F\left(\bar{U}_{i+\frac{1}{2}}\right) = \frac{b_{i+1}^{\mathrm{L}}F\left(\bar{U}_i^{\mathrm{R}}\right) - b_i^{\mathrm{R}}F\left(\bar{U}_{i+1}^{\mathrm{L}}\right) + b_{i+1}^{\mathrm{L}}b_i^{\mathrm{R}}\left(\bar{U}_{i+1}^{\mathrm{L}} - \bar{U}_i^{\mathrm{R}}\right)}{b_{i+1}^{\mathrm{L}} - b_i^{\mathrm{R}}}, \tag{B.48}$$

$$\bar{U}_{i+\frac{1}{2}} = \frac{b_{i+1}^{\mathrm{L}}\bar{U}_{i+1}^{\mathrm{L}} - b_i^{\mathrm{R}}\bar{U}_i^{\mathrm{R}} - F\left(\bar{U}_{i+1}^{\mathrm{L}}\right) + F\left(\bar{U}_i^{\mathrm{R}}\right)}{b_{i+1}^{\mathrm{L}} - b_i^{\mathrm{R}}}. \tag{B.49}$$

Using the values of $\{F_{i+\frac{1}{2}}\}$ obtained above, one evolves the variables $\{U_i^{(n)}\}$ subject to the equation (B.74). In the the present method, $\bar{U}_i^{\mathrm{R}}$ and $\bar{U}_{i+1}^{\mathrm{L}}$ yielded from PPM are used in the initial condition of the Riemann Problem instead of U_i and U_{i+1}. In PPM, a parabolic interpolation is introduced and this prevents the overestimation of the flux between the flux between the cell boundary even if in the case of steep profiles.

B.4 Hydrodynamic Equations in Milne Coordinate

In a general coordinate system, one must consider connection in the covariant derivative. The left-hand side of hydrodynamic equations (B.1) in a general coordinates are

$$\begin{aligned} T^{\mu\nu}{}_{;\mu} &= \partial_\mu T^{\mu\nu} + \Gamma^\mu_{\rho\mu}T^{\rho\nu} + \Gamma^\nu_{\rho\mu}T^{\mu\rho} \\ &= \frac{1}{\sqrt{-g}}\partial_\mu\left(\sqrt{-g}T^{\mu\nu}\right) + \Gamma^\nu_{\rho\mu}T^{\mu\rho}, \end{aligned} \tag{B.50}$$

$$\begin{aligned} N^{\mu}{}_{;\mu} &= \partial_\mu N^{\mu} + \Gamma^\mu_{\rho\mu}N^{\rho} \\ &= \frac{1}{\sqrt{-g}}\partial_\mu\left(\sqrt{-g}N^{\mu}\right). \end{aligned} \tag{B.51}$$

Here, $\Gamma^\mu_{\nu\rho}$ is the Christoffel symbols of the coordinate system. We consider just torsion-free space time in the following. In this case, the Christoffel symbols have only symmetric part in their covariant (lower) indices and can be written:

$$\Gamma^\mu_{\nu\rho} = \frac{1}{2}g^{\mu\sigma}\left(g_{\sigma\nu,\rho} + g_{\sigma\rho,\nu} - g_{\nu\rho,\sigma}\right). \tag{B.52}$$

We use Milne coordinate in the relativistic hydrodynamic calculations for the heavy-ion collisions because of the convenience to describe the longitudinal dynamics. Milne coordinates $(\tau, x, y, \eta_{\mathrm{s}})$ are written in terms of Cartesian coordinates (t, x, y, z) as followings:

$$\tau = \sqrt{t^2 - z^2}, \tag{B.53}$$

$$\eta_{\mathrm{s}} = \frac{1}{2}\ln\frac{t+z}{t-z}. \tag{B.54}$$

τ and η_s are called proper time and space-time rapidity, respectively. Hereafter, we use the indices μ, ν, ρ, σ... for Cartesian coordinates and the indices α, β, γ, δ... for Milne coordinates:

$$x^\mu = (t, x, y, z)\,, x'^\alpha = (\tau, x, y, \eta_s)\,. \tag{B.55}$$

The metric tensors for Milne coordinates are given by

$$g_{\alpha\beta} = \begin{pmatrix} 1 & 0 & 0 & 0 \\ 0 & -1 & 0 & 0 \\ 0 & 0 & -1 & 0 \\ 0 & 0 & 0 & -\tau^2 \end{pmatrix}, g^{\alpha\beta} = \begin{pmatrix} 1 & 0 & 0 & 0 \\ 0 & -1 & 0 & 0 \\ 0 & 0 & -1 & 0 \\ 0 & 0 & 0 & -\frac{1}{\tau^2} \end{pmatrix}. \tag{B.56}$$

The Lorentz transformation between Milne coordinates and Cartesian coordinates is represented by the matrices

$$g^\alpha{}_\mu = \begin{pmatrix} \cosh\eta_s & 0 & 0 & -\sinh\eta_s \\ 0 & 1 & 0 & 0 \\ 0 & 0 & 1 & 0 \\ -\frac{1}{\tau}\sinh\eta_s & 0 & 0 & \frac{1}{\tau}\cosh\eta_s \end{pmatrix}, g^\mu{}_\alpha = \begin{pmatrix} \cosh\eta_s & 0 & 0 & \tau\sinh\eta_s \\ 0 & 1 & 0 & 0 \\ 0 & 0 & 1 & 0 \\ \sinh\eta_s & 0 & 0 & \tau\cosh\eta_s \end{pmatrix}. \tag{B.57}$$

The expressions of the relativistic hydrodynamic equations (B.51), (B.51) are

$$T^{\alpha\beta}{}_{;\alpha} = \frac{1}{\tau}\partial_\alpha\left(\tau T^{\alpha\beta}\right) + \Gamma^\beta_{\gamma\alpha}T^{\alpha\gamma} = 0, N^\alpha{}_{;\alpha} = \frac{1}{\tau}\partial_\alpha\left(\tau N^\alpha\right) = 0. \tag{B.58}$$

The equations of the energy-momentum conservation can not be written in the form of the continuity equations because of the terms with Christoffel symbols for the second contravariant index of the tensor:

$$\frac{\partial}{\partial\tau}\left(\tau T^{\tau\beta}\right) = -\left[\frac{\partial}{\partial x}\left(\tau T^{x\beta}\right) + \frac{\partial}{\partial y}\left(\tau T^{y\beta}\right) + \frac{\partial}{\partial\eta_s}\left(\tau T^{\eta_s\beta}\right)\right] - \tau\Gamma^\beta_{\gamma\alpha}T^{\alpha\gamma}. \tag{B.59}$$

The variables time-evolving in the numerical calculation program are chosen as

$$\tilde{U}^\alpha = \begin{pmatrix} \tilde{U}^\tau \\ \tilde{U}^x \\ \tilde{U}^y \\ \tilde{U}^\eta \end{pmatrix} = \tau\begin{pmatrix} T^{\tau\tau} \\ T^{\tau x} \\ T^{\tau y} \\ \tau T^{\tau\eta_s} \end{pmatrix} = \tau\Lambda^\alpha{}_\mu U^\mu = \begin{pmatrix} \tau\tilde{\gamma}\left(e+p\right) - \tau P \\ \tau\tilde{\gamma}\left(e+p\right)\tilde{v}^x \\ \tau\tilde{\gamma}\left(e+p\right)\tilde{v}^y \\ \tau\tilde{\gamma}\left(e+p\right)\tilde{v}^{\eta_s} \end{pmatrix}, \tilde{U}_N = \tau N^\alpha. \tag{B.60}$$

The equations (B.58)in Cartesian coordinate can be summarized in the following general form:

$$\frac{\partial}{\partial\tau}\tilde{U} = -\tilde{\nabla}_a\tilde{F}^a(\tilde{U}) + \tilde{S}(\tilde{U}), \tag{B.61}$$

$$\tilde{\nabla} = \left(\frac{\partial}{\partial x}, \frac{\partial}{\partial y}, \frac{1}{\tau}\frac{\partial}{\partial\eta_s}\right), \tag{B.62}$$

where a is a index for space components of Milne coordinates. $\tilde{S}(\tilde{U})$ is a source term which originates from non-zero non zero Christoffel symbols for Milne coordinates. U^μ of Cartesian coordinates in Eqs.(B.4) and $\tilde{U}^\alpha$ are connected by the following local Lorentz boost:

$$\tilde{U}^\alpha = \Lambda^\alpha{}_\mu U^\mu, U^\mu = \Lambda^\mu{}_\alpha \tilde{U}^\alpha, \tag{B.63}$$

$$\Lambda^\alpha{}_\mu(\eta_s) = \begin{pmatrix} \cosh\eta_s & 0 & 0 & -\sinh\eta_s \\ 0 & 1 & 0 & 0 \\ 0 & 0 & 1 & 0 \\ -\sinh\eta_s & 0 & 0 & \cosh\eta_s \end{pmatrix}, \Lambda^\mu{}_\alpha(\eta_s) = \begin{pmatrix} \cosh\eta_s & 0 & 0 & \sinh\eta_s \\ 0 & 1 & 0 & 0 \\ 0 & 0 & 1 & 0 \\ \sinh\eta_s & 0 & 0 & \cosh\eta_s \end{pmatrix}. \tag{B.64}$$

$\tilde{F}(\tilde{U})$ and $\tilde{S}(\tilde{U})$ in Eqs. (B.60) can be written as follows:

$$\tilde{F}^a\left(\tilde{U}^\beta\right) = \tau \begin{pmatrix} T^{a\tau} \\ T^{ax} \\ T^{ay} \\ \tau T^{a\eta_s} \end{pmatrix} = \begin{pmatrix} \tilde{v}^a\tilde{U}^\tau + \tau P\tilde{v}^a \\ \tilde{v}^a\tilde{U}^x + \tau P\delta^{ax} \\ \tilde{v}^a\tilde{U}^y + \tau P\delta^{ay} \\ \tilde{v}^a\tilde{U}^{\eta_s} + \tau P\delta^{a\eta_s} \end{pmatrix}, \tag{B.65}$$

$$\tilde{S}\left(\tilde{U}^\alpha\right) = -\begin{pmatrix} \tau\Gamma^\tau{}_{\alpha\beta}T^{\alpha\beta} \\ \tau\Gamma^x{}_{\alpha\beta}T^{\alpha\beta} \\ \tau\Gamma^y{}_{\alpha\beta}T^{\alpha\beta} \\ \tau^2\Gamma^{\eta_s}{}_{\alpha\beta}T^{\alpha\beta} - \tau T^{\tau\eta_s} \end{pmatrix} = -\begin{pmatrix} \frac{1}{\tau}\tilde{U}^\tau\left(\tilde{v}^{\eta_s}\right)^2 + P\left[1 + \left(\tilde{v}^{\eta_s}\right)^2\right] \\ 0 \\ 0 \\ \frac{1}{\tau}\tilde{U}^{\eta_s} \end{pmatrix}, \tag{B.66}$$

$$\tilde{u}^\alpha = \tilde{\gamma}(1, \tilde{v}_x, \tilde{v}_y, \tilde{v}_{\eta_s}) = \Lambda^\alpha{}_\mu u^\mu. \tag{B.67}$$

From $\tilde{U}^\alpha$ and $\tilde{U}_N$ together with the equation of state $P = P(e, n)$, thermodynamic variables and flow velocity can be obtained:

$$\tilde{v} = |\tilde{\boldsymbol{v}}| = \frac{\left|\tilde{\boldsymbol{U}}\right|}{\tilde{U}^\tau + \tau P(e,n)}, \tag{B.68}$$

$$e = \frac{\tilde{U}^\tau}{\tau} - \frac{\left|\tilde{\boldsymbol{U}}\right|}{\tau}\tilde{v}, \tag{B.69}$$

$$n = \frac{\tilde{U}_N}{\tau}\sqrt{1-\tilde{v}^2}, \tag{B.70}$$

$$\tilde{\boldsymbol{U}} = (U^x, U^y, U^{\eta_s}). \tag{B.71}$$

B.5 Scheme for Numerical Hydrodynamic Simulation in Milne Coordinate

A robust scheme for numerical hydrodynamics in full $(3+1)$-dimensional Milne Coordinates [123] is employed in the calculations in this thesis and plays a crucial role to keep the energy-momentum conservation in the hydrodynamical evolution.

Hydrodynamic equations in Milne coordinate (B.62) are not written in the form of the continuity equations because of the extra source terms. The discretized equations are

$$\tilde{U}_i^{n+1} = \tilde{U}_i^n - \frac{\Delta\tau}{\Delta x}\left(\tilde{F}_{i+\frac{1}{2}} - \tilde{F}_{i-\frac{1}{2}}\right) + \tilde{S}_i. \tag{B.72}$$

In numerical calculations, discretization errors in the source terms break the conservation low. If we keep the the second contravariant index of the energy-momentum tensor in Cartesian coordinate, the source terms do not appear:

$$\frac{\partial}{\partial\tau}\left(\tau T^{\tau\nu}\right) = -\left[\frac{\partial}{\partial x}\left(\tau T^{x\nu}\right) + \frac{\partial}{\partial y}\left(\tau T^{y\nu}\right) + \frac{\partial}{\partial\eta_{\rm s}}\left(\tau T^{\eta_{\rm s}\nu}\right)\right]. \tag{B.73}$$

The numerical breaking of the conservation law can be avoided if we choose the variables time-evolving in the program as:

$$\check{U}^\mu = \tau\Lambda^\tau{}_\nu T^{\nu\mu} = -\Lambda^\mu{}_\alpha\tilde{U}^\alpha, \tag{B.74}$$

$$\frac{\partial}{\partial\tau}\check{U}^\mu + \tilde{\nabla}_a\check{F}^{a\mu} = 0. \tag{B.75}$$

However, in this case, a Lorentz transformation is needed when one calculates the flow velocity used in PPM and rHLLE. Numerical errors in the Lorentz transformation induce extra fluxes even in the case of zero flow velocity. To avoid both numerical breaking of the conservation law and numerical extra fluxes, we refer $\check{F}^{a\mu}$ in Eq. (B.75) as a function of $\tilde{U}^\alpha$ so that PPM and rHLLE are applied to the variable $\tilde{U}^\alpha$:

$$\tilde{\nabla}_a\check{F}^{a\mu} = \tilde{\nabla}_a\left[\Lambda^\mu{}_\beta\tilde{F}^a(\tilde{U}^\beta)\right] \tag{B.76}$$

$$\tag{B.77}$$

Once, one calculates $\tilde{F}(\tilde{U})$ through PPM and rHLLE, then performs the Lorentz transformation of $\tilde{F}(\tilde{U})$. From the transformed $\tilde{F}(\tilde{U})$, one obtains the value of $\check{U}$ at the next step:

$$\check{U}_i^{\nu\,(n+1)} - \check{U}_i^{\nu\,(n)} = \frac{\Delta\tau}{\Delta x}\left[-\Lambda^\nu{}_\alpha\left(\eta_{{\rm s}\,i+\frac{1}{2}}\right)\tilde{F}_{i+\frac{1}{2}}(\tilde{U}^\alpha) + \Lambda^\nu{}_\alpha\left(\eta_{{\rm s}\,i-\frac{1}{2}}\right)\tilde{F}_{i-\frac{1}{2}}(\tilde{U}^\alpha)\right]. \tag{B.78}$$

A point to notice is that $\tilde{F}_{i+\frac{1}{2}}$ is transformed according to the Lorentz boost with the value of $\eta_{\rm s}$ at the cell boundary.

Finally, the value of $\tilde{U}$ at the next step is obtained by performing the Lorentz transformation of $\check{U}$ at the next step:

$$\tilde{U}_i^{\alpha\,(n+1)} = \tilde{U}_i^{\alpha\,(n)} + \Lambda^\alpha{}_\nu\left(\eta_{{\rm s}i}\right)\left[\check{U}_i^{\nu\,(n+1)} - \check{U}_i^{\nu\,(n)}\right]. \tag{B.79}$$

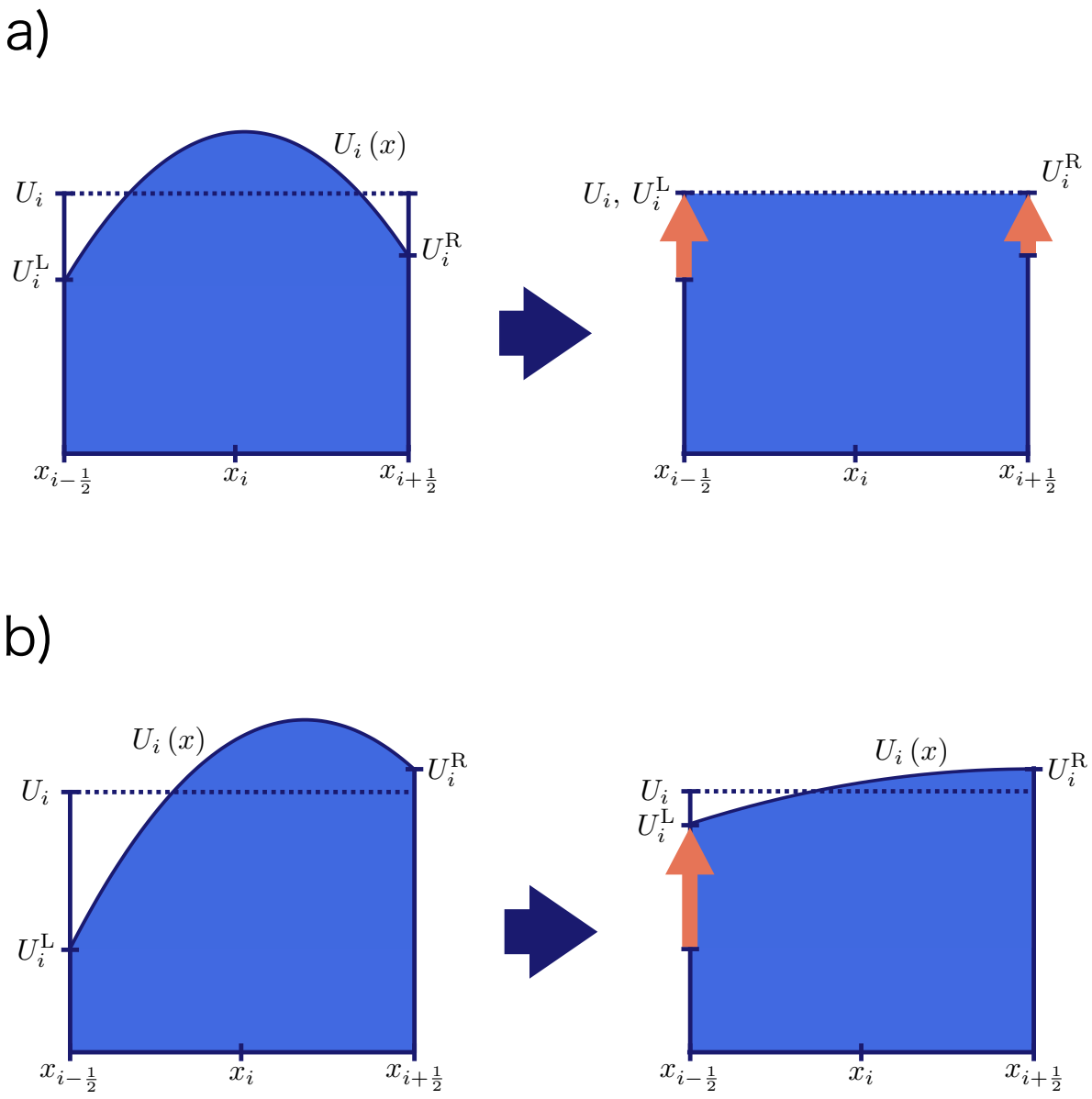

Figure B.1: Reset of the value of U^{L} and U^{R} subject to the monotonicity constraint (Eqs. (B.36)). a) The case where U_i does not take on its value between U_i^{L} and U_i^{R}. In this case, both U_i^{L} and U_i^{R} are reset so that the interpolation function becomes constant. b) The case where U_i is between U_i^{L} and U_i^{R} but the interpolation function has a local maximum or minimum. In this case, the value at the edge farther from the local maximum or minimum point (in the example of this figure, U_i^{L}) to move the local maximum or minimum point to the closer edge of the cell (in the example of this figure, the right end) keeping the mean value U_i fixed.

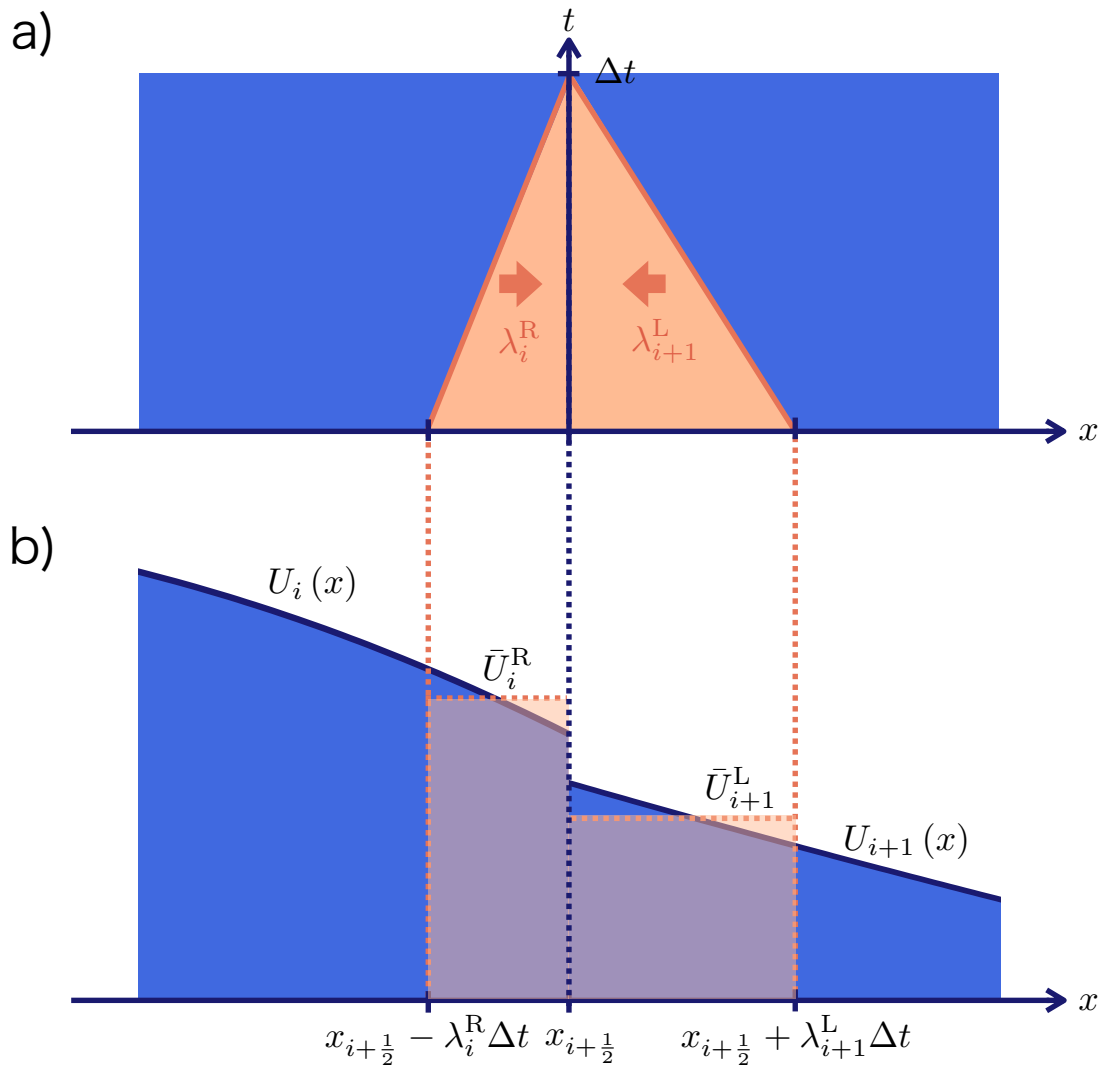

Figure B.2: a) The regions from where sound waves can arrive at the interface at the end of the time step (the orange colored regions). b) The averaged values employed in the initial condition of the Riemann problem (Eq. (B.42)) calculated by integration of the interpolation function over these region

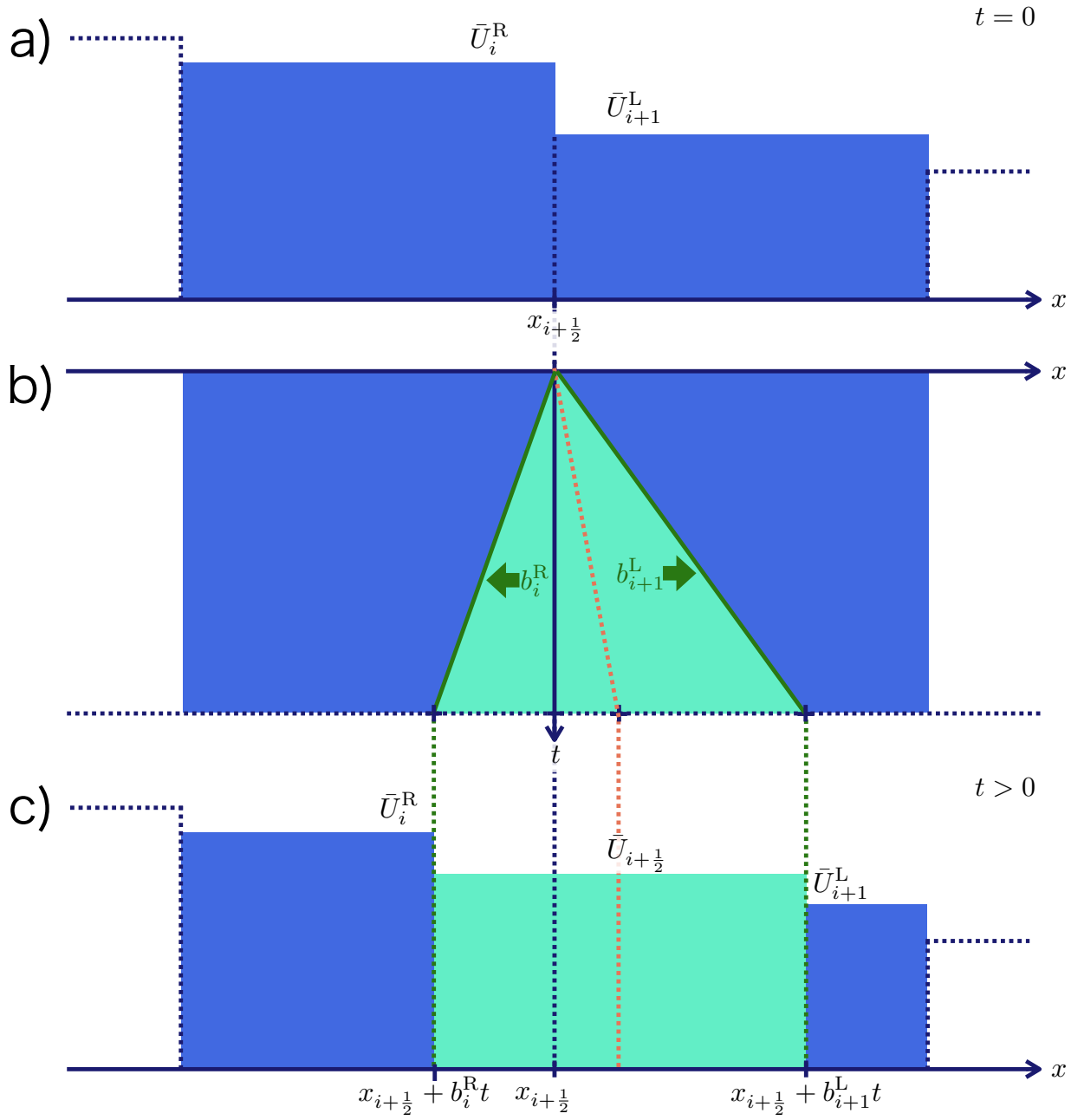

Figure B.3: Approximated development of a Riemann problem a) Initial condition for the Riemann problem to be solved approximately by rHLLE algorithm. b) The corresponding spacetime regions where sound waves from the interface can reach up to the given time. c) Approximated solution of the Riemnn problems.

References

[1] K. Yagi, T. Hatsuda, and Y. Miake, "Quark-gluon plasma: From big bang to little bang," *Camb.Monogr.Part.Phys.Nucl.Phys.Cosmol.* **23** (2005) 1–446.

[2] U. W. Heinz and P. F. Kolb, "Early thermalization at RHIC," *Nucl.Phys.* **A702** (2002) 269–280.

[3] T. Lee, "The strongly interacting quark-gluon plasma and future physics," *Nucl.Phys.* **A750** (2005) 1–8.

[4] M. Gyulassy and L. McLerran, "New forms of QCD matter discovered at RHIC," *Nucl.Phys.* **A750** (2005) 30–63.

[5] E. V. Shuryak, "What RHIC experiments and theory tell us about properties of quark-gluon plasma?," *Nucl.Phys.* **A750** (2005) 64–83.

[6] T. Hirano and M. Gyulassy, "Perfect fluidity of the quark gluon plasma core as seen through its dissipative hadronic corona," *Nucl.Phys.* **A769** (2006) 71–94.

[7] J. Bjorken, "Energy Loss of Energetic Partons in Quark - Gluon Plasma: Possible Extinction of High p(t) Jets in Hadron - Hadron Collisions,".

[8] D. A. Appel, "Jets as a Probe of Quark - Gluon Plasmas," *Phys.Rev.* **D33** (1986) 717.

[9] J. Blaizot and L. D. McLerran, "Jets in Expanding Quark - Gluon Plasmas," *Phys.Rev.* **D34** (1986) 2739.

[10] M. Rammerstorfer and U. W. Heinz, "Jet acoplanarity as a quark - gluon plasma probe," *Phys.Rev.* **D41** (1990) 306–309.

[11] M. Gyulassy and M. Plumer, "Jet Quenching in Dense Matter," *Phys.Lett.* **B243** (1990) 432–438.

[12] M. H. Thoma and M. Gyulassy, "Quark Damping and Energy Loss in the High Temperature QCD," *Nucl.Phys.* **B351** (1991) 491–506.

[13] M. Gyulassy and X.-n. Wang, "Multiple collisions and induced gluon Bremsstrahlung in QCD," *Nucl.Phys.* **B420** (1994) 583–614.

[14] **ATLAS Collaboration** , G. Aad *et al.*, "Observation of a Centrality-Dependent Dijet Asymmetry in Lead-Lead Collisions at $\sqrt{s_{NN}} = 2.77$ TeV with the ATLAS Detector at the LHC,"

[15] **CMS Collaboration** , S. Chatrchyan *et al.*, "Observation and studies of jet quenching in PbPb collisions at nucleon-nucleon center-of-mass energy = 2.76 TeV,"

[16] **CMS Collaboration** , C. Collaboration,

[17] C. Roland, "Jet measurements by the CMS experiment in pp and PbPb collisions," *J.Phys.* **G38** (2011) 124020.

[18] L. D. Landau and E. M. Lifshitz, *Fluid Mechanics*. Pergamon, Oxford, second ed., 1987.

[19] H. Stoecker, "Collective flow signals the quark gluon plasma," *Nucl.Phys.* **A750** (2005) 121–147.

[20] J. Casalderrey-Solana, E. Shuryak, and D. Teaney, "Conical flow induced by quenched QCD jets," *J.Phys.Conf.Ser.* **27** (2005) 22–31.

[21] R. Neufeld, B. Muller, and J. Ruppert, "Sonic Mach Cones Induced by Fast Partons in a Perturbative Quark-Gluon Plasma," *Phys.Rev.* **C78** (2008) 041901.

[22] R. Neufeld, "Mach cones in the quark-gluon plasma: Viscosity, speed of sound, and effects of finite source structure," *Phys.Rev.* **C79** (2009) 054909.

[23] R. Neufeld and B. Muller, "The sound produced by a fast parton in the quark-gluon plasma is a 'crescendo'," *Phys.Rev.Lett.* **103** (2009) 042301.

[24] G.-Y. Qin, A. Majumder, H. Song, and U. Heinz, "Energy and momentum deposited into a QCD medium by a jet shower," *Phys.Rev.Lett.* **103** (2009) 152303.

[25] R. Neufeld and T. Renk, "The Mach cone signal and energy deposition scenarios in linearized hydrodynamics," *Phys.Rev.* **C82** (2010) 044903.

[26] A. Chaudhuri and U. Heinz, "Effect of jet quenching on the hydrodynamical evolution of QGP," *Phys.Rev.Lett.* **97** (2006) 062301.

[27] B. Betz, J. Noronha, G. Torrieri, M. Gyulassy, and D. H. Rischke, "Universal Flow-Driven Conical Emission in Ultrarelativistic Heavy-Ion Collisions," *Phys.Rev.Lett.* **105** (2010) 222301.

[28] Y. Tachibana and T. Hirano, "Emission of Low Momentum Particles at Large Angles from Jet," *Nucl.Phys.* **A904-905** (2013) 1023c–1026c.

[29] Y. Tachibana and T. Hirano, "Momentum transport away from a jet in an expanding nuclear medium," *Phys.Rev.* **C90** (2014) 021902.

[30] R. P. G. Andrade, J. Noronha, and G. S. Denicol, "Jet quenching effects on the direct, elliptic, and triangular flow at RHIC,".

[31] S. Floerchinger and K. C. Zapp, "Hydrodynamics and Jets in Dialogue,".

[32] M. Schulc and B. Tomasik, "Anisotropic flow of the fireball fed by hard partons,".

[33] S. S. Gubser, S. S. Pufu, and A. Yarom, "Sonic booms and diffusion wakes generated by a heavy quark in thermal AdS/CFT," *Phys.Rev.Lett.* **100** (2008) 012301.

[34] P. M. Chesler and L. G. Yaffe, "The Stress-energy tensor of a quark moving through a strongly-coupled N=4 supersymmetric Yang-Mills plasma: Comparing hydrodynamics and AdS/CFT," *Phys.Rev.* **D78** (2008) 045013.

[35] J. Noronha, M. Gyulassy, and G. Torrieri, "Di-Jet Conical Correlations Associated with Heavey Quark Jets in anti-de Sitter Space/Conformal Field Theory Correspondence," *Phys.Rev.Lett.* **102** (2009) 102301.

[36] I. Bouras, A. El, O. Fochler, H. Niemi, Z. Xu, *et al.*, "Transition From Ideal To Viscous Mach Cones In A Kinetic Transport Approach," *Phys.Lett.* **B710** (2012) 641–646.

[37] I. Bouras, B. Betz, Z. Xu, and C. Greiner, "Mach cones in viscous heavy-ion collisions," *Phys.Rev.* **C90** (2014) 024904.

[38] K. G. Wilson, "Confinement of Quarks," *Phys.Rev.* **D10** (1974) 2445–2459.

[39] J. C. Collins and M. Perry, "Superdense Matter: Neutrons Or Asymptotically Free Quarks?," *Phys.Rev.Lett.* **34** (1975) 1353.

[40] N. Cabibbo and G. Parisi, "Exponential Hadronic Spectrum and Quark Liberation," *Phys.Lett.* **B59** (1975) 67–69.

[41] **PHENIX Collaboration** , K. Adcox *et al.*, "Formation of dense partonic matter in relativistic nucleus-nucleus collisions at RHIC: Experimental evaluation by the PHENIX collaboration,"

[42] **STAR Collaboration** , J. Adams *et al.*, "Experimental and theoretical challenges in the search for the quark gluon plasma: The STAR Collaboration's critical assessment of the evidence from RHIC collisions,"

[43] B. Back, M. Baker, M. Ballintijn, D. Barton, B. Becker, *et al.*, "The PHOBOS perspective on discoveries at RHIC," *Nucl.Phys.* **A757** (2005) 28–101.

[44] **BRAHMS Collaboration** , I. Arsene *et al.*, "Quark gluon plasma and color glass condensate at RHIC? The Perspective from the BRAHMS experiment,"

[45] F. Cooper and G. Frye, "Comment on the Single Particle Distribution in the Hydrodynamic and Statistical Thermodynamic Models of Multiparticle Production," *Phys.Rev.* **D10** (1974) 186.

[46] Y. Nara, N. Otuka, A. Ohnishi, K. Niita, and S. Chiba, "Study of relativistic nuclear collisions at AGS energies from p + Be to Au + Au with hadronic cascade model," *Phys.Rev.* **C61** (2000) 024901.

[47] M. Isse, A. Ohnishi, N. Otuka, P. Sahu, and Y. Nara, "Mean-field effects on collective flows in high-energy heavy-ion collisions from AGS to SPS energies," *Phys.Rev.* **C72** (2005) 064908.

[48] S. Bass, M. Belkacem, M. Bleicher, M. Brandstetter, L. Bravina, *et al.*, "Microscopic models for ultrarelativistic heavy ion collisions," *Prog.Part.Nucl.Phys.* **41** (1998) 255–369.

[49] M. Bleicher, E. Zabrodin, C. Spieles, S. Bass, C. Ernst, *et al.*, "Relativistic hadron hadron collisions in the ultrarelativistic quantum molecular dynamics model," *J.Phys.* **G25** (1999) 1859–1896.

[50] T. Hirano, N. van der Kolk, and A. Bilandzic, "Hydrodynamics and Flow," *Lect.Notes Phys.* **785** (2010) 139–178.

[51] J.-Y. Ollitrault, "Anisotropy as a signature of transverse collective flow," *Phys.Rev.* **D46** (1992) 229–245.

[52] J.-Y. Ollitrault, "Determination of the reaction plane in ultrarelativistic nuclear collisions," *Phys.Rev.* **D48** (1993) 1132–1139.

[53] P. Huovinen, P. Kolb, U. W. Heinz, P. Ruuskanen, and S. Voloshin, "Radial and elliptic flow at RHIC: Further predictions," *Phys.Lett.* **B503** (2001) 58–64.

[54] **STAR Collaboration** , J. Adams *et al.*, "Particle type dependence of azimuthal anisotropy and nuclear modification of particle production in Au + Au collisions at s(NN)**(1/2) = 200-GeV,"

[55] B. Alver, M. Baker, C. Loizides, and P. Steinberg, "The PHOBOS Glauber Monte Carlo,".

[56] M. Luzum, "Flow fluctuations and long-range correlations: elliptic flow and beyond," *J.Phys.* **G38** (2011) 124026.

[57] M. L. Miller, K. Reygers, S. J. Sanders, and P. Steinberg, "Glauber modeling in high energy nuclear collisions," *Ann.Rev.Nucl.Part.Sci.* **57** (2007) 205–243.

[58] W. Broniowski, M. Rybczynski, and P. Bozek, "GLISSANDO: Glauber initial-state simulation and more..," *Comput.Phys.Commun.* **180** (2009) 69–83.

[59] H.-J. Drescher and Y. Nara, "Effects of fluctuations on the initial eccentricity from the Color Glass Condensate in heavy ion collisions," *Phys.Rev.* **C75** (2007) 034905.

[60] H.-J. Drescher and Y. Nara, "Eccentricity fluctuations from the color glass condensate at RHIC and LHC," *Phys.Rev.* **C76** (2007) 041903.

[61] B. Schenke, P. Tribedy, and R. Venugopalan, "Fluctuating Glasma initial conditions and flow in heavy ion collisions," *Phys.Rev.Lett.* **108** (2012) 252301.

[62] C. Gale, S. Jeon, B. Schenke, P. Tribedy, and R. Venugopalan, "Event-by-event anisotropic flow in heavy-ion collisions from combined Yang-Mills and viscous fluid dynamics," *Phys.Rev.Lett.* **110** (2013) 012302.

[63] **ATLAS Collaboration** , G. Aad *et al.*, "Measurement of the azimuthal anisotropy for charged particle production in $\sqrt{s_{NN}} = 2.76$ TeV lead-lead collisions with the ATLAS detector,"

[64] R. J. Glauber, *Lectures in Theoretical Physics*, vol. 1. Interscience, New York, 1959.

[65] W. Czyz and L. Maximon, "High-energy, small angle elastic scattering of strongly interacting composite particles," *Annals Phys.* **52** (1969) 59–121.

[66] R. Glauber and G. Matthiae, "High-energy scattering of protons by nuclei," *Nucl.Phys.* **B21** (1970) 135–157.

[67] A. Bialas, M. Bleszynski, and W. Czyz, "Multiplicity Distributions in Nucleus-Nucleus Collisions at High-Energies," *Nucl.Phys.* **B111** (1976) 461.

[68] D. Kharzeev, C. Lourenco, M. Nardi, and H. Satz, "A Quantitative analysis of charmonium suppression in nuclear collisions," *Z.Phys.* **C74** (1997) 307–318.

[69] **PHOBOS Collaboration** , B. Back *et al.*,

[70] **PHENIX Collaboration** , K. Adcox *et al.*, "Centrality dependence of charged particle multiplicity in Au - Au collisions at S(NN)**(1/2) = 130-GeV,"

[71] X.-N. Wang and M. Gyulassy, "Energy and centrality dependence of rapidity densities at RHIC," *Phys.Rev.Lett.* **86** (2001) 3496–3499.

[72] D. Kharzeev and M. Nardi, "Hadron production in nuclear collisions at RHIC and high density QCD," *Phys.Lett.* **B507** (2001) 121–128.

[73] P. Kolb, U. W. Heinz, P. Huovinen, K. Eskola, and K. Tuominen, "Centrality dependence of multiplicity, transverse energy, and elliptic flow from hydrodynamics," *Nucl.Phys.* **A696** (2001) 197–215.

[74] P. F. Kolb and U. W. Heinz, "Hydrodynamic description of ultrarelativistic heavy ion collisions,".

[75] J. Bjorken, "Highly Relativistic Nucleus-Nucleus Collisions: The Central Rapidity Region," *Phys.Rev.* **D27** (1983) 140–151.

[76] T. Ishii and S. Muroya, "Hydrodynamical model analysis of the (3+1)-dimensional cylindrical symmetric baryon rich quark - gluon plasma with phase transition," *Phys.Rev.* **D46** (1992) 5156–5167.

[77] K. Morita, S. Muroya, H. Nakamura, and C. Nonaka, "Numerical analysis of two pion correlation based on a hydrodynamical model," *Phys.Rev.* **C61** (2000) 034904.

[78] T. Hirano, K. Morita, S. Muroya, and C. Nonaka, "Hydrodynamical analysis of hadronic spectra in the 130 GeV/nucleon Au+Au collisions," *Phys.Rev.* **C65** (2002) 061902.

[79] T. Hirano, "Is early thermalization achieved only near mid-rapidity at RHIC?," *Phys.Rev.* **C65** (2002) 011901.

[80] T. Hirano and K. Tsuda, "Collective flow and two pion correlations from a relativistic hydrodynamic model with early chemical freezeout," *Phys.Rev.* **C66** (2002) 054905.

[81] S. J. Brodsky, J. Gunion, and J. H. Kuhn, "Hadron Production in Nuclear Collisions: A New Parton Model Approach," *Phys.Rev.Lett.* **39** (1977) 1120.

[82] A. Adil and M. Gyulassy, "3D jet tomography of twisted strongly coupled quark gluon plasmas," *Phys.Rev.* **C72** (2005) 034907.

[83] T. Hirano, U. W. Heinz, D. Kharzeev, R. Lacey, and Y. Nara, "Hadronic dissipative effects on elliptic flow in ultrarelativistic heavy-ion collisions," *Phys.Lett.* **B636** (2006) 299–304.

[84] D. d'Enterria, "Jet quenching,".

[85] Y. L. Dokshitzer, "Calculation of the Structure Functions for Deep Inelastic Scattering and e+ e- Annihilation by Perturbation Theory in Quantum Chromodynamics.," *Sov.Phys.JETP* **46** (1977) 641–653.

[86] V. Gribov and L. Lipatov, "Deep inelastic e p scattering in perturbation theory," *Sov.J.Nucl.Phys.* **15** (1972) 438–450.

[87] V. Gribov and L. Lipatov, "e+ e- pair annihilation and deep inelastic e p scattering in perturbation theory," *Sov.J.Nucl.Phys.* **15** (1972) 675–684.

[88] G. Altarelli and G. Parisi, "Asymptotic Freedom in Parton Language," *Nucl.Phys.* **B126** (1977) 298.

[89] R. K. Ellis, W. J. Stirling, and B. Webber, "QCD and collider physics," *Camb.Monogr.Part.Phys.Nucl.Phys.Cosmol.* **8** (1996) 1–435.

[90] N. Armesto, L. Cunqueiro, C. A. Salgado, and W.-C. Xiang, "Medium-evolved fragmentation functions," *JHEP* **0802** (2008) 048.

[91] B. A. Kniehl, G. Kramer, and B. Potter, "Fragmentation functions for pions, kaons, and protons at next-to-leading order," *Nucl.Phys.* **B582** (2000) 514–536.

[92] X.-N. Wang and X.-f. Guo, "Multiple parton scattering in nuclei: Parton energy loss," *Nucl.Phys.* **A696** (2001) 788–832.

[93] E. Braaten and M. H. Thoma, "Energy loss of a heavy quark in the quark - gluon plasma," *Phys.Rev.* **D44** (1991) 2625–2630.

[94] M. H. Thoma, "Collisional energy loss of high-energy jets in the quark gluon plasma," *Phys.Lett.* **B273** (1991) 128–132.

[95] R. Baier, Y. L. Dokshitzer, A. H. Mueller, S. Peigne, and D. Schiff, "Radiative energy loss of high-energy quarks and gluons in a finite volume quark - gluon plasma," *Nucl.Phys.* **B483** (1997) 291–320.

[96] B. Zakharov, "Fully quantum treatment of the Landau-Pomeranchuk-Migdal effect in QED and QCD," *JETP Lett.* **63** (1996) 952–957.

[97] R. Baier, Y. L. Dokshitzer, A. H. Mueller, S. Peigne, and D. Schiff, "Radiative energy loss and p(T) broadening of high-energy partons in nuclei," *Nucl.Phys.* **B484** (1997) 265–282.

[98] B. Zakharov, "Radiative energy loss of high-energy quarks in finite size nuclear matter and quark - gluon plasma," *JETP Lett.* **65** (1997) 615–620.

[99] R. Baier, Y. L. Dokshitzer, A. H. Mueller, and D. Schiff, "Medium induced radiative energy loss: Equivalence between the BDMPS and Zakharov formalisms," *Nucl.Phys.* **B531** (1998) 403–425.

[100] U. A. Wiedemann, "Gluon radiation off hard quarks in a nuclear environment: Opacity expansion," *Nucl.Phys.* **B588** (2000) 303–344.

[101] C. A. Salgado and U. A. Wiedemann, "Calculating quenching weights," *Phys.Rev.* **D68** (2003) 014008.

[102] N. Armesto, C. A. Salgado, and U. A. Wiedemann, "Medium induced gluon radiation off massive quarks fills the dead cone," *Phys.Rev.* **D69** (2004) 114003.

[103] P. B. Arnold, G. D. Moore, and L. G. Yaffe, "Photon emission from quark gluon plasma: Complete leading order results," *JHEP* **0112** (2001) 009.

[104] P. B. Arnold, G. D. Moore, and L. G. Yaffe, "Photon emission from ultrarelativistic plasmas," *JHEP* **0111** (2001) 057.

[105] P. B. Arnold, G. D. Moore, and L. G. Yaffe, "Photon and gluon emission in relativistic plasmas," *JHEP* **0206** (2002) 030.

[106] S. Jeon and G. D. Moore, "Energy loss of leading partons in a thermal QCD medium," *Phys.Rev.* **C71** (2005) 034901.

[107] M. Gyulassy, P. Levai, and I. Vitev, "Jet quenching in thin quark gluon plasmas. 1. Formalism," *Nucl.Phys.* **B571** (2000) 197–233.

[108] M. Gyulassy, P. Levai, and I. Vitev, "Reaction operator approach to nonAbelian energy loss," *Nucl.Phys.* **B594** (2001) 371–419.

[109] A. Majumder, "The In-medium scale evolution in jet modification,".

[110] **ALICE Collaboration** , K. Aamodt *et al.*, "Suppression of Charged Particle Production at Large Transverse Momentum in Central Pb–Pb Collisions at $\sqrt{s_{NN}} = 2.76$ TeV,"

[111] **CMS Collaboration** , S. Chatrchyan *et al.*, "Jet momentum dependence of jet quenching in PbPb collisions at $\sqrt{s_{NN}} = 2.76$ TeV,"

[112] J. Casalderrey-Solana, J. G. Milhano, and U. A. Wiedemann, "Jet Quenching via Jet Collimation," *J.Phys.* **G38** (2011) 035006.

[113] I. Lokhtin, A. Belyaev, and A. Snigirev, "Jet quenching pattern at LHC in PYQUEN model," *Eur.Phys.J.* **C71** (2011) 1650.

[114] G.-Y. Qin and B. Muller, "Explanation of Di-jet asymmetry in Pb+Pb collisions at the Large Hadron Collider," *Phys.Rev.Lett.* **106** (2011) 162302.

[115] C. Young, B. Schenke, S. Jeon, and C. Gale, "Dijet asymmetry at the energies available at the CERN Large Hadron Collider," *Phys.Rev.* **C84** (2011) 024907.

[116] Y. He, I. Vitev, and B.-W. Zhang, "$\mathcal{O}(\alpha_s^3)$ Analysis of Inclusive Jet and di-Jet Production in Heavy Ion Reactions at the Large Hadron Collider," *Phys.Lett.* **B713** (2012) 224–232.

[117] T. Renk, "On the sensitivity of the dijet asymmetry to the physics of jet quenching," *Phys.Rev.* **C85** (2012) 064908.

[118] K. C. Zapp, F. Krauss, and U. A. Wiedemann, "A perturbative framework for jet quenching," *JHEP* **1303** (2013) 080.

[119] J.-P. Blaizot, F. Dominguez, E. Iancu, and Y. Mehtar-Tani, "Probabilistic picture for medium-induced jet evolution," *JHEP* **1406** (2014) 075.

[120] R. Neufeld, "Fast Partons as a Source of Energy and Momentum in a Perturbative Quark-Gluon Plasma," *Phys.Rev.* **D78** (2008) 085015.

[121] R. Neufeld and I. Vitev, "Parton showers as sources of energy-momentum deposition in the QGP and their implication for shockwave formation at RHIC and at the LHC," *Phys.Rev.* **C86** (2012) 024905.

[122] T. Renk, "Space-time structure of the energy deposition into the bulk medium due to jet quenching," *Phys.Rev.* **C88** (2013) 044905.

[123] K. Murase and Y. Tachibana, "Conservative numerical schemes of relativistic dissipative hydrodynamics for heavy-ion collisions: conservation law, and transversality and spatial rotation of dissipative currents (in preparation),".

[124] J. Liao and E. Shuryak, "Angular Dependence of Jet Quenching Indicates Its Strong Enhancement Near the QCD Phase Transition," *Phys.Rev.Lett.* **102** (2009) 202302.

[125] X. Zhang and J. Liao, "Hard probe of geometry and fluctuations in heavy ion collisions at sNN=0.2 , 2.76, and 5.5 TeV," *Phys.Rev.* **C89** no. 1, (2014) 014907.

[126] X. Zhang and J. Liao, "Event-by-event azimuthal anisotropy of jet quenching in relativistic heavy ion collisions," *Phys. Rev. C 87,* **044910** (2013) 044910.

[127] D. Kharzeev, E. Levin, and M. Nardi, "QCD saturation and deuteron nucleus collisions," *Nucl.Phys.* **A730** (2004) 448–459.

[128] L. D. McLerran and R. Venugopalan, "Computing quark and gluon distribution functions for very large nuclei," *Phys.Rev.* **D49** (1994) 2233–2241.

[129] L. D. McLerran and R. Venugopalan, "Green's functions in the color field of a large nucleus," *Phys.Rev.* **D50** (1994) 2225–2233.

[130] T. Hirano and Y. Nara, "Dynamical modeling of high energy heavy ion collisions," *PTEP* **2012** (2012) 01A203.

[131] S. Borsanyi, Z. Fodor, C. Hoelbling, S. D. Katz, S. Krieg, *et al.*, "Full result for the QCD equation of state with 2+1 flavors," *Phys.Lett.* **B730** (2014) 99–104.

[132] **CMS Collaboration** , S. Chatrchyan *et al.*, "Measurement of jet fragmentation into charged particles in *pp* and PbPb collisions at $\sqrt{s_{NN}} = 2.76$ TeV,"

[133] P. Colella and P. R. Woodward, "The Piecewise Parabolic Method (PPM) for Gas Dynamical Simulations," *J.Comput.Phys.* **54** (1984) 174–201.

[134] V. Schneider, U. Katscher, D. Rischke, B. Waldhauser, J. Maruhn, and C.-D. Munz, "New algorithms for ultra-relativistic numerical hydrodynamics.," *J. Comput. Phys.* **105** no. 1, (1993) 92–107.

[135] P. Harten, A. Lax and B. Van Leer, "On upstream differencing and godunov-type schemes for hyperbolic conservation laws," *SIAM Review* **25** no. 1, 35–61.

[136] B. Einfeldt, "On godunov-type methods for gas dynamics," *SIAM J. Numer. Anal.* **25** no. 1, (January, 1988) 294–318.

[137] D. H. Rischke, "Fluid dynamics for relativistic nuclear collisions," *Lect.Notes Phys.* **516** (1999) 21.